Modelling Convective Dissolution and Reaction of Carbon Dioxide in Saline Aquifers

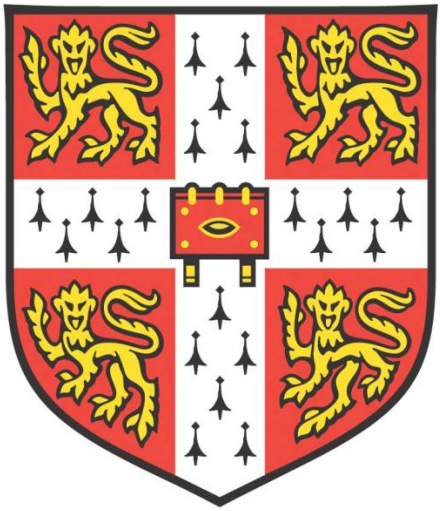

Ilia Cherezov

St John's College

Department of Chemical Engineering and Biotechnology

University of Cambridge

This dissertation is submitted for the degree of Doctor of Philosophy

July 2017

PREFACE

This dissertation is the result of my own work and includes nothing, which is the outcome of work done in collaboration except where specifically indicated in the text (e.g. the linear stability analysis and numerical simulations in chapters 6 and 7 carried out by Professor Kim). The total word count of this thesis including captions, appendices and references is approximately 45,000 words, with a total of 63 figures and 9 tables.

Material from chapters 4, 5 and 6 has been published in Physical Chemistry Chemical Physics (2016), **18**, 23727 and is soon to be published in Physical Chemistry Chemical Physics (2017). Some of the results from Chapter 6 have also been presented at the 69th Annual Meeting of the APS Division of Fluid Dynamics held in Portland, Oregon in 2016. With these exceptions, no part of this thesis has yet been published elsewhere, or has been submitted for a degree, diploma, or other qualification at any other university or academic institution.

Signed:_____

Date:_____

Ilia Cherezov

St John's College, Cambridge

ABSTRACT

In an effort to reduce atmospheric carbon dioxide (CO_2) emissions and mitigate climate change, it has been proposed to sequester supercritical CO_2 in underground saline aquifers. Geological storage of CO_2 involves different trapping mechanisms which are not yet fully understood. In order to improve the understanding of the effect of chemical reaction on the flow and transport of CO_2, these storage mechanisms are modelled experimentally and numerically in this work. In particular, the destabilising interaction between the fluid hydrodynamics and a density-increasing second-order chemical reaction is considered.

It is shown that after nondimensional scaling, the flow in a given physicochemical system is governed by two dimensionless groups, Da/Ra^2, which measures the timescale for convection compared to those for reaction and diffusion, and C_{Bo}', which reflects the excess of the environmental reactant species relative to the diffusing solute. The destabilising reactive scenario is modelled experimentally under standard laboratory conditions using an immiscible two-layer system with acetic acid acting as the solute. A novel colorimetric technique is developed to infer the concentrations of chemical species from the pH of the solution making it possible to measure the flux of solute into the aqueous domain. The validity of this experimental system as a suitable analogue for the dissolution of CO_2 is tested against previous work and the destabilising effect of reaction is investigated by adding ammonia to the lower aqueous layer.

The system is also modelled numerically and it is shown that the aqueous phase reaction between acetic acid and ammonia can be considered to be instantaneous, meaning that Da/Ra^2 tends to infinity and the flow is therefore governed only by the initial dimensionless concentration of reactant in the aqueous phase. The results from the experiments and numerical simulations are in good agreement, showing that an increase in the initial concentration of reactant increases the destabilising effect of reaction, accelerates the onset of convection and enhances the rate of dissolution of solute. The numerical model is then applied to a real world aquifer in the Sleipner gas field and it is demonstrated how the storage capacity of a potential CO_2 reservoir could be enhanced by chemical reaction.

ACKNOWLEDGEMENTS

I wish to thank my supervisor, Dr. Silvana Cardoso, for her guidance and support during the course of this work, especially over the last few months. I would also like to express my gratitude to Dr Jeanne Therese Andres as it was her passion and enthusiasm that inspired me to take on this project in the first place. Some of the results in this work have been obtained as a result of collaboration with Professor Min Chan Kim from Jeju National University, South Korea. It is a pleasure to acknowledge the fruitful discussions that we had together.

A big thank you must go to the fellow researchers from the M1 office for all of their encouragement and positive interactions that helped make this such a stimulating and enjoyable place of work. The help and valuable assistance from the workshop and technical staff of the Department of Chemical Engineering and Biotechnology was hugely appreciated. I am also grateful to the Engineering and Physical Sciences Research Council and to St John's College for providing the financial support necessary to fund this project.

Last but by no means least, my heartfelt gratitude goes out to my family and loved ones who have stuck by me through thick and thin and have made the completion of this work possible. There are of course many countless others who have come and gone over these years, to whom I am greatly indebted. Thank you.

CONTENTS

LIST OF TABLES

LIST OF FIGURES

NOMENCLATURE

Roman Symbols

a	wavenumber	m^{-1}
C	Concentration of species i	M
C_{As}	Aqueous solubility of solute A	M
C_{AT}	Total concentration of solute A	M
C_{BT}	Total concentration of reactant B	M
c_p	Specific heat capacity	$J\ kg^{-1}\ K^{-1}$
D	Molecular diffusion coefficient	$m^2\ s^{-1}$
D_T	Thermal diffusivity	$m^2\ s^{-1}$
Da	Damköhler number	
f_i	Fourier modes of the Fast Fourier Transform	
$\langle f(t) \rangle$	Power averaged mean wavenumber	m^{-1}
g	Gravitational acceleration	$m\ s^{-2}$
h	Hele-Shaw cell gap width	m
$\mathbf{i}$	Unit vector	
J	Mass flux of solute	$kg\ m^{-2}\ s^{-1}$
k	Permeability of the porous media	m^2
k_r	Chemical reaction rate constant	$M^{-1}\ s^{-1}$
K	Equilibrium constant	
L_f	Maximum convective finger length	m
L_s	Convective length scale	m
L_x	Width of the domain	m
L_z	Height of the domain	m
p	Reduced pressure	$kg\ m^{-1}\ s^{-2}$

p_s	Pressure scale	kg m^{-1} s^{-2}
P	Pressure	kg m^{-1} s^{-2}
$P(f)$	Amplitudes of Fast Fourier Transform	
Q	Enthalpy of reaction	J mol^{-1}
Ra	Rayleigh number	
Sh	Sherwood number	
t	Time	s
t_c	Critical time	s
t_m	Time of minimum mass flux	s
t_{oc}	Time for onset of convection	s
t_s	Time scale	s
T	Temperature	K
v	Velocity	m s^{-1}
$\mathbf{v}$	Fluid transport velocity	m s^{-1}
v_s	Velocity scale	m s^{-1}
w	Vertical velocity	m s^{-1}

Greek Symbols

β	Solutal expansion coefficient	kg m^{-3} M^{-1}
β_T	Thermal expansion coefficient	K^{-1}
Δp	Pressure difference	kg m^{-1} s^{-2}
ΔT	Temperature difference	K
$\Delta \rho$	Density difference	kg m^{-3}
ε	Initial perturbation level	
ζ	Self-similar variable	
λ	Wavelength of convective instability	m
μ	Dynamic viscosity	kg m^{-1} s^{-1}

ρ	Density	kg m^{-3}
ρ_0	Reference density	kg m^{-3}
ϕ	Porosity	
ψ	Stream function	m^2 s^{-1}

Subscripts

o	Initial
1	Perturbation
A	Solute
B	Reactant
b	Base state
C	Product of reaction
i	Chemical species index
R	Reaction front
x	Horizontal direction
z	Vertical direction

Superscripts

$'$	Nondimensional

Abbreviations

APS	American Physical Society
BP	British Petroleum
CO_2	Carbon dioxide
DFT	Discrete Fourier transform
DMA	Dominant mode analysis
EGR	Enhanced gas recovery

EOR	Enhanced oil recovery
ESRL	Earth System Research Laboratory
HSV	Hue, Saturation, Value
IPCC	Intergovernmental Panel on Climate Change
GISTEMP	Goddard Institute for Space Studies Surface Temperature Analysis
LED	Light emitting diode
MIBK	Methyl isobutyl ketone
MiniCAM	Mini-Climate Assessment Model
NASA	National Aeronautics and Space Administration
NOAA	National Oceanic and Atmospheric Administration
ISO	International Organisation for Standardisation
PTFE	Polytetrafluorethylene
QSSA	Quasi-Steady State Approximation
RGB	Red, Green, Blue

1 INTRODUCTION

In order to understand the motivation for the geological sequestration of carbon dioxide, it is first necessary to review the impact that anthropogenic emissions of CO_2 into the atmosphere have had on the Earth's climate (§1.1). This is followed by an overview of the different climate change mitigation techniques in section §1.2 and particular focus is given in section §1.3 to the processes that occur in the capture and storage of carbon dioxide on the industrial scale.

1.1 CLIMATE CHANGE

Since the industrial revolution in the late 18th century, society has become increasingly dependent on the use of fossil fuels such as coal, petroleum oil and natural gas. Approximately 86% of the world's energy demand is supplied by the combustion of fossil fuels (BP, 2016) and they are also extensively used in the manufacture and transport industries. The burning of fossil fuels produces carbon dioxide along with other pollutants, which are directly emitted into the atmosphere.

The historic concentration of CO_2 in the atmosphere can be estimated from ice cores at the South Pole (Etheridge et al., 1996) and has also been directly measured since 1958 at the Mauna Loa Observatory in Hawaii by the National Oceanic and Atmospheric Administration (NOAA) and the Earth System Research Laboratory (ESRL). Figure 1.1 shows that the atmospheric concentration of CO_2 has rapidly risen from around 285 parts per million (ppm) by volume in the industrial era to over 400 ppm in 2016.

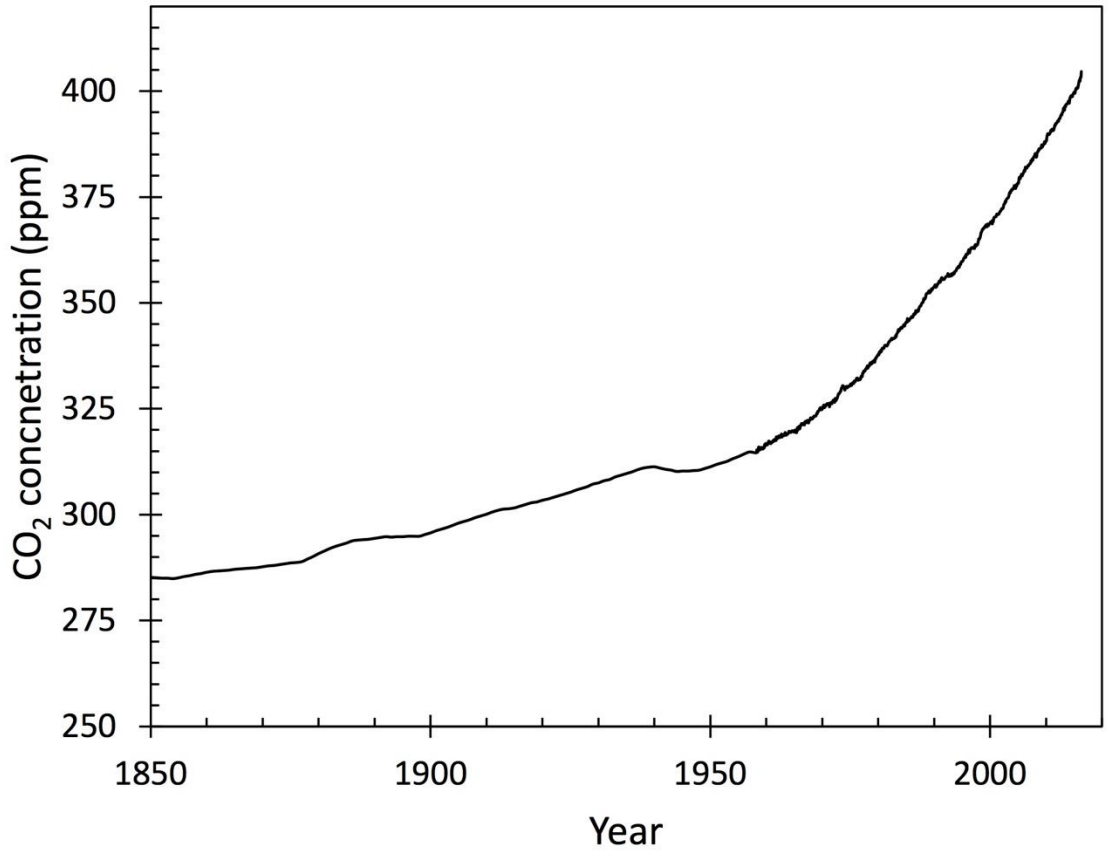

Figure 1.1 Atmospheric concentration of CO_2, ppm by volume, over the last 200 years as measured by Etheridge et al. (1996) and Tans and Keeling (2016).

In recent decades, there has been a 2.1% annual increase in the atmospheric concentration of CO_2 and it is expected to continue to rise (Parry et al., 2007). This increase is largely attributed to the anthropogenic emissions due to fossil fuel combustion and exceeds any natural variability that may occur in the absence of any human involvement.

Carbon dioxide is classed as a greenhouse gas as it absorbs infrared radiation and retains heat within the Earth's atmosphere, which in turn warms the planet's surface. The accumulation of CO_2 in the atmosphere is thought to have a direct effect on the Earth's climate. Records of the past average global surface temperatures kept by the National Aeronautics and Space Administration (NASA) are plotted in Figure 1.2 and show that temperatures have significantly increased over the course of the 20^{th} century. During the last 50 years, the global temperature has risen by roughly 1^{o}C at a rate which is nearly twice than that for the last 100 years.

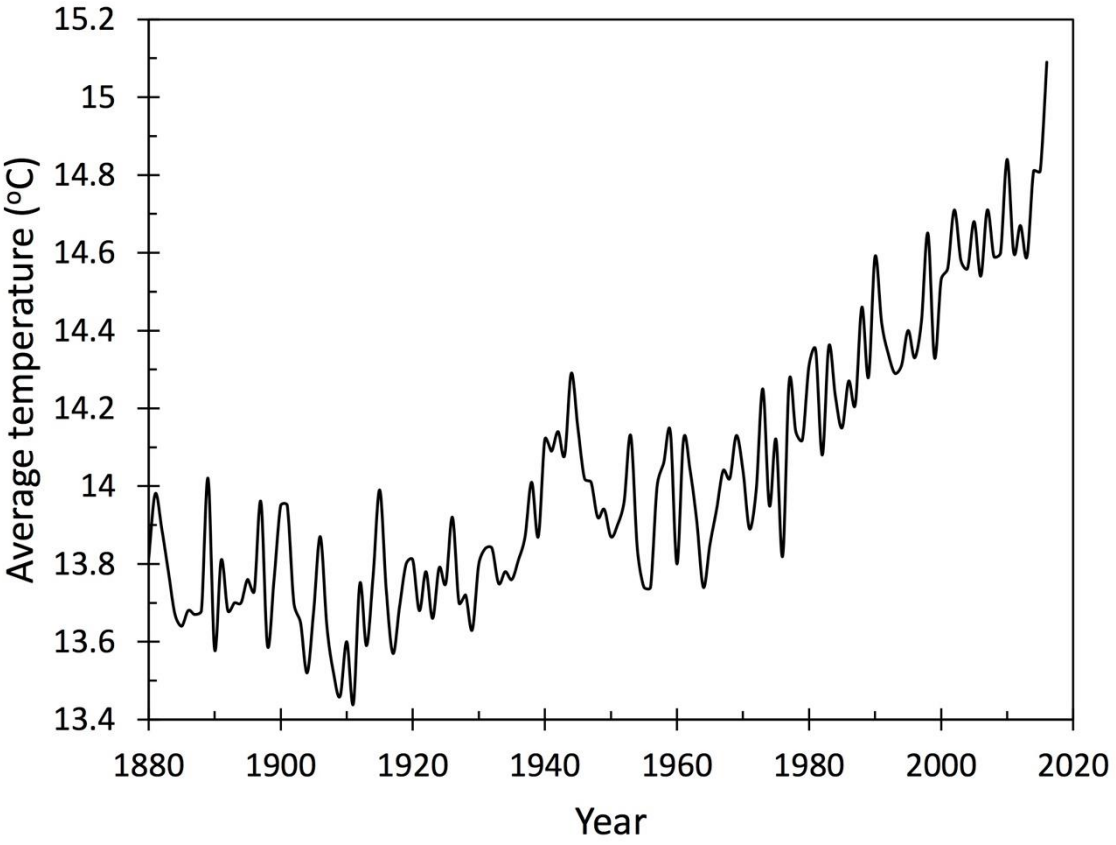

Figure 1.2 Global average surface temperature since 1850 as measured by the NASA Goddard Institute of Space Studies (GISTEMP, 2016).

It is very likely that such "global warming" trends are directly related to the increase in atmospheric greenhouse gas concentrations and CO_2 in particular (IPCC, 2007). Climate models developed by the IPPC (2007) have only been able to reproduce the observed average global surface temperature patterns when anthropogenic forcings have been included and no model has been able to simulate the increase in temperatures since the mid-20th century using only natural forcings such as solar and volcanic activity.

Other changes to the climate have also been identified as human influences have already contributed to the reductions of snow covered layers and rise of sea levels, which lead to the erosion of coastlines (Titus et al., 1985). The uptake of anthropogenic CO_2 can result in the acidification of oceans which could also have a severe impact on ecosystems and biodiversity. In general, the impacts associated with climate change are expected to affect the wellbeing of millions of people through increased malnutrition and spread of infectious diseases, and increased mortality due to heat waves, wildfires, storms floods and droughts (IPCC, 2007).

Further global climate change is expected to be observed if the emissions of greenhouse gases continue at or above the current rate. The IPCC Special Report on Emissions Scenarios (2000) has projected an increase in annual global greenhouse gas emissions by 25 – 90% between the years 2000 and 2030. Even if the atmospheric greenhouse gas and aerosol concentrations are stabilised and kept constant at their year 2000 levels, the average global surface temperature is expected to experience a further warming of 0.1^{o}C per decade (IPCC, 2007). It is very likely that this rise in temperatures will induce drastic changes in the Earth's climate system resulting in far more severe climate effects than those observed during the last century. The reduction of CO_2 emissions into the atmosphere is therefore of major importance in order to mitigate the effects of climate change.

1.2 MITIGATION STRATEGY

Most models of global energy use predict a substantial increase in CO_2 emissions during the course of this century. The Mini-Climate Assessment Model (MiniCAM) in Figure 1.3 shows that the amount of CO_2 released into the atmosphere is likely to almost triple by 2095 if nothing is done to curb emissions (IPCC, 2012).

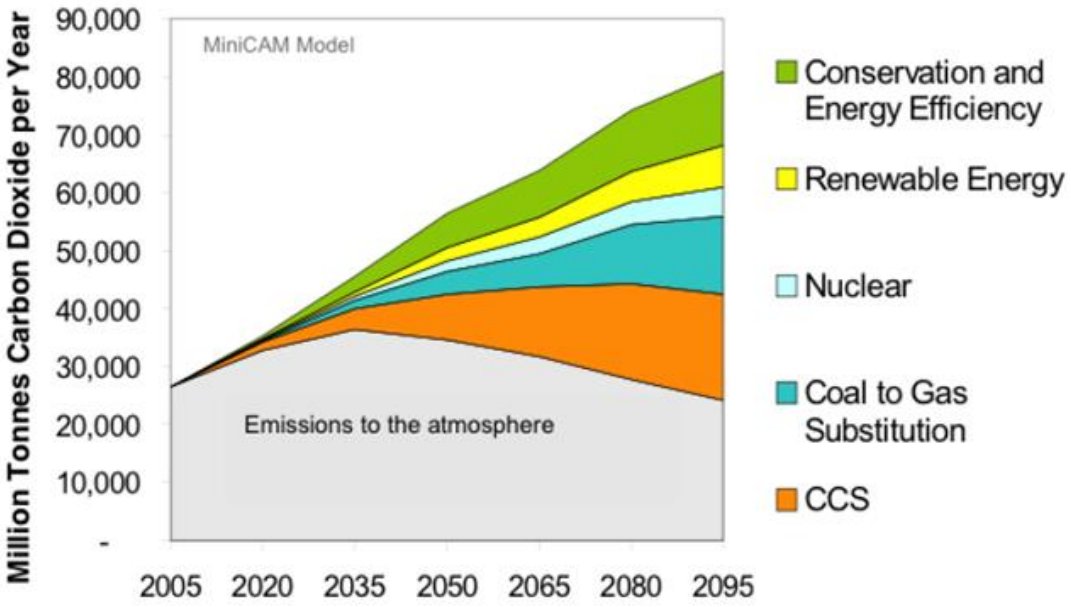

Figure 1.3 MiniCAM model showing the projected annual global CO_2 emissions (top line). Each coloured wedge represents a different mitigation approach that can be implemented to help reduce CO_2 emissions into the atmosphere (IPCC, 2012).

Several mitigation strategies have been proposed in order to mitigate climate change and these include reducing overall demand for energy, developing more efficient technologies or switching to alternative, zero-carbon, energy sources such as solar, wind, hydropower, geothermal, biomass and also nuclear power. The contribution of these different actions on CO_2 mitigation is illustrated by the wedges in Figure 1.3, which shows that the combined implementation of all the proposed techniques would result in the stabilisation and subsequent decline in in annual emissions. An important component of the broad portfolio of energy technologies and emission reduction strategies is carbon dioxide capture and storage (CCS).

1.3 CARBON DIOXIDE CAPTURE AND STORAGE

It is possible to capture CO_2 produced by large point sources such as power generation plants and other large-scale industrial processes such as ammonia, iron and steel manufacturing (Herzog and Golomb, 2004). The purpose of CO_2 capture is to produce a high pressure, concentrated stream of CO_2 that can be transported for storage. The added short-term advantage of CCS as a CO_2 mitigation option is that it enables the continued use of fossil fuels whilst other renewable and alternative sources of energy are being developed.

The technology for capture is well developed and there are three main capture techniques: post-combustion capture, pre-combustion capture and oxyfuel combustion where pure oxygen is used during combustion so that the flue gas contains mostly CO_2 and water. The use of the different capture methods depends on the type of plant and on how far down the process they are implemented. Amongst the three systems, post-combustion is the best understood technique, in which CO_2 is separated from other gaseous products in the combustion flue gas by means of physical or chemical solvents and membranes. Another advantage of post-combustion capture is that it can be retrofitted to existing plants as there is no need to modify the combustion process. After the CO_2 is captured, it can then be reused in other industrial processes or transported to suitable storage sites where it is isolated from the atmosphere for a long period of time.

Potential storage methods include the injection of CO_2 into underground geological formations, storage in deep oceans or mineral carbonation (IPCC, 2012). Mineral carbonation involves the conversion of CO_2 into solid inorganic carbonates using chemical reactions with metal oxides found in silicates, in an accelerated process similar to natural weathering. However, this option is still in the development stage and would

require high cost, large-scale mining to supply the necessary quantities of silicates, causing a significant impact on the environment. The environmental risks to the marine ecosystems posed by injection of CO_2 into oceans along with the economic and policy considerations also rule out ocean storage as a viable option.

In contrast to these alternatives, geological sequestration is already ongoing with a number of industrial scale projects in operation, annually storing in the order of one million tonnes of CO_2 or more. These include the Sleipner project in the North Sea, the Weyburn project in Canada and the In Salah project in Algeria (IPCC, 2012). During geological sequestration, CO_2 is trapped in underground formations such as depleted oil and gas reservoirs, coal seams and deep saline aquifers. In addition CO_2 can also be injected into reservoirs for enhanced oil recovery (EOR) and enhanced gas recovery (EGR), which increases the reservoir's pressure to boost production, leaving CO_2 to remain permanently stored in the formation. An overview of the different geological storage options is provided in Figure 1.4.

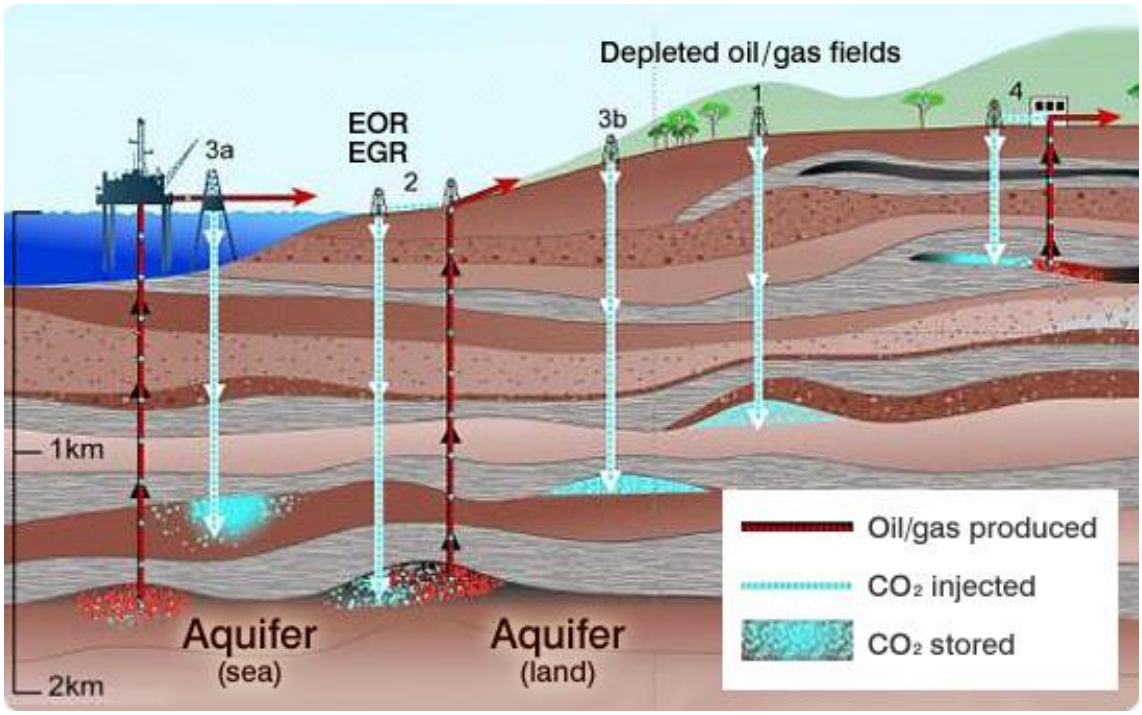

Figure 1.4 Methods for storing CO2 in geological formations. (1) corresponds to depleted oil and gas reservoirs, (2) use of CO_2 for EOR and EGR, (3a) deep offshore and (3b) deep onshore saline formations and (4) use of CO_2 in enhanced coal bed methane recovery. Figure from (IPCC, 2012).

The most promising geological storage sites are saline aquifers – underground sedimentary rock formations saturated with brine. Saline aquifers are able to provide an estimated storage capacity of between 1,000 and 10,000 billion tonnes of CO_2 (IPCC, 2012) and are therefore larger and also more widespread than other sequestration options such as depleted oil and gas reservoirs (Orr, 2009). The equipment and technology required to inject CO_2 into deep saline aquifer is already widely used in the oil and gas industries and the salinity of the brine means that no potable water resources are compromised by storing CO_2 in these formations. The risks associated with geological CO_2 storage projects are related to leakage of CO_2 from the storage formation to the atmosphere or to other formations where it may cause pollution. However, the expected rates of leakage are in general very small and careful site selection can help mitigate the chances of such an event occurring.

It is for the reasons given above that the focus of this work is on the geological storage of CO_2 in saline aquifers. In order to ensure safe, long term storage of CO_2 it is necessary to understand the different trapping mechanisms that are involved. A detailed discussion of these mechanisms is provided in the next chapter along with a review of previous relevant work in this field.

2 LITERATURE REVIEW

The geological sequestration of carbon dioxide in saline aquifers has been identified as the most promising way of permanently storing CO_2 in an effort to reduce atmospheric emissions and mitigate climate change, due to the abundance and large storage capacity of these formations. The different structural and non-structural trapping mechanisms by which CO_2 can be stored underground are outlined in section §2.1. A review of the research and literature that has been published to help understand and characterise these trapping mechanisms is performed in section §2.2 and an overview of this thesis is given in section §2.3.

2.1 CO_2 TRAPPING MECHANISMS

At standard atmospheric conditions, CO_2 is a gas, slightly heavier than air, with a density of approximately 2 kg m^{-3}. At supercritical conditions, CO_2 retains some of its gas-like properties such as the ability to occupy the entire available volume, but is also liquid-like with a high density (Bachu, 2008). During sequestration, industrial CO_2 is injected into a deep saline aquifer under supercritical conditions to occupy a smaller volume in the subsurface and reduce transportation costs (Audigane et al., 2007).

The critical point for CO_2 to transition to its supercritical state is when the temperature of the environment is greater than T_c = 31.1 ^oC and the pressure is greater than P_c = 7.38 MPa. These conditions are found underground at depths ranging from 800 m to 2 km below ground level, depending on the background temperature of the aquifer (Bachu, 2003). At these depths, supercritical CO_2 has a density of approximately 600 kg m^{-3} and is less dense than the surrounding resident brine solution (Huppert and

Neufeld, 2014). This density difference means that the injected CO_2 displaces the surrounding fluid and rises upward through the porous formation. It eventually reaches a cap rock layer, which acts as an impermeable seal and confines the CO_2 inside the formation, preventing further migration towards the surface. The plume of supercritical CO_2 spreads laterally beneath the cap rock forming an immiscible layer above the brine as shown in Figure 1.3.

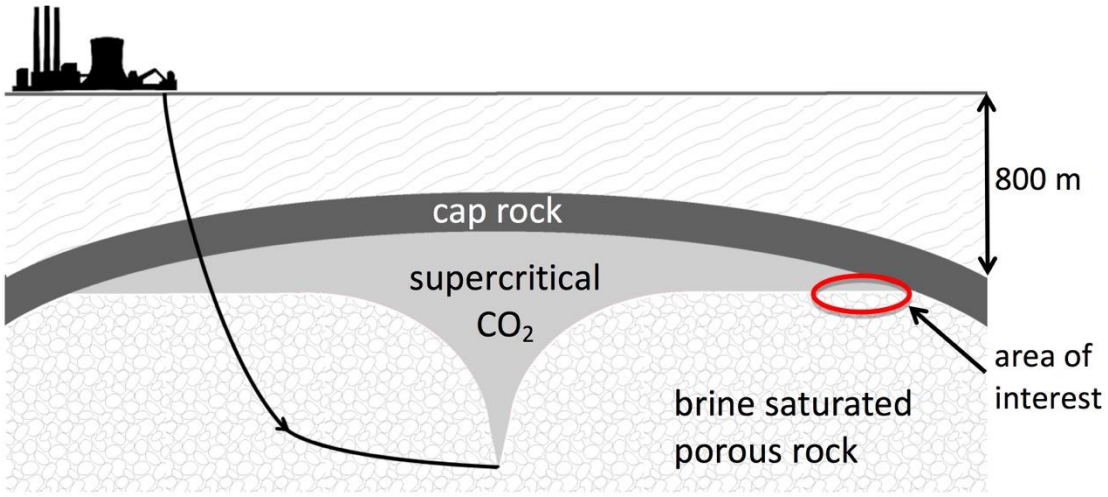

Figure 2.1 Schematic of the injection and structural trapping of supercritical CO_2 in a saline aquifer. Supercritical CO_2 is injected into an anticlinal fold and the resulting plume is physically contained by the domed impermeable cap rock layer.

This containment of CO_2 is commonly referred to as structural, stratigraphic or hydrodynamic trapping. The development and spreading of the supercritical CO_2 plume has been extensively studied to show that it propagates as a gravity current, driven by the pressures of injection and its own buoyancy (Bachu et al., 1994; Neufeld and Huppert, 2009; Nordbotten et al., 2005; Pritchard et al., 2001; Pruess and Nordbotten, 2011; Verdon and Woods, 2007). Given that the CO_2 remains mobile and buoyant beneath the impermeable layer, it is very important to assess the structural integrity of the cap rock as any cracks or fractures can result in the CO_2 leaking back out into the atmosphere or contaminating fresh water aquifers. The longer the supercritical CO_2 remains in contact with the cap rock, the greater the risk of leakage, so it is therefore necessary to immobilise the CO_2 through other trapping mechanisms to ensure safe and long-term storage.

2.1.1 Capillary trapping

Supercritical CO_2 is immiscible with the surrounding fluid and as more CO_2 is injected, it displaces some of the brine in the reservoir pore space. As the plume rises and spreads, the reservoir brine imbibes back into the pores, leaving behind a small amount of CO_2 that becomes permanently immobilised by capillary forces. This process is known as capillary or residual trapping. Theoretical and numerical studies have shown that capillary trapping limits the extent of plume migration and enhances the amount of CO_2 safely stored in an underground reservoir (Hesse et al., 2009; Juanes et al., 2010; Macminn et al., 2010; Woods and Farcas, 2009).

MacMinn et al. (2011) found that for the area of interest considered in this work, circled in Figure 1.3, capillary trapping effects can be ignored as it is the solubility trapping mechanism that primarily acts along the supercritical CO_2 – brine interface.

2.1.2 Solubility trapping

CO_2 is weakly soluble in brine and slowly dissolves across the immiscible horizontal interface, to form an aqueous layer of CO_2-rich brine, which grows by diffusion. This CO_2-rich fluid is heavier than the surrounding brine and the density difference can in turn drive the formation of buoyancy-driven convective instabilities in the diffusive boundary layer (Ennis-King and Paterson, 2005). The denser CO_2-rich solution sinks into the pure brine and is transported away from the interface in the form of negatively buoyant plumes, commonly referred to as convective fingers (Figure 2.2).

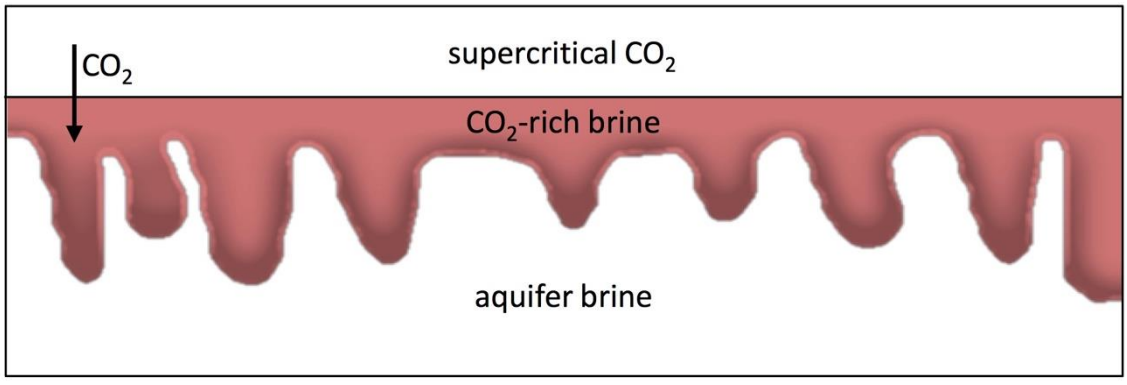

Figure 2.2 Schematic showing a stationary layer of supercritical CO_2 and the dissolution of CO_2 into the underlying brine.

The flow induced by the sinking fluid means that fresh pore water is brought into constant contact with the supercritical CO_2 interface, significantly enhancing the rate of CO_2 dissolution. The dissolution of CO_2 into the pore water removes mobile supercritical CO_2 from the system and traps large volumes of CO_2 within the aquifer, which reduces the risks of leakage from the storage formation. A number of studies have been carried out to investigate and characterise the mechanisms of solubility trapping and a detailed discussion of these works can be found in section §2.2.2.

2.1.3 Mineral trapping

The dissolved CO_2 may also react chemically with the minerals in the formation rock to form ionic species and precipitates (Marini, 2007). The rate at which the stable precipitates are formed is greater than the rate of mineral dissolution, which is why mineral trapping is regarded as the most permanent and secure form of geological storage (Gunter et al., 1997).

The geochemical reactions involved in the mineral trapping process are slow, taking hundreds to thousands of years to immobilise a significant amount of the injected CO_2 (IPCC, 2012). The extent of mineral trapping is expected to be enhanced by the dissolution of CO_2 as convection transports solute to greater reservoir depths and therefore increases the area of reservoir rock in contact with the dissolved species. However, geochemical reactions may also in turn influence the development of convective instability due to the changes in the concentrations of the dissolved species (Ennis-King and Paterson, 2007). Given the importance of solubility and mineral trapping in maximising the storage capacity and security of a geological formation, it is therefore necessary to consider the interplay between chemical reaction and density-driven convection on the behaviour and flow of CO_2 in a saline aquifer.

2.2 REVIEW OF LITERATURE

In this section, previous research and investigations relating to the solubility and mineral mechanisms of CO_2 storage are examined. Extensive analytical, numerical, experimental and field work has been carried out to specifically study the dissolution of CO_2 into brine and the influence of chemical reaction. A number of other investigations have also been performed to determine the effects of reaction, diffusion and convection in different systems. These systems were not directly intended for the purpose of CO_2 storage, but are still considered here as they can aid in developing the understanding of

the interaction of the buoyancy-induced instabilities and chemical kinetics that needs to be taken into account when characterising flow in porous media.

2.2.1 Existing CO_2 storage projects

There are a number of pilot-scale and large-scale projects in operation around the world where industrially captured CO_2 is injected into deep geological formations for storage or used for the purposes of enhanced oil recovery. Only the projects where CO_2 is stored in saline aquifers are considered here.

One of the largest pilot projects in the world is the Ketzin Pilot Site in Germany. After four years of injection, which began in 2008, more than 60,000 tonnes of CO_2 has been safely stored in the deep sandstone formation located west of Berlin (Martens et al., 2013). The pilot-scale activities are used in to test and demonstrate the viability of certain designs and technologies, whilst also providing important information to aid the development of large-scale commercial operations (Global CCS Institute, 2014).

Large-scale CSS projects, by definition, involve the capture, transport and storage of CO_2 at a scale of at least 400,000 tonnes of CO_2 per year. An overview of the commercial projects currently in operation is provided in Table 2.1.

Table 2.1 Overview of current large-scale deep saline aquifer storage projects.

Project name	Country	Industry	Injection rate (10^9 kg CO_2 $year^{-1}$)	Operating since
Sleipner CO_2 Injection	Norway	Natural gas processing	0.9	1996
Snøhvit CO_2 Injection	Norway	Natural gas processing	0.7	2008
Quest	Canada	Hydrogen production	1.0	2015
Illinois Industrial CCS	United States	Industrial separation	1.0	2017
Gorgon CO_2 Injection	Australia	Natural gas processing	3.4-4.0	2017

The Gorgon CO_2 Injection project in Western Australia is the largest greenhouse gas mitigation project in the world, with annual emissions at the natural gas processing facility expected to be reduced by approximately 40% (Global CCS Institute, 2014). However, not all projects have been successful. In 2004, injection began at the In Salah oil field in Algeria and seventeen million tonnes of CO_2 were expected to be stored over the lifetime of the project. Unfortunately, injection had to be suspended in 2011 due to concerns over the integrity of the cap rock seal, with a total of just under four million tonnes of CO_2 successfully stored in the formation (Global CCS Institute, 2014). The changing political environment and socioeconomic factors have also resulted in a number of previously planned projects being cancelled as their required funding needed to be reallocated elsewhere.

Despite the fact that there are several CCS projects already being implemented globally, the number of large-scale projects has to greatly increase in order to result in a significant reduction in the amount of CO_2 emitted to the atmosphere. A greater understanding of the processes and mechanisms in play during storage is required before the necessary extent of large-scale CCS technology is deemed feasible and deployed world-wide.

Deep saline aquifers are generally not as geologically well explored as other underground formations of interest to the hydrocarbon and mining industries. Before a potential storage formation is selected, it is important to know the geophysical properties of a reservoir as these properties can vary from site to site. For example, the Utsira sandstone aquifer at the Sleipner site has an average vertical permeability of approximately 2,000 mD (Chadwick et al., 2008), which is much greater than 1 mD, the permeability of the carboniferous sandstone in the Krechba formation at In Salah (Lopez et al., 2011). It is necessary to assess how such differences in geophysical properties can affect the trapping mechanisms and the amount of CO_2 that can be stored in a given sequestration site. The geological storage system processes can be very slow, lasting hundreds of years, which means predicting their long term behaviour cannot be done solely by monitoring active storage projects in the field (Balashov et al., 2013). It is therefore necessary to perform theoretical studies using numerical simulations and analogue experimental systems in order to model the long term effects and different storage scenarios.

2.2.2 Investigations of convective dissolution in porous media

The interface between the supercritical CO_2 layer and the underlying aqueous brine is considered to be sharp and horizontal, as shown in Figure 2.2, when thermodynamic equilibrium is established (Riaz and Cinar, 2014). Although the equilibrium solubility of CO_2 in brine has been studied extensively, not all models extend to the supercritical temperature and pressure conditions found in deep underground storage reservoirs. Activity coefficient models developed by Duan and Sun (2003) and Spycher et al. (2003) found that the aqueous solubility of CO_2 decreases with rising temperature, but increases sharply with rising pressure. Portier and Rochelle (2005) and Nomeli et al. (2014) then used these models to further show that CO_2 solubility decreases with increasing salinity of the aqueous brine. Portier and Rochelle (2005) compared the solubility of CO_2 predicted by their model with measurements from the Sleipner storage site and the results were found to be in good agreement. The temperature, pressure and salinity of the brine must be carefully considered for each storage site as these factors affect the aqueous solubility of CO_2 and therefore the density of the CO_2-rich brine layer.

If the density difference between the CO_2-rich brine and the surrounding aquifer fluid is sufficiently great, then buoyancy-driven convection occurs in the system. Convection increases the rate of dissolution and therefore decreases the time scale over which there is a risk of leakage of mobile supercritical CO_2. It is therefore important to develop ways to estimate the time for onset of convection during the large scale geological storage of CO_2 at a particular sequestration site (IPCC, 2012). Theoretical and numerical studies model the aquifer system as an idealised, two-dimensional porous medium and the dynamics can be characterised by the Rayleigh number, Ra, which is the ratio of the timescales of convective and diffusive transport. Slim and Ramakrishnan (2010) conducted a linear stability analysis study to show that for an immiscible two-layer system, convective instability is possible only when the system's Rayleigh number is greater than the critical value of 32.5. Prior to the onset of convection, the dissolution of CO_2 across the interface occurs purely by diffusion and the solute-rich boundary layer grows in proportion to the square root of time. Neutral stability curves for a given system can be calculated by linear stability analysis and the minimum of such curves gives the critical time at which convective instability is induced. The results for the time for onset of convection determined by linear stability studies are summarised in Table 2.2.

It is possible to further characterise the pattern of the convective instability by calculating the initial wavelength of the instabilities. Some studies provide this result in terms of the dimensionless wavenumber a' which is inversely proportional to the dimensionless wavelength of instability $\lambda' = 2\pi/a'$. To ensure consistency and easy comparison between studies, Table 2.2 summarises the results in terms of the dimensionless wavelength λ'. Dimensionless quantities are used to generalise the behaviour observed in each study to aid the application of the results to other dynamically similar systems.

Table 2.2 Summary of results from linear stability analysis for the dimensionless time for onset of convection t_{oc}' and the initial wavelength of convective instability λ' in inert systems.

Source	t_{oc}'	λ'
(Slim and Ramakrishnan, 2010)	48	120
(Cheng et al., 2012)	48	110
(Lindeberg and Wessel-Berg, 2011)	49	110
(Hassanzadeh et al., 2006)	60-130	130
(Ennis-King et al., 2005)	75	95
(Xu et al., 2006)	75	97
(Ennis-King and Paterson, 2005)	78	92
(Javaheri et al., 2009)	140	140
(Riaz et al., 2005)	150	90
(Kim and Choi, 2012)	170	91

It is not possible to evaluate the behaviour of the flow after the onset of convection by linear stability alone. To analyse the long-term evolution of the unstable modes predicted by linear stability, it is necessary to perform numerical simulations (Riaz et al., 2005). Direct numerical simulations can estimate the dissolution flux of CO_2 into the underlying brine. Initially, the flux decreases diffusively inversely proportional to the square root of time until it reaches a minimum. After this point, the flux begins to increase as convection dominates over diffusion and negatively-buoyant plumes become apparent. The time at which this minimum flux is reached marks the time for onset of convection and the results from numerical simulations are summarised in dimensionless form in Table 2.3.

Table 2.3 Summary of results from direct numerical simulations for the dimensionless time for onset of convection t_{oc}' in inert systems.

Source	$\boldsymbol{t_{oc}'}$
(Ghesmat et al., 2011)	850
(Andres and Cardoso, 2011)	1,100
(Slim, 2014)	1,200
(Pau et al., 2010)	1,800-3,700
(Riaz et al., 2005)	2,000
(Hassanzadeh et al., 2005)	2,300
(Farajzadeh et al., 2007)	2,500
(Cheng et al., 2012)	3,100
(Elenius and Johannsen, 2012)	4,900
(Hidalgo and Carrera, 2009)	5,600

The dimensionless onset times calculated from direct numerical simulations are approximately an order of magnitude greater than the times predicted by linear stability analysis. This is due to the difference in how the onset time is defined by each method. Linear stability measures the onset of critical instability, however at this point diffusion is still the dominant form of mass transfer and convection is negligible in comparison. As the convective instability grows, the dissolution flux in the system eventually transitions from the diffusive to the convective mass transfer regime, and this transition point marks the onset of convection measured by direct numerical simulations. The results calculated by numerical simulations are of a greater practical relevance to determining the fate of the supercritical CO_2 stored in the field. This is because the numerical time for onset of convection marks the point at which the rate of mass transfer of CO_2 into the aqueous brine, and by definition, the extent of solubility trapping is enhanced.

The variation in the numerically determined onset times in Table 2.3 is due to the differences in the analytical approach and the nature and amplitude of the initial perturbations used by each numerical model. The longest onset time was calculated by Hidalgo and Carrera (2009), which suggests that the value of the onset time is greater when the initial perturbations originate from numerical errors instead of physical perturbations. Indeed, Pau et al. (2010) showed that the onset time is delayed by a factor of two when the perturbations necessary to initiate instability arise due to numerical errors ($t_{oc}' = 3{,}700$) rather than small scale variations in permeability ($t_{oc}' = 1{,}800$).

The dissolution of CO_2 into aqueous solutions has also been investigated experimentally at the laboratory scale using a transparent Hele-Shaw cell to help visualise the flow (Faisal et al., 2015; Kneafsey and Pruess, 2010, 2011; Mojtaba et al., 2014; Outeda et al., 2014; Vosper et al., 2014). Convection was found to significantly accelerate the dissolution of CO_2 and comparisons between experiments and theory showed similar trends in the development of the fingers over time (Faisal et al., 2015; Vosper et al., 2014). Despite the agreement in the trends shown, experimental results were found to overestimate the timescales predicted by numerical simulations (Chevalier et al., 2015; Kneafsey and Pruess, 2010, 2011). The aqueous CO_2 is acidic in water and the dissolution patterns can be detected by a colour indicator sensitive to changes in pH (Parker et al., 2006), however Outeda et al. (2014) note that changes in the indicator concentration have an effect on the observed convective finger pattern. The presence of pH indicators was also found to influence the development of buoyancy-driven

instabilities in the investigations of acid-base reactions fronts carried out by Almarcha et al. (2010) and Kuster et al. (2011). Recently, Thomas et al. (2015) studied the effect of pH indicators in experimental studies of CO_2 convective dissolution in aqueous solutions. They concluded that for the indicator to have no substantial impact on the development of the dynamics, the indicator has to be carefully chosen to capture the full extent of the fingers over the pH range expected for each experimental case.

Yang and Gu (2006) performed experiments at elevated pressures and temperatures to replicate aquifer conditions, however they were unable to study the long-time behaviour of the mass transfer of CO_2 into water as their experiments were too short. Other experimental studies used analogue systems where CO_2 is replaced by another fluid to further investigate the effects of convective mixing on the mass transfer of solute at the interface. Slim et al. (2013) performed experiments to study the convection of potassium permanganate. The colour of the aqueous permanganate made it possible to track the convective patterns and infer concentration from the intensity of the transmitted light. After the onset of convection, convective fingers were observed to grow and propagate downwards, whilst also merging together when neighbouring fingers got sufficiently close to each other. Eventually the sinking fingers were found impact the bottom boundary, resulting in the decay of the dissolution flux as the system entered the convective shutdown regime.

The flux was also measured experimentally using a water – methyl ethylene glycol (Neufeld et al., 2010) and water – propylene glycol (Backhaus et al., 2011; Tsai et al., 2013) analogue systems. After convection was established, the rate of dissolution was observed to enter a regime of constant flux where the dense solute is removed and redistributed from the interface by convection. This constant flux regime can be characterised for the different systems using a scaling relationship between the Sherwood and Rayleigh numbers shown in Table 2.4. A power law relationship was observed for the experimental analogue systems with a Rayleigh number exponent equal to approximately 0.8, consistent with the numerical simulations carried out by Farajzadeh et al. (2013). However, this sublinear scaling is different to the results of the theoretical studies in Table 2.4, which yield a linear relationship between the Sherwood and Rayleigh numbers in the regime of constant mass flux. The difference in the results can be attributed to the method by which the flux was measured, i.e., if it was inferred or measured directly (Riaz and Cinar, 2014).

Table 2.4 Summary of results from direct numerical simulations and experimental studies for the mass transfer scaling relationship between the Sherwood and Rayleigh numbers during the constant flux regime in inert systems.

Source	Scaling relationship
(Pau et al., 2010)	$Sh = 0.017Ra$
(Elenius and Johannsen, 2012)	$Sh = 0.02Ra$
(Slim, 2014)	$Sh = 0.017Ra$
(Ward et al., 2015)	$Sh = 0.017Ra$
(Neufeld et al., 2010)	$Sh = 0.12Ra^{0.84}$
(Backhaus et al., 2011)	$Sh = 0.045Ra^{0.76}$
(Tsai et al., 2013)	$Sh = 0.037Ra^{0.84}$
(Farajzadeh et al., 2013)	$Sh = 0.079Ra^{0.83}$

2.2.3 Effect of chemical reaction on flow in porous media

After carbon dioxide is dissolved in brine, it forms carbonic acid, H_2CO_3, some of which dissociates to release H^+ ions and therefore lowers the pH of the solution according to the following equilibrium reactions

$$CO_2 + H_2O \rightleftharpoons H_2CO_3 \tag{2.1}$$

$$H_2CO_3 \rightleftharpoons H^+ + HCO_3^- \tag{2.2}$$

$$HCO_3^- \rightleftharpoons H^+ + CO_3^{2-} \tag{2.3}$$

The most common candidate formations for geological storage consist of sandstone and carbonates (Kim and Santamarina, 2014). Mineral trapping reactions result in the precipitation of calcite, siderite, magnesite and dolomite (White et al., 2003; Xu et al., 2004).

$$Ca^{2+} + CO_3{}^{-} \rightleftharpoons CaCO_3 \quad (2.4)$$

$$Fe^{2+} + CO_3{}^{-} \rightleftharpoons CaCO_3 \quad (2.5)$$

$$Mg^{2+} + CO_3{}^{-} \rightleftharpoons CaCO_3 \quad (2.6)$$

$$Mg^{2+} + Ca^{2+} + 2CO_3{}^{-} \rightleftharpoons CaMg(CO_3)_2 \quad (2.7)$$

Ennis-King and Paterson (2007) used analytical and numerical techniques to investigate the effect of coupling of geochemical reactions with convective mixing of dissolved CO_2 during storage. Slow reactions with timescales much greater than the convection of CO_2 have been found to have little influence on the fluid motion, whilst fast acting reaction can either stabilise or enhance convection by altering the density profile of the solution. Precipitation reactions between CO_2-rich brine and solid phase minerals consume and withdraw CO_2 from solution, decreasing the density difference driving instability. Ennis-King and Paterson (2007) found that such systems obeyed first-order reaction kinetics and reaction was found to stabilise the convective fluid motion compared to that in an inert system. This is consistent with the findings of previously carried out theoretical studies and numerical simulations, which quantified the stabilising effect of reaction (Andres and Cardoso, 2011, 2012; Ghesmat et al., 2011; Kim and Choi, 2014; Pritchard and Richardson, 2007; Ritchie and Pritchard, 2011; Ward et al., 2014a, 2014b). Reaction was found to significantly influence the dynamics of the system, resulting in the delay in the time for onset of convection, stabilisation of the diffusive boundary layer and the inhibition of finger growth. Ghesmat et al. (2011) noted that the increase in stability due to reaction could be characterised using the dimensionless Damköhler number. Andres and Cardoso (2011, 2012) grouped this dimensionless number together with the Rayleigh number into the term Da/Ra^2, which was identified as the single parameter that governs the flow, transport and chemical kinetics of CO_2 in their system. As Da/Ra^2 was increased, the stabilising effect of reaction was found to also increase, with no convection observed when Da/Ra^2 exceeded the critical value of 3.5×10^{-3}. These observations were applied together with results from experiments to show that chemical reaction with silicate-rich rocks may inhibit the transport of convective fingers of CO_2 in an aquifer (Cardoso and Andres, 2014). The stabilisation of convection means that the full extent of the reservoir may

remain unused as the downward motion of CO_2-rich brine is curbed by reaction (Audigane et al., 2007).

The effect of chemical reaction on the hydrodynamics in pattern formation has been the focus of many recent studies investigating the behaviour of propagating reaction fronts (D'Hernoncourt et al., 2007; Rongy et al., 2008, 2010) and two layer miscible systems (Carballido-Landeira et al., 2013; De Wit, 2001, 2004; Lemaigre et al., 2013; Trevelyan et al., 2008, 2011; Zalts et al., 2008). Budroni et al. (2014) performed experiments using a partially miscible system to study the convective dissolution of an ester into an underlying aqueous phase solution. The introduction of an alkaline hydroxide to the aqueous solution was found to result in the formation of a less dense salt and the stabilisation of convection.

Immiscible systems have been studied experimentally using a vertically-orientated Hele-Shaw cell, where a less dense organic layer overlies an aqueous layer. In the experiments performed by Eckert and Grahn (1999) and Eckert et al. (2004) a carboxylic acid (solute *A*), initially dissolved in the upper organic layer, diffuses into the lower aqueous layer where it gives rise to density driven, Rayleigh-Taylor instabilities and also undergoes a simple $A + B \rightarrow C$ neutralisation with an aqueous base (reactant *B*) to form the soluble salt *C*. Acid-base neutralisation is an exothermic process with enthalpy of approximately –57 kJ mol^{-1} and the heat evolved may give rise to thermal instabilities that influence the behaviour of the chemo-hydrodynamic pattern. However, this system was modelled by Bratsun and De Wit (2011), who calculated the thermal Rayleigh number to be much smaller than the solutal one meaning that the dynamics are controlled by solutal effects. When this is the case, thermal effects can be ignored, consistent with the work carried out by Almarcha et al. (2010), who found that heat diffuses much faster than mass and so the contribution of heat can therefore be neglected.

The effect of the orientation of the Hele-Shaw cell on pattern formation was investigated by Eckert et al. (2004) who found that tilting the cell from vertical to horizontal, reduced the velocity of the reaction front, increased the wavelength of the pattern and delayed the onset of Rayleigh-Taylor instability. Using the same reactive system, Shi and Eckert (2006) noted that for a cell in a fully horizontal orientation, no buoyancy driven convection was observed. Instead mass transfer across the interface gave rise to a planar reaction diffusion front.

The spatio-temporal dynamics observed in these experiments were numerically modelled by Bratsun and De Wit (2011) by coupling the Navier-Stokes flow velocity equations with reaction-diffusion-convection equations for the concentrations of the chemical species. Convective fingers in the lower aqueous layer were observed as a result of Rayleigh-Taylor instabilities caused by the diffusive boundary layer of solute *A* overlying the less dense bulk solution. This lower layer convection was found to increase the amplitude of the stream function and the mass transfer of *A* through the interface. Convective plumes were also found to occur in the upper layer originated due to a diffusive layer mechanism (Trevelyan et al., 2011) where the transfer of acid to the aqueous layer resulted in an acid rich region overlying an acid depleted region within the upper organic layer itself. With increasing strength of reaction, the formation of product *C* brought about several complications in the observed patterns. This was due to the fact that in this particular system, the density of *C* is lower than that of either *A* and *B*, so as reaction proceeded, the formation of the lighter *C* was found to locally stabilise the system and reduce the intensity of the instability. It was observed that by increasing the initial concentration between the acid and base, the growth rate of convective fingering also increased. Increasing the Damköhler number had the reverse effect on the growth of the fingers due to the stabilising formation of product *C*. A comprehensive quantitative comparison between the numerical model and the experiments could not be fully carried out as the value of the kinetic rate constant of reaction remains unknown for this system.

Recently, Loodts et al. (2014, 2015) and Trevelyan et al. (2015) classified the possible convective instability scenarios that arise when an $A + B \rightarrow C$ aqueous reaction takes place and the density of the solution varies with the concentration of the different chemical species. Chemical reaction can modify the density profiles and thus the convective dynamics compared to the inert case with no reaction. The stabilising effect of reaction has been discussed above, however reactions can also play a destabilising role and enhance convection by forming a soluble product *C* that is denser than the reactants.

Wylock et al. (2014) conducted experiments and numerical simulations to study the absorption of gaseous CO_2 by an aqueous solution of monoethanolamine at standard laboratory conditions. The aqueous phase reaction was found to induce convective motion in the form of negatively-buoyant plumes sinking monotonically into the bulk solution and significantly enhance the rate of mass transfer of solute. However, in their

work the Damköhler number remained fixed at 15, so the effect of this governing parameter on the convective dissolution behaviour is unknown and there is therefore no possibility of understanding the behaviour in a real CO_2 reservoir for which the Damköhler number will be different.

The dissolution of gaseous CO_2 into an aqueous solution of sodium hydroxide has also been investigated experimentally by Loodts et al. (2014). Upon dissolution, CO_2 reacts with the hydroxide to form aqueous sodium carbonate which has a greater solutal expansion coefficient than the reactants. Convective fingers were shown to sink monotonically and develop faster as the concentration of sodium hydroxide was increased. However, besides such qualitative descriptions there is a lack of experimental results quantifying the destabilising impact of chemical reaction.

2.3 OUTLINE OF THESIS

This work contributes to the next step in understanding how chemical reactions modify the density of the fluid and the flow of a solute in a porous medium, inducing instabilities and fluid motion that would not otherwise occur in an inert system. In particular, the destabilising scenario where the product of a second-order chemical reaction between the diffusing solute and a uniformly distributed aqueous reactant remains in solution and has a greater density than the surrounding fluid is addressed.

A theoretical model that incorporates the effects of diffusion, convection and reaction on the fluid flow in a two-dimensional homogenous, isotropic porous medium is described in the next chapter. It is shown that for a given physicochemical system, the fluid flow is governed by the initial concentration of the environmental reactant species relative to the concentration of the solute, and also a ratio of the Damköhler and Rayleigh numbers.

The effect of these dimensionless parameters on the development of instability is analysed in the laboratory using an analogue system that mimics the flow of CO_2 in a saline aquifer. Details of the experimental apparatus, components and the image processing techniques are provided in chapter 4 and then in the following chapter the results for the inert case with no reaction are compared to those from previous work to test the validity of this system as a suitable analogue. The experimental observations are quantitatively analysed to determine the convective onset time and to characterise the growth and interaction of the fingering instability. In order to experimentally measure the rate of mass transfer of solute into the solution, a colorimetric technique is

developed which converts the information carried by the laboratory image pixels to calculate the concentration of the chemical species dissolved in solution.

The destabilising effect of reaction on the dissolution of solute and the evolution of the convective fingers is examined in chapter 6 for the experimental system. Conditions are identified for which the development of instability is accelerated and the transport of solute is enhanced. The analogue physicochemical system is then modelled numerically and the results of the experiments and numerical simulations are compared using nondimensional groups to ensure dynamic similarity.

The effect of a destabilising chemical reaction between CO_2 and aqueous sodium hydroxide in a real world sequestration scenario is analysed in chapter 7. Numerical simulations are performed to estimate the effect that the initial concentration of sodium hydroxide dissolved in the aquifer may have on the trapping of CO_2 in the Utsira Sand formation at Sleipner and to show the different factors that must be considered when selecting an effective geological storage site. The assumptions and limitations of the numerical model are discussed. Finally, the conclusions of this work are presented together with recommendations for future research to build on the results of this investigation and develop further the understanding of this topic.

3 THEORY

The equations used to describe the flow of CO_2 in a saline aquifer coupled with a second-order chemical reaction are presented in section §3.1 together with the initial and boundary conditions of the model. The nondimensional scaling used to determine the parameters which govern the system is outlined in section §3.2 and in §3.3, analytical solutions are found for the destabilising effect of chemical reaction for the limiting case where the reaction is instantaneous.

3.1 GOVERNING EQUATIONS

The saline aquifer system is modelled as a two-dimensional homogenous, isotropic porous medium. Supercritical CO_2, solute *A*, is present in an immiscible layer above the two-dimensional domain with horizontal and vertical length-scales L_x and L_z respectively. The gravity field g points downwards, along the vertical *z*-axis and perpendicular to the horizontal *x*-axis. Local chemical equilibrium between the two phases is assumed so that the total concentration of the solute species at the interface is considered to remain constant and equal to C_{As} the aqueous solubility of *A*. As solute *A* dissolves into the underlying fluid, it reacts with reactant *B*, present with initial concentration C_{Bo}, and undergoes an irreversible second-order chemical reaction to form product *C*. The chemical species are all soluble in the domain and remain in solution and the reaction follows:

$$A_{(aq)} + B_{(aq)} \rightarrow C_{(aq)} \tag{3.1}$$

The rate of reaction can be expressed as $k_r C_A C_B$, where k_r is the kinetic rate constant, with SI units equal to mol m^{-3} s^{-1}, and C_i is the concentration of chemical species i in the aqueous solution. Species B and C are insoluble in the upper phase and therefore the focus is on the dynamics in the lower phase only.

The domain and the boundary conditions for the system are outlined in Figure 1.1. It is assumed that the interface remains at the same position $z = 0$ over time, that the volume of the domain does not change significantly with the dissolution of A and that thermal and dispersion effects are negligible.

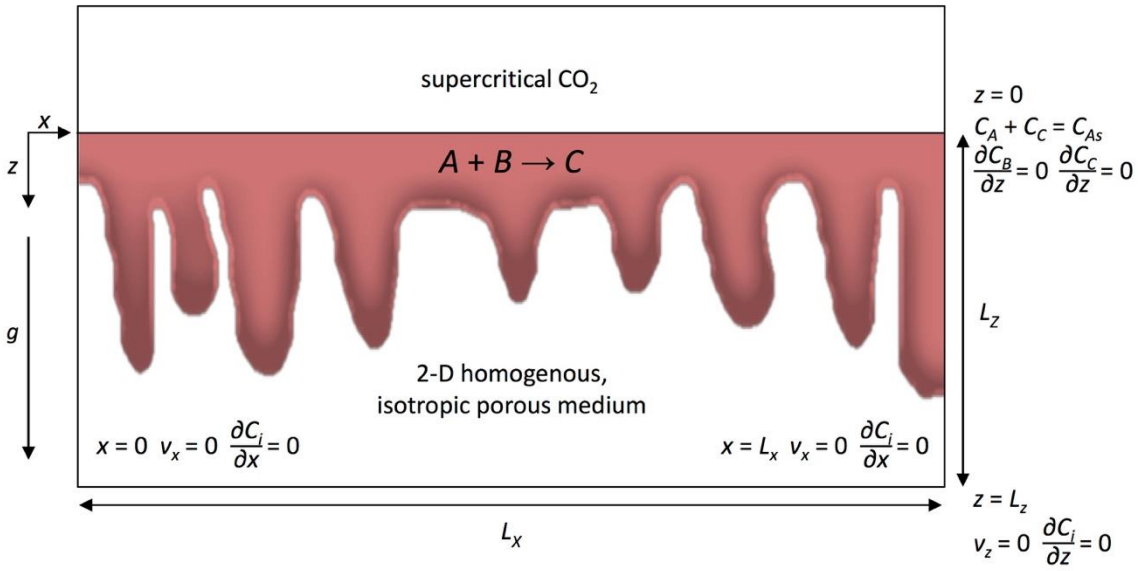

Figure 3.1 The system is modelled as a two-dimensional porous medium with a horizontal interface between the supercritical CO_2 and the underlying brine. The dissolution of CO_2, solute A, results in convective fingers (shaded red) that sink into the domain. The total concentration of solute A that remains dissolved and that has reacted with B to form product C is equal to C_{As} at the top boundary. There is no fluid flow across the bottom of the domain and its walls at all times.

The fluid is assumed to be incompressible and the dynamics of the system are described using the equations previously used by Ennis-King and Patterson (2007): the continuity equation (3.2), Darcy's law (3.3) and the conservation of the dissolved species with concentration C_i, $i = A, B, C$, equations (3.4) – (3.6).

$$\nabla \cdot \mathbf{v} = 0 \tag{3.2}$$

$$\mathbf{v} = -\frac{k}{\mu}(\nabla p - \Delta\rho_0 g \mathbf{i}) \tag{3.3}$$

$$D_A\phi\nabla^2 C_A - \mathbf{v}\cdot\nabla C_A = \phi\frac{\partial C_A}{\partial t} + k_r C_A C_B \tag{3.4}$$

$$D_B\phi\nabla^2 C_B - \mathbf{v}\cdot\nabla C_B = \phi\frac{\partial C_B}{\partial t} + k_r C_A C_B \tag{3.5}$$

$$D_C\phi\nabla^2 C_C - \mathbf{v}\cdot\nabla C_C = \phi\frac{\partial C_C}{\partial t} - k_r C_A C_B \tag{3.6}$$

The fluid viscosity μ and permeability of the medium k are assumed to be constant. Here, $\mathbf{v}$ is the fluid superficial velocity vector and the reduced pressure $\nabla p = P - \rho_0 g\mathbf{i}$ is taken to be the difference between the pressure in the liquid P and the hydrostatic pressure. Under the Boussinesq approximation, variations in all fluid properties other than density are ignored (Tritton, 1977) and density changes are considered by the buoyancy term $\Delta\rho_0 g\mathbf{i}$ where $\mathbf{i}$ is vertical unit vector co-directional with the positive z-axis. This approximation is valid as the density changes due to CO_2 dissolution are small enough in comparison with the density of the pure pore water fluid, with $\frac{\Delta\rho_0}{\rho_0} \approx 1\%$ (Teng, 1998), satisfying the condition for incompressibility. The density of the aqueous solution ρ is taken to be linearly dependent on concentration C_i so that

$$\rho = \rho_0 + \beta_A C_A + \beta_B C_B + \beta_C C_C \tag{3.7}$$

where ρ_0 is the reference density of the pure fluid and $\beta_i = (\partial\rho/\partial C_i)$ is the solutal expansion coefficient of species i. The density change $\Delta\rho_0 = \rho - \rho_0$ in the buoyancy term can therefore be expressed as $\Delta\rho_0 = \sum \beta_i C_i$.

The conservation of chemical species in equations (3.4) – (3.6) is the balance between the diffusive flux $D_i\phi\nabla^2 C_i$, convective flux $\mathbf{v}\cdot\nabla C_i$ and the accumulation $\phi\frac{\partial C_i}{\partial t}$ and reaction $k_r C_A C_B$ terms. Time is denoted by t, tortuosity is neglected and the effective diffusivity of the dissolved species is taken as the product of the porosity ϕ of the aquifer and the molecular diffusion coefficient D_i. It is assumed that A, B and C have the same diffusion coefficient so that $D_A = D_B = D_C = D$. No heat transport equations have been included as the system is considered to be isothermal.

The domain is initially free of solute A and product C so that for $z > 0$, $(C_A, C_B, C_C) = (0, C_{Bo}, 0)$ where C_{Bo} is the initial concentration of reactant B uniformly distributed in the aqueous phase. The total concentration of solute at the top boundary is equal to C_{As} and there is no flow across the walls and the bottom boundary at all times.

3.2 NONDIMENSIONALISATION

The use of dimensionless quantities generalises the behaviour of the CO_2 in the saline aquifer system to other analogue systems with dynamic similarity. Equations (3.2) – (3.6) can be written in dimensionless form (Rees et al., 2008, Andres and Cardoso, 2011) by scaling the variables using the length scale $L_s = \mu D\phi/(k\beta_A C_{As} g)$, velocity scale $v_s = D\phi/L_s$, time scale $t_s = {L_s}^2/D$, pressure scale $p_s = \mu D\phi/k$, concentration scale C_{As} and the solutal expansion coefficient scale β_A, which is the solutal expansion coefficient of solute *A* in the fluid, giving

$$\nabla' \cdot \mathbf{v}' = 0 \tag{3.8}$$

$$\mathbf{v}' = -\nabla' p' + \sum \beta_i' C_i' \mathbf{i} \tag{3.9}$$

$$\nabla'^2 C_A' - \mathbf{v}' \cdot \nabla' C_A' = \frac{\partial C_A'}{\partial t'} + \frac{\mathrm{Da}}{\mathrm{Ra}^2} C_A' C_B' \tag{3.10}$$

$$\nabla'^2 C_B' - \mathbf{v}' \cdot \nabla' C_B' = \frac{\partial C_B'}{\partial t'} + \frac{\mathrm{Da}}{\mathrm{Ra}^2} C_A' C_B' \tag{3.11}$$

$$\nabla'^2 C_C' - \mathbf{v}' \cdot \nabla' C_C' = \frac{\partial C_C'}{\partial t'} - \frac{\mathrm{Da}}{\mathrm{Ra}^2} C_A' C_B' \tag{3.12}$$

The length scale of the system is sufficiently small so that the change in parameters with height is negligible and the criteria for the Boussinesq approximation are satisfied (Tritton, 1977). The initial conditions are that the entire domain is quiescent, i.e., $\mathbf{v}'(x', z', t' = 0)$, and that it is solute and product free for $\forall x', z' > 0$, $(C_A', C_B', C_C') = (0, C_{Bo}', 0)$ where $C_{Bo}' = C_{Bo}/C_{As}$ is the ratio between the initial concentration of reactant *B* and the solubility of solute *A* in the aqueous phase. When $C_{Bo}' = 0$, the inert case is recovered which describes the dissolution of CO_2 into pure brine with no reaction. At the upper boundary $z' = 0$, it is set that the total concentration of solute derived species $C_{AT}' = C_A' + C_C' = 1$ and the downward fluid vertical velocity is assumed to be negligible so that $v_z' = 0$. The boundary conditions are $v_x' = 0$ and $\partial C_i'/\partial x'$ at the walls $(x' = 0, L_x/L_s)$, and $v_z' = 0$ and $\partial C_i'/\partial z'$ at the bottom $(z' = L_z/L_s)$, at all times.

To determine the amount of solute that can be stored in a given reservoir, it is necessary to calculate the total inward mass flux of solute *A* into the domain. This can be calculated at the top boundary in the absence of vertical flow and is given in dimensional form as

$$J_A = \frac{D\phi}{L_x}\int_0^{L_x} \left.\frac{\partial C_{AT}}{\partial z}\right|_{z=0} dx \tag{3.13}$$

The expression for the flux gives the rate of change of the mass of CO_2 dissolved in brine per unit area of the interface can be nondimensionaled as $J_A' = J_A L_s / D\phi C_{As}$. This provides an important measure of the dissolution process and is used to help characterise geological formations based on their potential storage capacity.

The above analysis suggests that the flow and transport in this system is governed by the following parameters: the dimensionless solutal expansion coefficients of the chemical species β_A', β_B', β_C'; the initial dimensionless concentration of reactant *B*, C_{Bo}'; and the dimensionless parameter

$$\frac{\mathrm{Da}}{\mathrm{Ra}^2} = \frac{k_r C_{As} D\phi}{(k\beta_A C_{As} g/\mu)^2} \tag{3.14}$$

which is the ratio of the Damköhler number $\mathrm{Da} = k_r C_{As} {L_z}^2/(D\phi)$, and the square of the solutal Rayleigh number $\mathrm{Ra} = k\beta_A C_{As} g L_z/(\mu D\phi)$. The Damköhler number is a measure of the relative magnitude of the reaction time scale and the diffusion time scale. A large value of Da indicates that the reaction dominates over diffusion and this is the case for systems with a fast chemical reaction. For the inert case, Da = 0 as there is no reaction. The Rayleigh number is the ratio of the solutal buoyancy forces driving convection to the diffusive forces. Both Da and Ra are defined in terms of the dimensional depth of the domain L_z and this is cancelled out when calculating $\mathrm{Da/Ra}^2$ to show that the vertical extent of the reservoir has no effect on the initial development of convection. This is the case when the reservoir's depth is much greater than the scaling length L_s ($L_z >> L_s$), which corresponds to the thickness of the solute boundary layer at the moment in time when the diffusive and convective effects are of the same magnitude. Thus for the hypothetical scenario where $L_z = L_s$, the Rayleigh number would equal one.

The Rayleigh number is always positive when the dissolution of solute *A* increases the density of the solution, i.e., $\beta_A > 1$, as is the case for CO_2 dissolving in brine. If the dimensional solutal expansion coefficient for *A*, β_A, is negative then the solute rich boundary layer is less dense than the surrounding bulk fluid. The solute-rich layer grows by diffusion only and is thus stable, meaning that convective instabilities do not develop. However, this scenario is not considered in this work as it does not represent the behaviour of CO_2 in an aquifer.

The dimensionless density difference driving buoyancy in equation (3.9) can be expanded to give

$$\Delta\rho_0' = \sum \beta_i' C_i' = \beta_A' C_A' + \beta_B' C_B' + \beta_C' C_C' \qquad (3.15)$$

Taking into account the initial and boundary conditions for species *B* and *C*, equations (3.11) and (3.12) can be added together to show that the concentration of reactant and product remains constant over time and equal to C_{Bo}' the initial concentration of *B* dissolved in the domain. The concentration field for the product *C* can thus be reconstructed according to

$$C_C' = C_{Bo}' - C_B' \qquad (3.16)$$

Given that $\beta_A' = \beta_A / \beta_A$ is always equal to unity and using the expression above for C_C', the density difference can be rewritten as

$$\Delta\rho_0' = C_A' - (\beta_C' - \beta_B')C_B' + \beta_C' C_{Bo}' \qquad (3.17)$$

The density difference for the system is therefore characterised by only three constants: β_B', β_C' and C_{Bo}'. If the parameter $(\beta_C' - \beta_B')$ is positive then the formation of the product of reaction results in the development of a buoyantly unstable density profile. As C_{Bo}' is increased, the destablising effect of reaction and product formation on the development of the dissolution driven instability is expected to be amplified. Using the expression for the density difference it is possible to reconstruct the general reaction-diffusion profiles for the concentration of species *i* and the density of the solution analytically.

3.3 ANALYTICAL SOLUTIONS

For the asymptotic scenario where the reaction between the solute *A* and reactant *B* is assumed to be instantaneous, Da/Ra^2 tends to infinity, and the reaction is confined to a thin region at the interface. Within this reaction zone, where $z' < z_R'$, species *A* and *B* are immediately and entirely consumed by reaction and therefore cannot coexist. The aqueous solutions are assumed to be dilute and to obey Fick's model for diffusion. The Sherwood and Pigford (1956) model was used to find the time-dependent base state solutions to the reaction-diffusion equations (3.10) – (3.12) in the absence of convection to be given as

$$C_{Ab}' = \operatorname{erfc}\left(\frac{\zeta}{2}\right) - C_{Bo}', \quad C_{Bb}' = 0 \quad \text{and} \quad C_{Cb}' = C_{Bo}', \text{ for } z' \le z_R' \qquad (3.18)$$

$$C_{Ab}' = 0,\ \ C_{Bb}' = C_{Bo}' - \text{erfc}\left(\frac{\zeta}{2}\right),\ \text{and}\ \ C_{Cb}' = \text{erfc}\left(\frac{\zeta}{2}\right),\ \text{for}\ z' \geq z_R' \qquad (3.19)$$

where C_{ib}' is the time-dependent, diffusive base state concentration profile for species i and ζ corresponds to the self-similar variable $\zeta = z'/\sqrt{t'}$. The reaction front proceeds as $z_R' = \zeta_R \sqrt{t'}$ and its position can be determined by solving

$$\text{erfc}\left(\frac{\zeta_R}{2}\right) = C_{Bo}' \qquad (3.20)$$

Given that the maximum value of erfc(ζ_R/2) is 1, equation (3.20) shows that the limit of the model is for $C_{Bo}' \leq 1$. The effect of reaction is therefore only investigated for cases where the initial concentration of reactant *B* satisfies this limit.

The total base state concentration of aqueous solute at the interface that has both reacted to form product *C* and that has remained in its unreacted form *A*, is expressed as C_{ATb}' and is set to 1 – the aqueous solubility of the solute (C/C_{As} = 1). The present base state concentration profiles at the interface correspond to $C_{Ab}' = 1 - C_{Bo}'$ for the unreacted solute species and $C_{Cb}' = C_{Bo}'$ for the solute species that have been consumed by reaction to form product *C*. This is different to the boundary condition previously used by Loodts et al. (2015) who set $C_{Ab}' = 1$ at the interface and derived $C_{ATb}' = \text{erfc}(\zeta_R/2) + C_{Bo}'$ as the base state concentration profile for the total concentration of reacted and unreacted solute. The boundary condition employed by Loodts et al. (2015) means that the total concentration of solute derived species is $C_{ATb}' = 1 + C_{Bo}'$ at the interface and thus greater than the aqueous solubility of the solute.

A physicochemical analogue system is introduced in the next chapter to model this problem experimentally. In this system, the solute *A* is a weak acid initially dissolved in an organic layer and as the acid diffuses into the underlying aqueous phase, it dissociates to form ions. It could be argued that at the interface, the acid in the organic layer is in equilibrium with the ions in the aqueous phase so that the dimensionless concentration of solute *A* is $C_{ATb}' = 1$, consistent with the boundary condition proposed in this work.

The position of the reaction front for an instantaneous reaction was plotted in **Figure 3.2** as a function of the initial dimensionless concentration of reactant *B* dissolved in the domain. It can be seen that as C_{Bo}' increases, the reaction zone is confined to a narrower region and the reaction front moves slower towards the bulk fluid in the domain. For the limiting case where $C_{Bo}' = 1$, the reaction front is located at the top boundary interface, where $z' = \zeta = 0$.

The reaction-diffusion concentration profiles of solute *A*, reactant *B* and product *C* given in equations (3.18) and (3.19) were plotted in **Figure 3.3** for different cases of C_{Bo}' ranging from 0 (the inert case with no reaction) to 1 (the upper limit of the model). **Figure 3.3**(a) shows that for the non-reactive case, the concentration profile decreases monotonically as solute *A* enters through the top boundary of the domain and diffuses into the bulk fluid. When the domain contains an initial concentration of reactant *B* in the aqueous phase, the dissolving solute *A* is consumed by the reaction with *B* and the concentration of *A* drops to zero at the reaction front ζ_R. The concentration of *B* is zero between the top boundary and the reaction front, as it has been totally consumed to produce the soluble product *C* with a concentration equal to C_{Bo}'. The total concentration of solute dissolved in the domain and which has reacted to form *C* is equal to 1, satisfying the earlier stipulated boundary condition. Away from the reaction front, the concentration of *B* increases monotonically from 0 to C_{Bo}', its initial value in the bulk solution. The product of reaction is present mainly in the region between the interface and the reaction front, but also extends into the bulk solution for $\zeta > \zeta_R$ by diffusion. **Figure 3.3**(d) shows that when $C_{Bo}' = 1$, the position of the reaction front is at the top boundary where *A* is immediately consumed by reaction at the interface and the solute is therefore stored in the domain only in its product form.

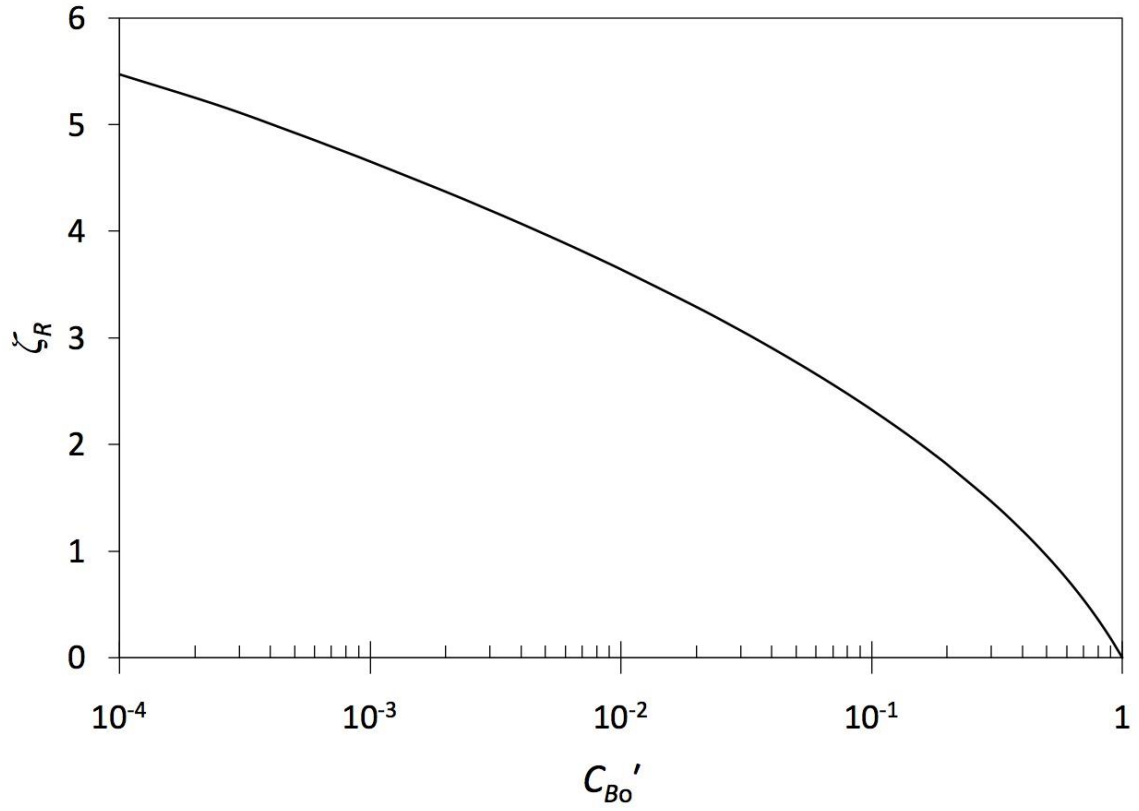

Figure 3.2 Position of the reaction front $\zeta_R = z_R' / \sqrt{t'}$ as a function of C_{Bo}', the dimensionless initial concentration of reactant *B*, for an instantaneous chemical reaction.

The reaction-diffusion concentration and density profiles can be analysed in order to understand how the convective instability may develop in a given physicochemical system. This analysis is now performed for an experimental system that is considered as an analogue model that mimics the flow and storage of CO_2 in a saline aquifer. This system is introduced in detail in the next chapter and has $\beta_B' = -0.9$ and $\beta_C' = 1.8$, which are the parameters required to determine the asymptotic concentration and density profiles.

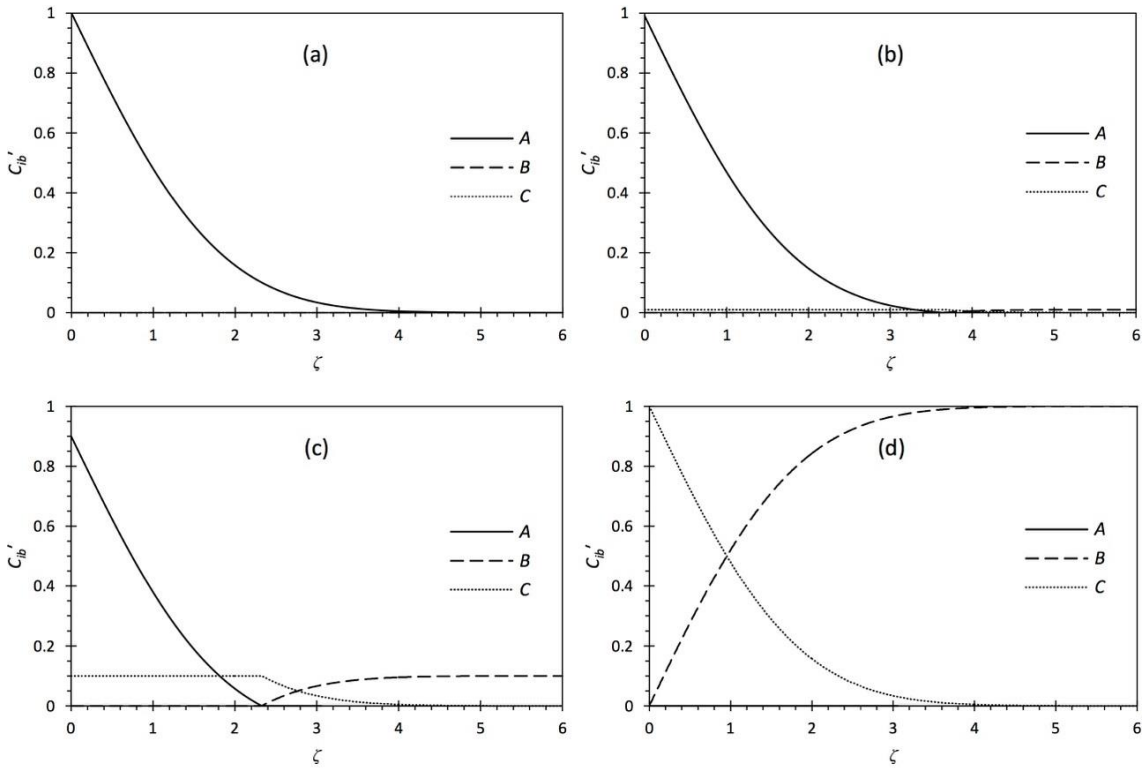

Figure 3.3 Dimensionless base state concentration profiles C_{ib}' of chemical species i = A, B and C when the dimensionless initial concentration of reactant B in the domain is (a) $C_{Bo}' = 0$, (b) $C_{Bo}' = 10^{-2}$, (c) $C_{Bo}' = 10^{-1}$ and (d) $C_{Bo}' = 1$.

Using the expressions for the concentration profiles and the values of β_i' for the experimental analogue system, the profiles showing the density difference between the fluid in the reaction zone and the bulk fluid with concentration C_{Bo}' were calculated and plotted in Figure 3.4. The parameter ($\beta_C' - \beta_B'$) is positive for the system under investigation, therefore the consumption of reactants and the formation of product C increases the global density of the solute-rich fluid compared to the surrounding bulk fluid. The density profile for the inert system with $C_{Bo}' = 0$ in Figure 3.4 is monotonic and decreases along ζ. This is expected as the dissolution of solute A increases the density of the aqueous solution in the domain ($\beta_A > 1$) and the result suggests that the extent of this dense boundary layer grows with time. For the reactive cases, the density difference between the solute rich boundary layer and the bulk fluid is monotonic and increases with increasing C_{Bo}'. This implies that the reactive cases are more unstable than the scenario of inert dissolution of A, and as more solute is converted into the dense soluble product by reaction, the density difference driving the formation of convective instabilities becomes greater.

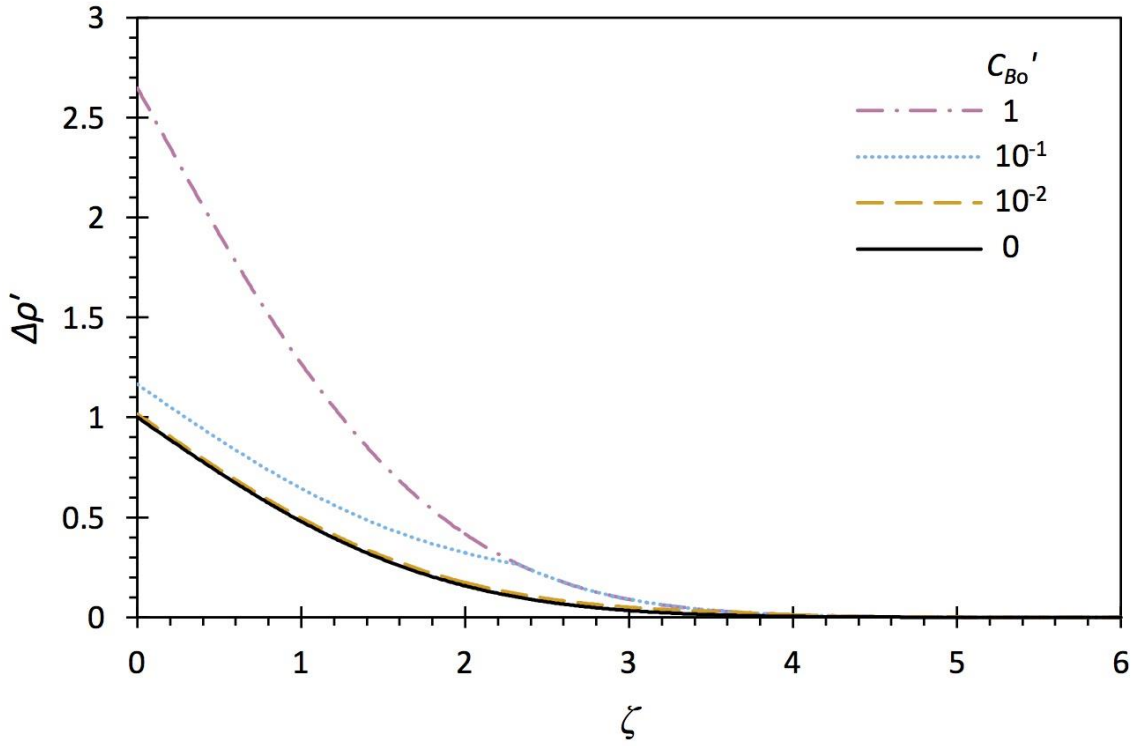

Figure 3.4 Dimensionless profiles of the density difference $\Delta\rho'$ between the solute rich fluid and the bulk solution with concentration C_{Bo}' plotted for the analogue physicochemical system where $\beta_B' = -0.9$ and $\beta_C' = 1.8$.

The analytical solutions presented above show that if the domain is considered to be semi-infinite in depth, then three distinct regions can be identified: the zone between the interface and the reaction front ($0 \leq \zeta \leq \zeta_R$) which is free of reactant *B* and contains only the solute derived species *A* and *C*, the region $\zeta_R \leq \zeta \leq \infty$ where the reactant *B* and product *C* are present and then also the zone far from the reaction front ($\zeta \rightarrow \infty$) where only *B* remains in the bulk solution with concentration equal to its initial concentration in the domain. The analysis is only valid for the asymptotic scenario where the chemical reactions are very fast and $Da/Ra^2 \rightarrow \infty$. The concentration and density profiles suggest that increasing C_{Bo}' increases the density difference in the domain, which should therefore in turn accelerate the development of dissolution driven convection. This hypothesis is tested using an experimental analogue system where both the solute and reactant are soluble in the aqueous phase and the product of a rapid chemical reaction increases the fluid density and remains in solution.

4 EXPERIMENTAL SYSTEM

There are significant practical, financial and safety constraints that must be considered when trying to replicate real reservoir conditions in the laboratory. To overcome these, it is necessary to develop an analogue system that, after nondimensionalisation, is dynamically similar to the real CO_2 problem and satisfies the same initial and boundary conditions in a standard laboratory environment.

The experimental apparatus and physicochemical system used to mimic the dissolution of CO_2 are described in sections §4.1 and §4.2 of this chapter. Details of the experimental method are outlined in section §4.3 and finally the image processing procedures are presented in section §4.4.

4.1 EXPERIMENTAL APPARATUS

4.1.1 The Hele-Shaw cell

Two-dimensional flow in a porous medium is often modelled experimentally using a Hele-Shaw cell. A Hele-Shaw cell consists of two parallel plates separated by a fixed thin gap as shown in Figure 4.1. The plates are transparent, making it possible to observe the behaviour of the fluid inside the cell, which has an effective porosity $\phi = 1$ (Oltean et al., 2008). In order to model buoyancy-driven flows, the cell is orientated vertically with gravity acting in the downward z-direction.

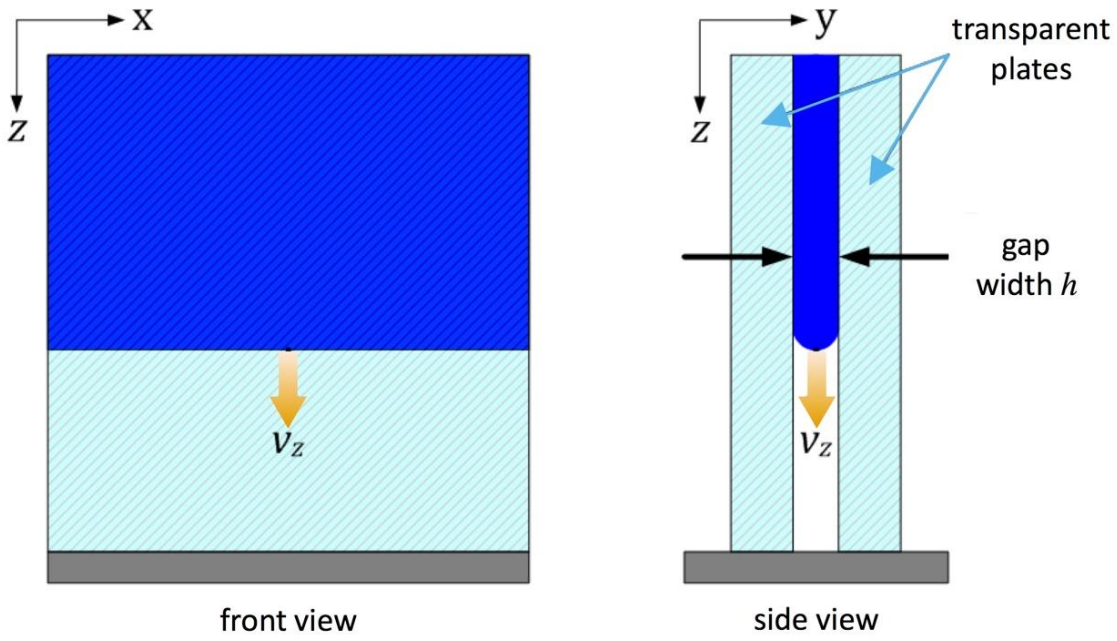

Figure 4.1 Sketch showing flow in a Hele-Shaw cell viewed from the front and the side.

When considering the velocity of the fluid, averaged across the cell gap width *h*, in the downward z-direction and horizontal x-direction, the Navier-Stokes equation can be used to give

$$v_z = -\frac{h^2}{12\mu}\left(\frac{\partial p}{\partial z} - \Delta\rho_0 \mathrm{g}\right) \tag{4.1}$$

$$v_x = -\frac{h^2}{12\mu}\left(\frac{\partial p}{\partial x}\right) \tag{4.2}$$

The equations above are consistent with Darcy's Law, where the permeability *k* is related to the gap between the cell plates *h* according to $k = h^2/12$ (Lamb, 1932), showing that the flow in the cell is analogous to that in a two-dimensional homogenous, isotropic porous medium.

The design of the Hele-Shaw cell and auxiliary apparatus used in experiments is described in the following section (§4.1.2).

4.1.2 Design and development of experimental apparatus

The design of the Hele-Shaw cell used in the laboratory experiments, adapted from Cardoso and Andres (2014) and Kuster et al. (2011), features two vertically aligned

cells that are filled separately and then brought together by slowly sliding the upper cell down towards the lower cell, as shown in Figure 4.2.

The two cells can be filled with different fluids which are immiscible with each other, similar to the supercritical CO_2 – brine system under investigation. As soon as the upper and lower cell fluids come into contact, diffusion, convection and reaction of the fluids begins. The use of this two cell set-up thus makes it possible to control the exact start time of the experiment and avoid shear effects associated with injecting one fluid on top of another.

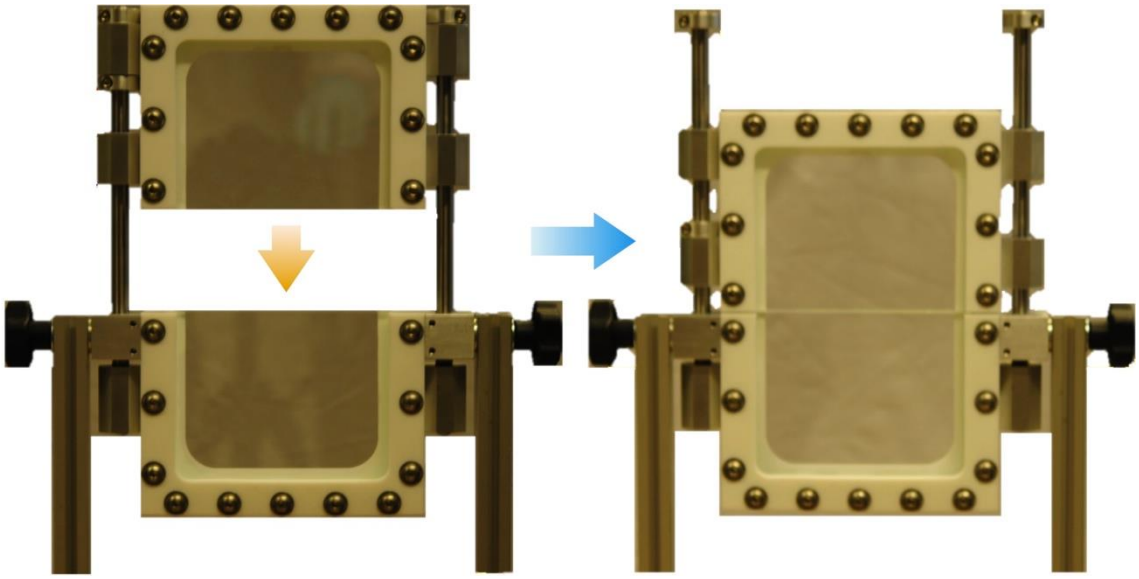

Figure 4.2 Two layer Hele-Shaw cell device used in laboratory experiments. The upper cell slides down to rest on top of the lower cell, allowing for the two immiscible fluid layers to come into contact.

Each cell consists of a U-shaped PTFE frame bolted around a pair of high quality transparent plates. The choice of plate material depends on its chemical resistance to the reactive solutions used. The dimensions of the plates were specified as 130 mm × 100 mm × 6.5 mm, which corresponds to a visible area of 120 mm × 95 mm. The plates within each cell were separated by a thin PTFE spacer in order to maintain a constant gap width and thus a constant permeability. A detailed schematic of the cell design is shown in Figure 4.3.

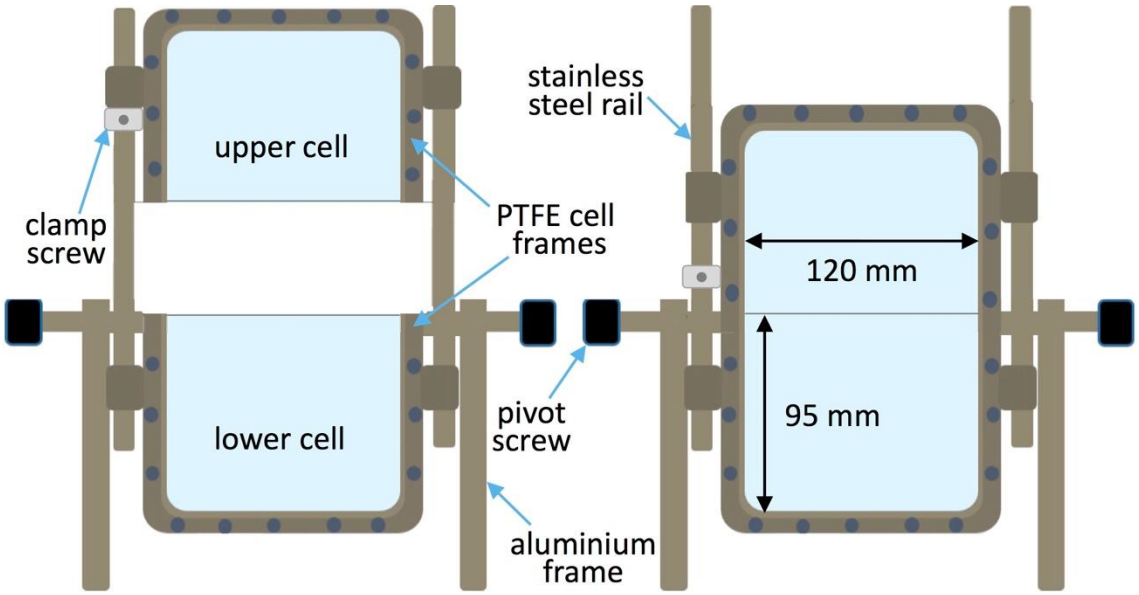

Figure 4.3 Design schematic of the Hele-Shaw cell device. The two cells are secured using PTFE frames which can freely pivot around an axis attached to the aluminium frame. The two cells can be kept apart using a clamp screw on the stainless steel rails.

The cells are attached to a set of stainless steel rails that freely pivot around the frame in line with the top of the lower cell (Figure 4.4). Given that the upper cell is free to slide up and down the rails, it is easy to configure a convenient orientation when assembling or taking apart the apparatus. A clamp screw is used on the steel rails to keep the cells apart during the filling stage. The base of the frame also features adjustable screws that are used in conjunction with a spirit level to ensure even alignment of the cells and the interface before the start of each experiment.

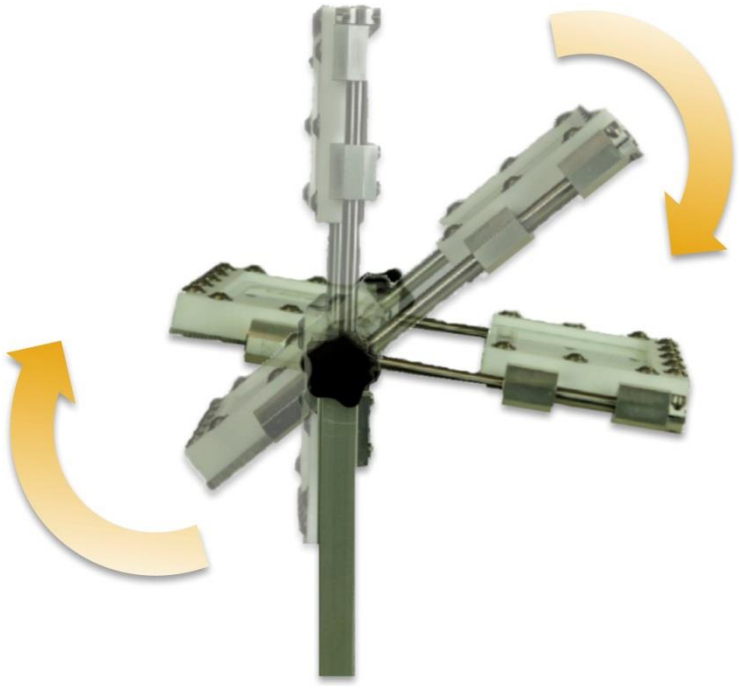

Figure 4.4 Side view showing that the cells can be freely tilted around the pivot axis.

4.2 ANALOGUE PHYSICOCHEMICAL SYSTEM

4.2.1 Selection criteria

The fluids used inside the Hele-Shaw cell require careful selection as the experimental system has to mimic the diffusion, convection and reaction of supercritical CO_2 during trapping, whilst also obeying the same boundary and initial conditions as the real CO_2 problem. A suitable analogue system has to satisfy the following selection criteria:

- *Do the fluids form two immiscible phases?* Supercritical CO_2 and brine are immiscible with each other.
- *Can a solute be transferred from one immiscible phase to the other?* CO_2 dissolves in the underlying brine to form an aqueous layer of CO_2 –rich brine.
- *Does the dissolution of solute cause a density difference large enough to drive convection in the lower fluid layer?* CO_2-rich brine is denser than the surrounding brine and the density difference causes buoyancy-driven convective instability.
- *Is the concentration of solute constant at the interface?* The concentration of CO_2 at the top of the domain is assumed to be constant and equal to the solubility of CO_2 in brine.

- *Can the solute undergo a reaction where the product remains in solution and has a greater density than the reactants?* In this study we are interested in modelling reaction of CO_2 in the aqueous phase that forms a dense soluble product.
- *Can the flow and reaction of solute be visualised in the laboratory?* It is necessary to track and measure the fluid flow with the help of a Schlieren technique, interferometry or a colour indicator under standard laboratory conditions.

4.2.2 MIBK – acetic acid – aqueous ammonia system

Using the previously defined selection criteria a candidate system was chosen. The immiscible phase boundary between the supercritical CO_2 and the underlying brine was modelled by injecting the organic solvent methyl-iso-butyl-ketone (MIBK) into the upper cell and an aqueous solution into the lower Hele-Shaw cell. MIBK is less dense than water (802 kg m^{-3}) and its very low aqueous solubility (2%) ensures that the two layers remain immiscible during the course of an experiment.

To mimic the dissolution of CO_2 into brine, acetic acid was dissolved in the upper organic MIBK layer. The MIBK – acetic acid – water system is common in industrial liquid-liquid extraction and mutual solubility data has been well documented by Sherwood et al. (1939). The concentration of acetic acid in the organic phase falls as you approach the interface in order to drive mass transfer. Local equilibrium between the two phases is assumed so that acetic acid dissolves instantaneously into the underlying aqueous layer. The example for modelling the conduction of heat in an infinite composite solid, given by Carslaw and Jaeger (1959), was applied to this scenario to find that the aqueous concentration of acetic acid $\underline{C_{As}}$ at the interface can be expressed as

$$C_{As} = \frac{H}{1 + H\sqrt{\frac{D_A}{D_{A,MIBK}}}} C_{A,MIBK} \tag{4.3}$$

where $C_{A,MIBK}$ is the initial bulk concentration of acetic acid uniformly dissolved in the MIBK organic layer, H is the equilibrium constant equal to 1.39 (Sherwood et al., 1939), D_A and $D_{A,MIBK}$ are the diffusion coefficients for acetic acid in water and for acetic acid in MIBK equal to 1.29×10^{-9} m^2 s^{-1} and 1.78×10^{-9} m^2 s^{-1} respectively

(Bulicka and Prochazka, 1976). Using the expression above, the concentration of acid at the top boundary of the lower aqueous layer is approximated to be constant and equal to

$$C_{As} = 0.64 C_{A,MIBK} \tag{4.4}$$

This expression has been calculated for the case where there is no convection and reaction occurring in the system. The presence of convection and reaction is likely to increase the rate of mass transfer and therefore influence the concentration of acid at the interface. However, this work assumes that because there is low resistance to mass transfer in the upper organic layer compared to that in the lower aqueous layer, these effects can be ignored and the aqueous concentration of acid at the top boundary is assumed to remain constant and equal to C_{As} as the experiment proceeds.

The diffusion of acetic acid across the interface and into the lower aqueous layer results in a density difference with the surrounding fluid, which drives hydrodynamic instabilities in the form of convective fingers as show in Figure 4.5.

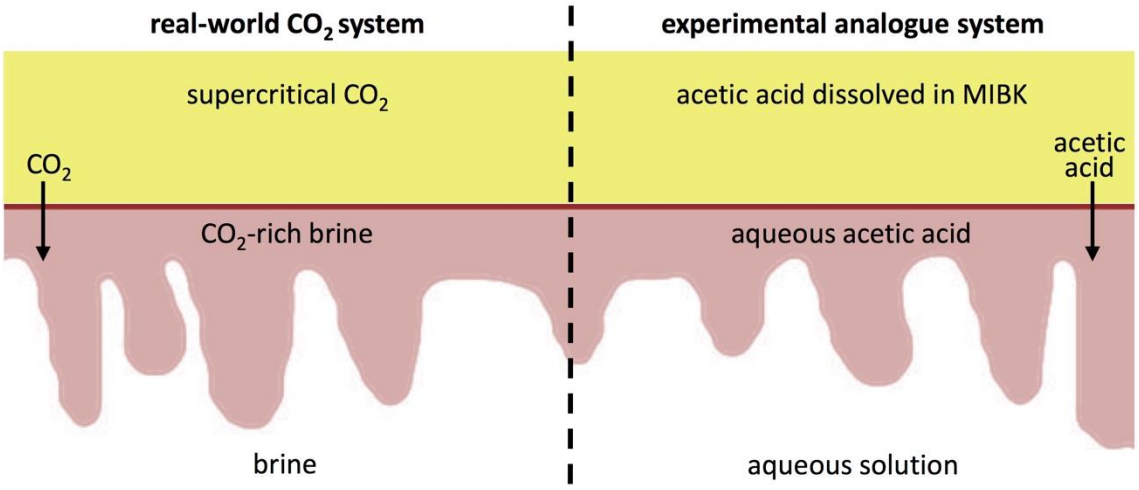

Figure 4.5 Summary of how dissolution of CO_2 in a saline aquifer is modelled in the laboratory using an experimental analogue physicochemical system.

At the start of the experiment, the lower aqueous layer is free of acetic acid and the dissolution of acid is assumed to have no significant effect on the volume of the lower layer solution. As all of the boundary and initial conditions are adequately satisfied, this experimental system makes it possible to study the inert solubility trapping mechanism of CO_2 storage.

The effect of reaction on the flow and transport of CO_2 was investigated experimentally by adding ammonia to the lower aqueous layer. The $A + B \rightarrow C$ neutralisation reaction between acetic acid (reactant *A*) and ammonia (reactant *B*) forms aqueous ammonium acetate (product *C*). The overall reaction can be summarised as

$$CH_3COOH_{(aq)} + NH_{3(aq)} \rightarrow NH_4CH_3COO_{(aq)} \tag{4.5}$$

The neutralisation involves direct proton transfer between the acid and the base, obeying second-order kinetics (Mohammed et al., 2007). The reaction rate is almost instantaneous with a kinetic constant k_r of 10^{11} M^{-1} s^{-1} at 20°C (Someya et al., 2009).

Acetic acid and ammonia are classed as a weak acid and base respectively, and dissociate in water according to the following equilibrium equations:

$$CH_3COOH \rightleftharpoons CH_3COO^- + H^+ \tag{4.6}$$

$$NH_3 + H_2O \rightleftharpoons NH_4^+ + OH^- \tag{4.7}$$

$$H_2O \rightleftharpoons H^+ + OH^- \tag{4.8}$$

The equilibrium constants for each reaction are:

$$K_a = \frac{[CH_3COO^-][H^+]}{[CH_3COOH]} = 1.75 \times 10^{-5} \tag{4.9}$$

$$K_b = \frac{[NH_4^+][OH^-]}{[NH_3]} = 1.75 \times 10^{-5} \tag{4.10}$$

$$K_w = [H^+][OH^-] = 1.01 \times 10^{-14} \tag{4.11}$$

The equilibrium constant for the overall reaction (4.5) can be expressed as

$$K = \frac{K_a K_b}{K_w} = 3.2 \times 10^4 \tag{4.12}$$

The large value of *K* means that the production of ammonium acetate is favoured and the reaction is driven practically to completion.

The solutal expansion coefficients for acetic acid, ammonia and ammonium acetate are 8.17, -7.09 and 14.54 kg m^{-3} M^{-1} respectively (Novotny and Sohnel, 1988; Sohnel et al., 1984; Wolf, 1966). Given that the solutal expansion coefficient for ammonium acetate is greater than that of acetic acid, the formation of product results in an increase in density of the convective fingers and has a destabilising effect on the system as desired.

The change in the density of solution due to the dissolution of solute is approximately 1% and therefore the condition for incompressibility is satisfied in the experiments. The fluid flows are sufficiently slow for Taylor dispersion in the cell to be negligible and the system is considered to be isothermal as heat effects are much weaker than those due to changes in concentration (Almarcha et al., 2013).

The governing equations introduced in the previous chapter to theoretically model this system have assumed that the diffusion coefficients of the species in solution are equal. In reality, the diffusion coefficients for acetic acid, ammonia and ammonium acetate are $1.3 \times 10^{-9}\ m^2\ s^{-1}$,$1.5 \times 10^{-9}\ m^2\ s^{-1}$ and $1.4 \times 10^{-9}\ m^2\ s^{-1}$ respectively (Weast et al. 1979). Given the low concentrations of species *B* and *C* relative to solute *A* (except for the stoichiometric case where $C_{Bo}' = 1$), the difference in magnitude between the diffusion coefficients has been assumed to be small enough to be ignored and a single diffusion coefficient is assumed for the minimal physical model used in this work. The effect of differential diffusion on the development of instability is a topic of ongoing work and is not considered here.

4.2.3 Choice of pH indicator

As the solutions are transparent colourless liquids, a pH colour indicator was used to help visualise the fluid flow. The dissolution of acetic acid releases H^+ ions and thus lowers the pH of the aqueous solution. These pH changes can be detected with an indicator which has different colour properties depending on whether it is in its acid *HInd* or conjugate base Ind^- form

$$HInd \rightleftharpoons H^+ + Ind^- \tag{4.13}$$

Almarcha et al. (2010) and Kuster et al. (2011) note that because indicators themselves act as weak acids or bases, they can interfere with the observed fluid patterns. In order to ensure that the indicator has no substantial impact on the development of the convective dynamics, the type of colour indicator was carefully selected to capture the full extent of the fingers and accurately characterise the flow as advised in Thomas et al. (2015).

A number of different indicators were tested to determine which would best visualise the motion and behaviour of the system. An identical experimental case was performed using different indicators each with a concentration of 10^{-6} M. The development of density-driven instability in the lower aqueous layer for the cases with universal

indicator, methyl red and also an equal volume mixture of methyl red and thymol blue is shown in Figure 4.6.

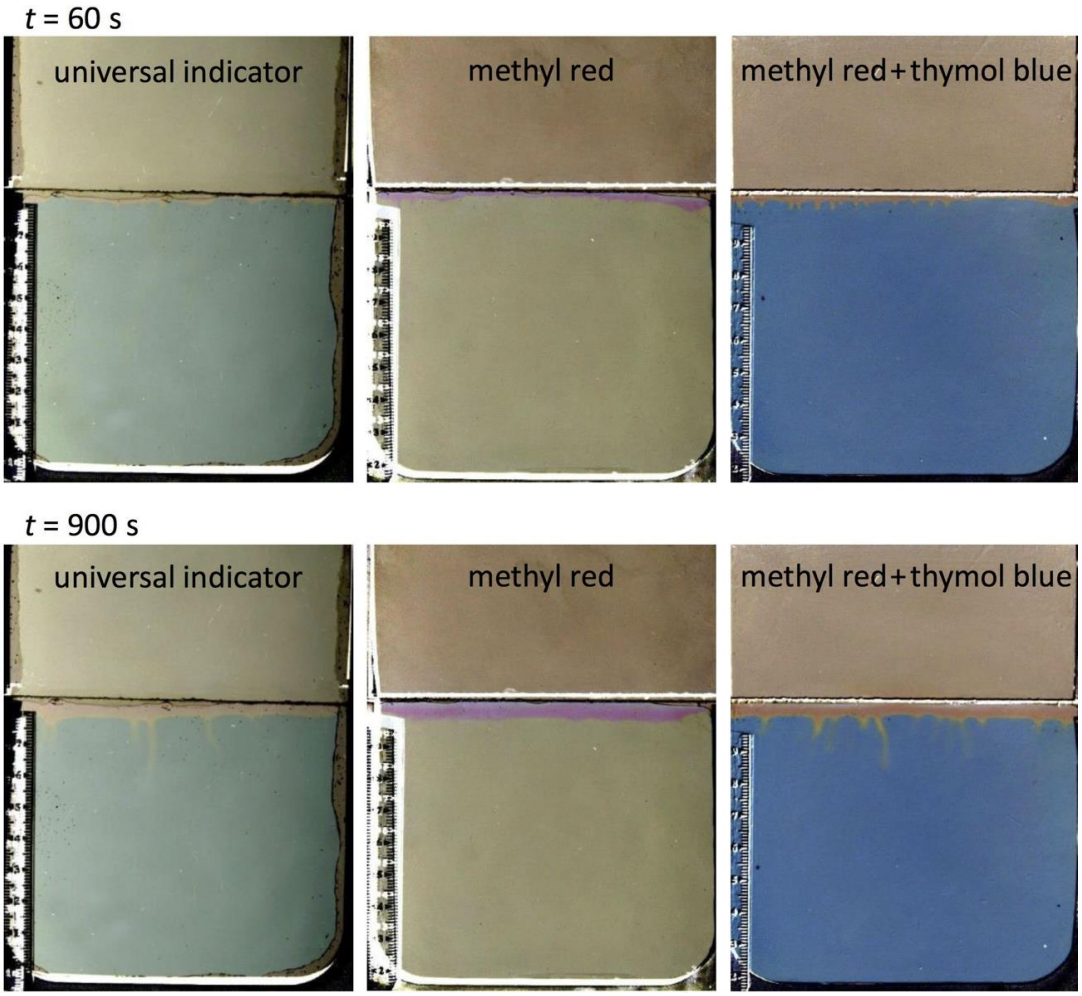

Figure 4.6 Development of instability in identical experimental runs (C_{As} = 0.113 M, C_{Bo} = 10^{-3} M, h = 0.8 mm) using different indicators with concentration of 10^{-6} M: universal indicator, methyl red and a mixture of methyl red and thymol blue**.**

All three indicators show an acidic boundary layer that grows to a similar thickness in the lower aqueous layer. However, the fingers that are visible after 900 seconds with universal indicator and the methyl red/thymol blue mixture cannot be observed when only methyl red is used. Methyl red has a transition range between pH 4.2 and 6.2, over which the colour changes from red to yellow. This suggests that the fingers after 900 seconds have a pH greater than 6.2 as they cannot be distinguished from the surrounding bulk alkaline solution when using only methyl red. Thymol blue is a diprotic acid and changes from red to yellow in the pH range of 1.2 to 2.8 and then from yellow to blue in the pH range 8.0 and 9.8. Universal indicator and the methyl red/thymol blue mixture both show a very similar convective pattern suggesting that the

full extent of the flow has been captured. However, the fingers are not as clear and sharp with universal indicator due to the poor contrast in colour compared to when the methyl red/thymol blue mixture is used. This suggests that the mixture of methyl red/thymol blue indicators is best suited for the acetic acid – ammonia reaction system.

The pK_a values for acetic acid and ammonia are 4.75 and 9.25 respectively. Therefore an acetic acid solution with pH lower than 4.75 will have undissociated acetic acid as the dominant species as shown in Figure 4.7(a), and an ammonia solution with pH greater than 9.25 will have undissocaited ammonia as the dominant species as seen in Figure 4.7(b). For the intermediate regions where pH is > 4.75 for the acetic acid solution and pH is < 9.25 for aqueous ammonia, the respective solutions will be mostly made up of the conjugate ions as shown in Figure 4.7.

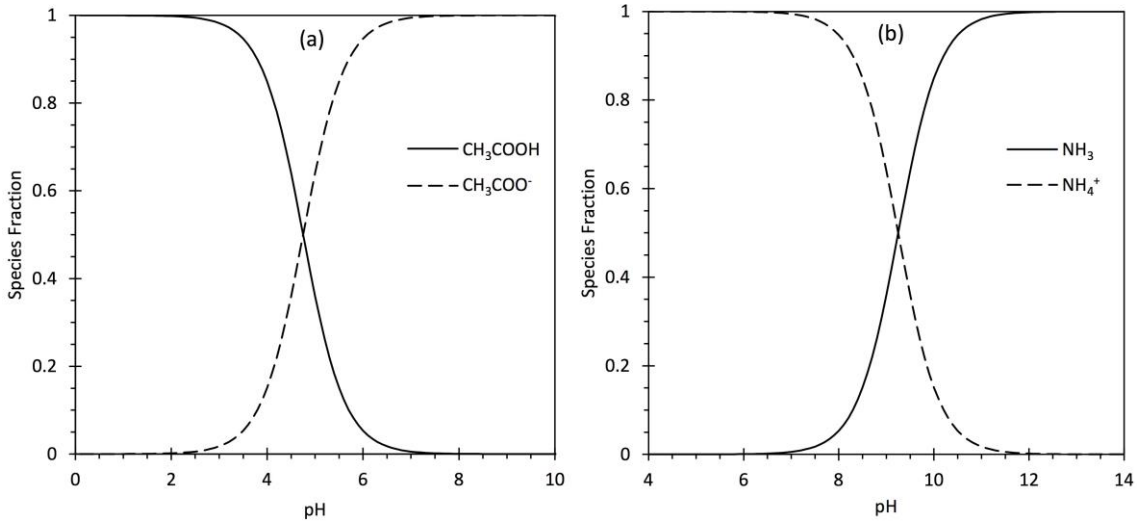

Figure 4.7 (a) Concentration fractions of undissociated acetic acid CH_3COOH and dissociated acetate ions CH_3COO^- calculated for an acetic acid solution using equation (4.9) at a given pH. (b) Concentration fractions of undissociated aqueous ammonia NH_3 and dissociated ammonium ions NH_4^+ calculated for an ammonia solution using equation (4.10) at a given pH.

The mixture of methyl red and thymol blue indicators can help visualise the three distinctive regions shown in Figure 4.7 where the acidic, neutral and alkaline species are dominant. Regions with high acetic acid concentration show up as red, unreacted ammonia solution is blue and the product of reaction can be identified by the yellow regions of the convective fingers in Figure 4.6. No indication of flow is observed in the upper organic layer in Figure 4.6 and both ammonia and ammonium acetate are insoluble in MIBK. Therefore the focus is on the dynamics only in the lower layer ($z \geq 0$).

4.3 EXPERIMENTAL PROCEDURE

An overview of the Hele-Shaw cell used in the experiments has been provided in §4.1. In this section, a description of the set-up is given along with details of the experimental procedure. A summary of the experimental parameters is given in section §4.3.7 with the common problems experienced during experimental runs and how to avoid them discussed in section §4.3.8.

4.3.1 Experimental apparatus assembly

The Hele-Shaw cell described in section §4.1.2 was assembled in the fume cupboard, with borosilicate glass plates used for the upper and lower cells. Borosilicate glass was chosen as the plate material because of its chemical resistance to the fluids in the MIBK – acetic acid – aqueous ammonia physicochemical system.

The cell gap width was set by inserting a U-shaped PTFE spacer of known thickness in between each set of plates, leaving the interface end of each cell open to be filled with fluid. A thin layer of silicone grease was applied to the spacers to seal them in place.

Transparent measuring tape with millimetre interval markings was attached to the cells in order to provide a measurement scale during image analysis.

4.3.2 Preparation of solutions

Glacial acetic acid was dissolved in MIBK to make up the upper organic layer solution to the required concentration between 0.02 – 1.76 M. This concentration range was chosen as it provides a practical timescale for the duration of an experimental run and a large enough density difference to drive convection. The lower cell solutions were prepared by dissolving different volumes of 35 wt% aqueous ammonia in deionised water, with electrical resistivity ~ 18.2 MΩ cm. The amount of ammonia dissolved was chosen to correspond to a dimensionless initial ammonia concentration C_{Bo}' (C_{Bo} / C_{As}) in the range from 0 to 1.

An equal volume mixture of methyl red (0.25 ml) and thymol blue (0.25 ml) indicators was added to the solutions and mixed well. The concentration of indicator in solution (10^{-6} M) was approximately one hundred times smaller than the lowest initial concentration of ammonia in the lower cell; large enough to yield a sufficient colour contrast between the acidic and basic forms, whilst also being low enough to ensure the effect of indicator on the dynamics of the system to be negligible.

4.3.3 Filling the cell

The aqueous solution was carefully injected into the lower cell through the gap between the glass plates as shown in Figure 4.8. Air bubbles were found to interfere with the fluid flow inside the cell so if any bubbles were observed during the filling stage, the cell would be emptied and the procedure would be repeated until the cell was evenly filled to its brim with the solution.

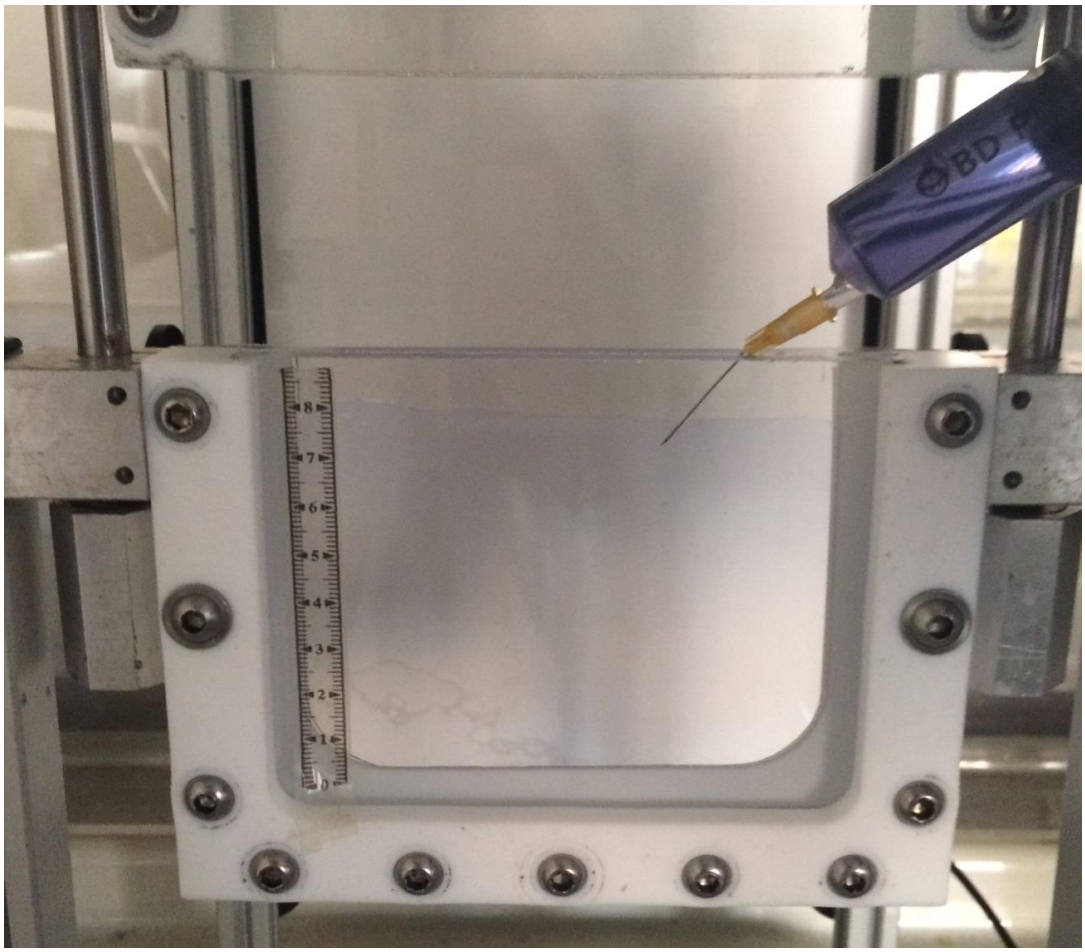

Figure 4.8 Injection of aqueous solution into the lower cell.

The cell was then rotated to access and fill the upper cell with the organic solution (Figure 4.9). A clean syringe and needle was used each time to avoid cross-contamination of reactants. After injection, the organic solution did not flow out of the upper cell due to surface tension effects (Zalts et al., 2008).

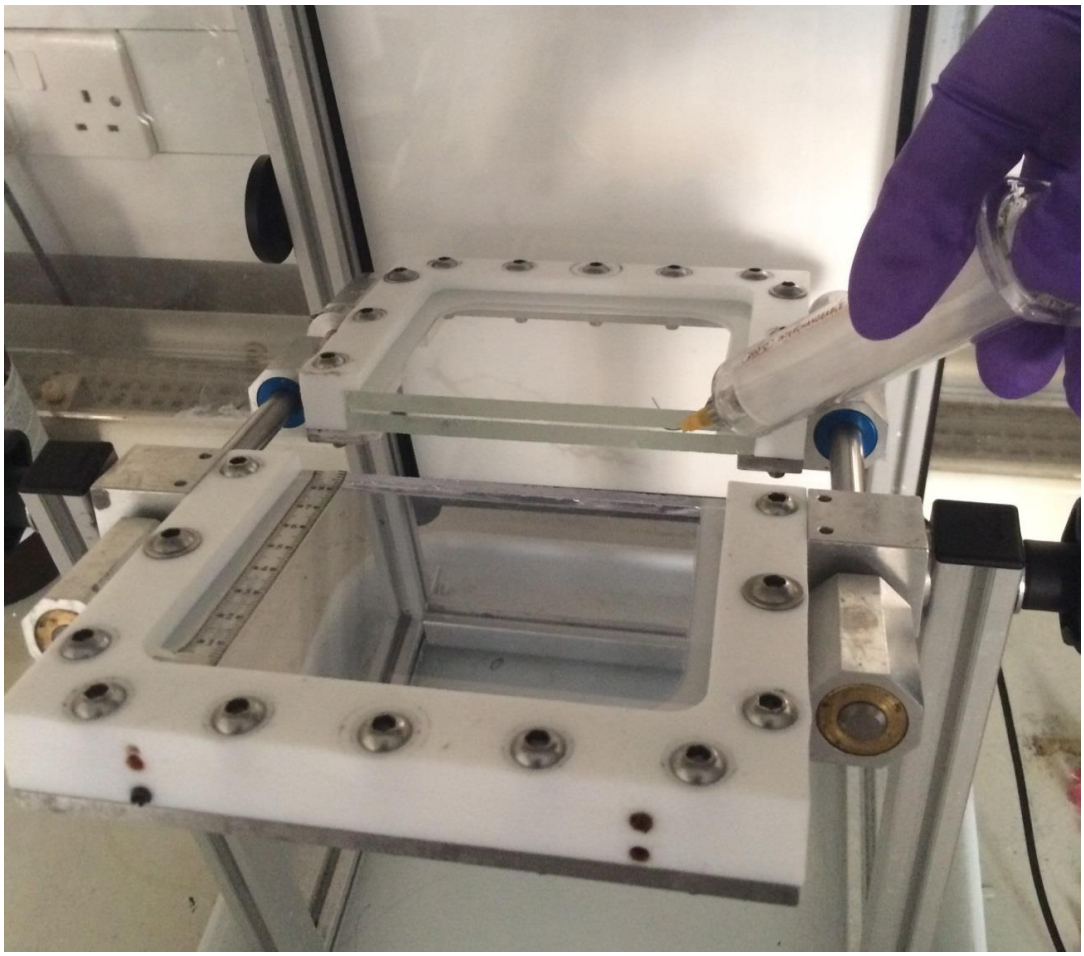

Figure 4.9 Injection of organic solution into the upper cell.

To start each run, a spirit level was used to check that the cells were aligned vertically and the upper cell was then slowly lowered to make contact with the lower cell, taking care to cause as little disturbance of the fluid interface as possible.

4.3.4 Image capture

A Nikon D300s digital camera (2,144 × 1,424 pixels) was mounted on a tripod facing the centre of the cell in order to record the progress of each experiment at regular time intervals (Figure 4.10). Images were taken with the camera's shutter speed set to 1/250 s, an ISO setting of 200 and an aperture of f/3.

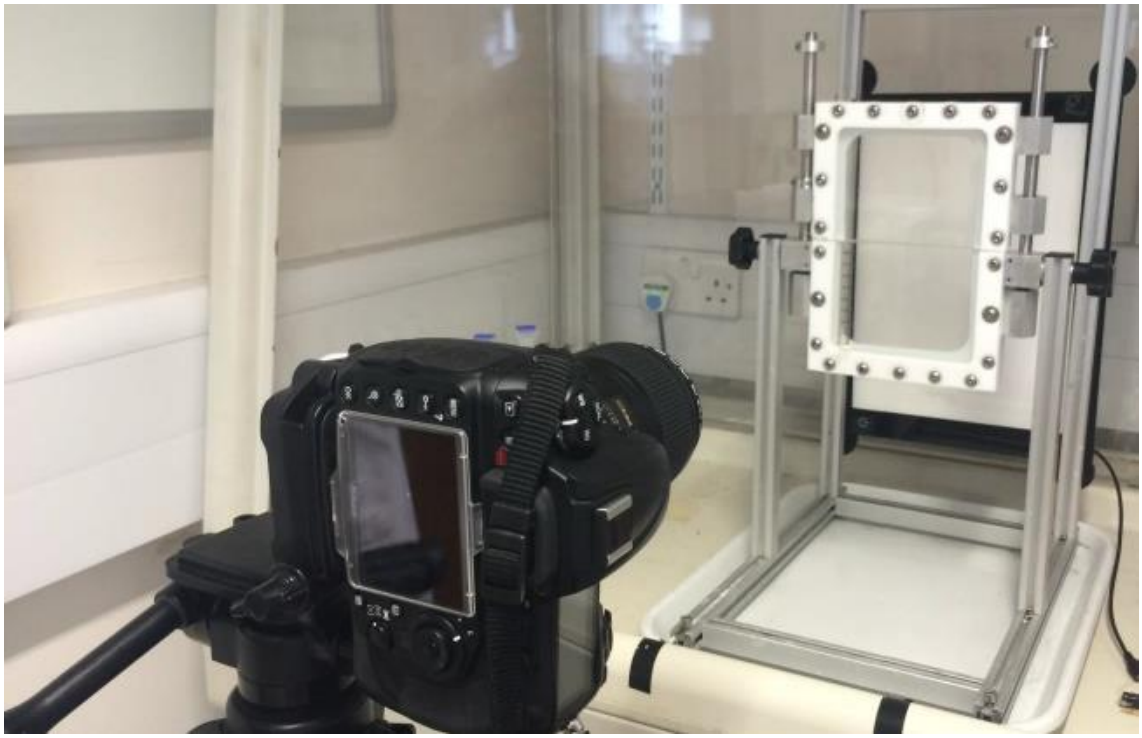

Figure 4.10 Laboratory set-up with a Nikon D300s camera used to record progress of the experiments performed in a fume cupboard.

The cell domain was lit from behind using an LED backlighting panel (Figure 4.11), with illuminated area of 210 x 297 mm, colour temperature of 9,000 K and light intensity of 1,600 lux. The light was found to remain cool for approximately 8 hours, which is several hours longer than the duration of the slowest experimental run and meant that heat effects from the light source could be deemed insignificant.

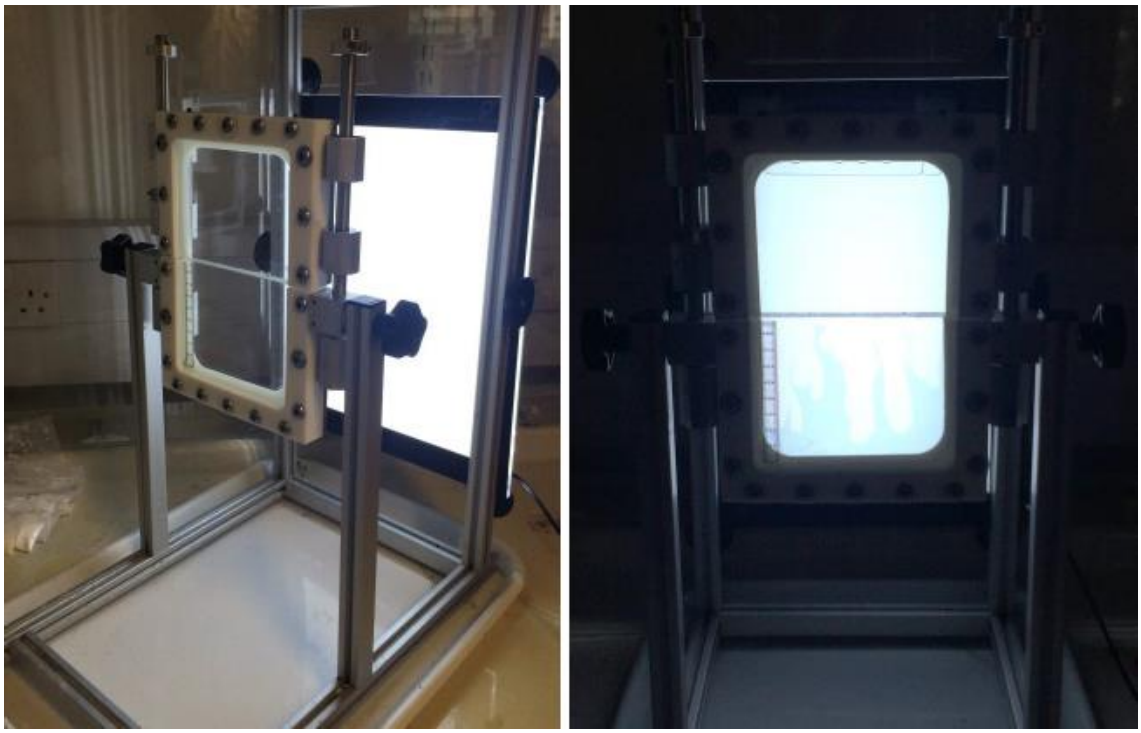

Figure 4.11 The apparatus is illuminated using an LED backlighting panel in order to visualise the flow inside the cells.

4.3.5 Cleaning of apparatus

At the end of each experiment, the cells were emptied and the rig was disassembled. With the apparatus still inside the fume cupboard, acetone was used to wash the glass plates and any other exposed parts of the cells. The plates were then rinsed with water and left to soak for 12 – 24 hours in a 5% dilute solution of Decon 90 cleaning agent, before being given a final wash in deionised water and left to dry.

4.3.6 Safety considerations

MIBK is highly flammable, whilst stock solutions of glacial acetic acid and 35 wt% ammonia are corrosive, so care was taken when diluting them down for use in experiments. The routes of exposure for the chemicals are through inhalation, ingestion and contact with the skin and or the eyes. To minimise risk, the experiments were performed in a fume cupboard, appropriate personal protective equipment was worn and the waste solutions were disposed of in accordance with the laboratory's safety regulations and guidelines.

4.3.7 Experimental system parameters

The physical and chemical parameters of the MIBK – acetic acid – aqueous ammonia system are summarised in Table 4.1. These parameters were kept constant for each experimental run. Cases with Rayleigh numbers $4.8 \times 10^3 – 3.4 \times 10^5$ and Da/Ra^2 in the range $2.9 \times 10^6 – 7.1 \times 10^7$ were performed by changing the gap width h between the cell plates (and thus the permeability k) and also the initial concentration of acetic acid in the organic phase (which in turn changes the aqueous solubility C_{As}). The cell gap width h was set using 0.5, 0.8 and 1.0 mm spacers equating to a permeability k of 2.08×10^{-8}, 5.33×10^{-8} and 8.33×10^{-8} m^2 respectively. The concentration of acetic acid dissolved in the MIBK organic layer was varied from 0.02 M to 1.76 M. These parameters along with those in Table 4.1 were used to nondimensionalise the experimental results so they could be compared to the real aquifer scenario. The amount of ammonia dissolved in the lower layer was chosen to correspond to a dimensionless initial ammonia concentration C_{Bo}' (C_{Bo} / C_{As}) in the range from 0 to 1. For the inert cases, $C_{Bo}' = 0$ and $Da/Ra^2 = 0$ as there is no reaction.

The dimensionless solutal expansion coefficients β_i' (β_i / β_A) for acetic acid, ammonia and ammonium acetate are 1.0, -0.9 and 1.8 respectively. These are constant and do not change as the same chemical species are involved in each experiment when using this physicochemical system.

The thermal Rayleigh number was also calculated using the equation below

$$\mathrm{Ra}_T = \frac{k\rho_0\beta_T\Delta T g L_z}{\mu D_T} \tag{4.14}$$

where D_T is the thermal diffusivity of water (1.49×10^{-7} m^2 s^{-1}), β_T is the thermal expansion coefficient (2.07×10^{-4} K^{-1}) and ΔT is the temperature change in the aqueous solution. The temperature change can be calculated using the enthalpy of reaction (Q = $– 5.04 \times 10^4$ J mol^{-1}) and specific heat capacity of water ($c_p = 4.18 \times 10^3$ J kg^{-1} K^{-1}) as $\Delta T = \left| Q \right| C_{As}/(\rho_o c_p)$. For a case with concentration C_{As} = 0.1 M and cell gap width h = 1.0 mm, the thermal Rayleigh number, $Ra_T = 87.5$, is almost 350 times smaller than the solutal Rayleigh number, $Ra = 3.05 \times 10^4$, which shows that the dynamics are mainly controlled by solutal effects and thermal effects can be ignored. In order to account for any wall or bottom boundary effects, an area 30 mm in from the bottom and 10 mm in from the sides of the cell plates was taken to represent the domain of the system. The vertical extent L_z was thus taken as 65 mm when calculating the Rayleigh number.

Table 4.1 Parameters of the experimental analogue system held constant for each run.

Parameter	Magnitude	Source
Viscosity μ [Pa s]	1.02×10^{-3}	(Weast et al., 1979)
Diffusivity D [m^2 s^{-1}]	1.29×10^{-9}	(Weast et al., 1979)
Porosity ϕ [-]	1	(Oltean et al., 2008)
Reaction rate constant k_r [M^{-1} s^{-1}]	10^{11}	(Someya et al., 2009)
Acetic acid solutal expansion coefficient β_A [kg m^{-3} M^{-1}]	8.17	(Novotny and Sohnel, 1988)
Ammonia solutal expansion coefficient β_B [kg m^{-3} M^{-1}]	-7.09	(Sohnel et al., 1984)
Ammonium acetate solutal expansion coefficient β_C [kg m^{-3} M^{-1}]	14.54	(Wolf, 1966)

4.3.8 Common experimental problems

Many runs had to be abandoned due to a number of experimental mishaps. The cells would often leak if the screws securing the PTFE frame around the glass plates were not tightened enough. An example of the solutions leaking from the upper and lower cells is shown in Figure 4.12.

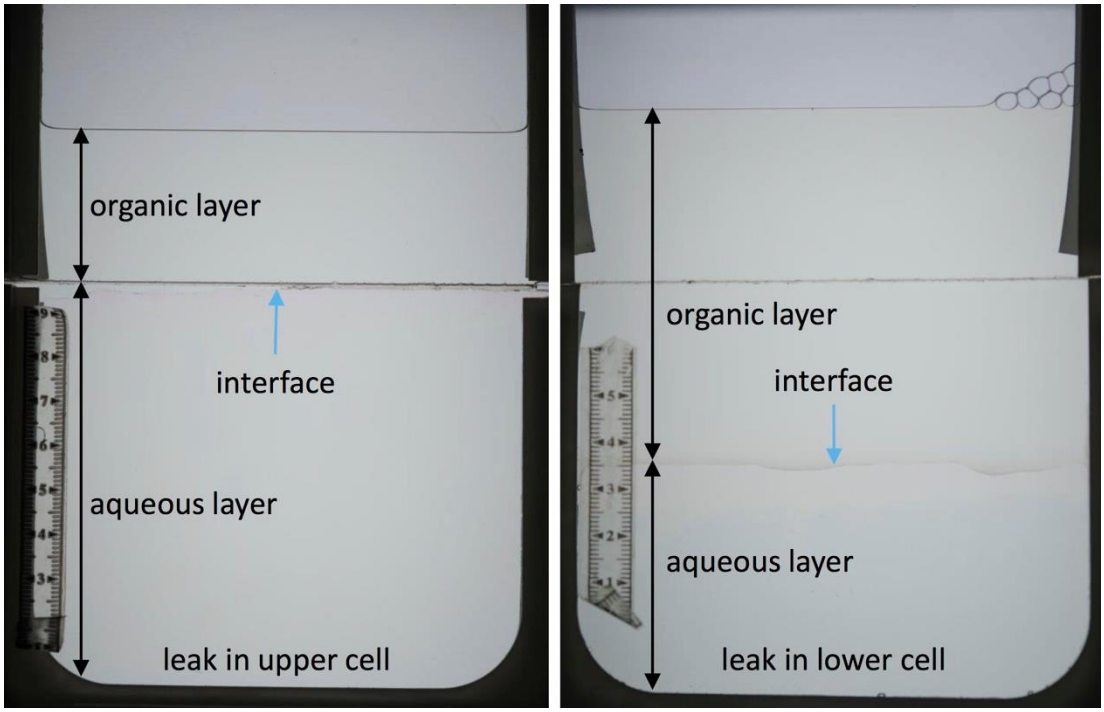

Figure 4.12 Examples of failed runs due to upper and lower cell leaks.

Another common cause for the leaks in the upper cell was due to air bubbles entering and driving the solution out of the cell. This would occur if the PTFE spacer was not placed close enough to the top/bottom edge of the glass plates leaving a gap for bubbles to enter from the side of the cell as shown in Figure 4.13.

In some cases, the upper and lower cells were not aligned with enough accuracy, meaning that the two liquid interfaces could not come into contact with each other and there would be no transfer of solute across the interface into the lower aqueous layer.

Figure 4.13 Air bubbles entering upper cell through gaps (circled) between the glass plates when the PTFE spacers are not properly positioned.

Other factors to consider include taking care when applying silicone grease to the PTFE spacer as too much grease could affect the gap thickness and thus the permeability of the cell. Also the high volatility of ammonia means that the concentration of the ammonia stock solution had to be periodically checked by titration with an acid of a known concentration.

4.4 IMAGE PROCESSING

After the completion of each experimental run, the captured images were processed and enhanced so that the convective patterns could be observed and then analysed quantitatively. Although great care was used to control the conditions affecting the image quality, it was necessary to make correction in order to reduce unwanted variations in the images. The post-processing steps required to yield final enhanced images are described in detail below.

4.4.1 Background correction

The recorded images suffered from uneven lighting, with the centre of the cell appearing brighter than the edges. This is shown in Figure 4.14 where the longitudinal-averaged intensity value of pixels is parabolic with its maximum in the middle of the cell domain.

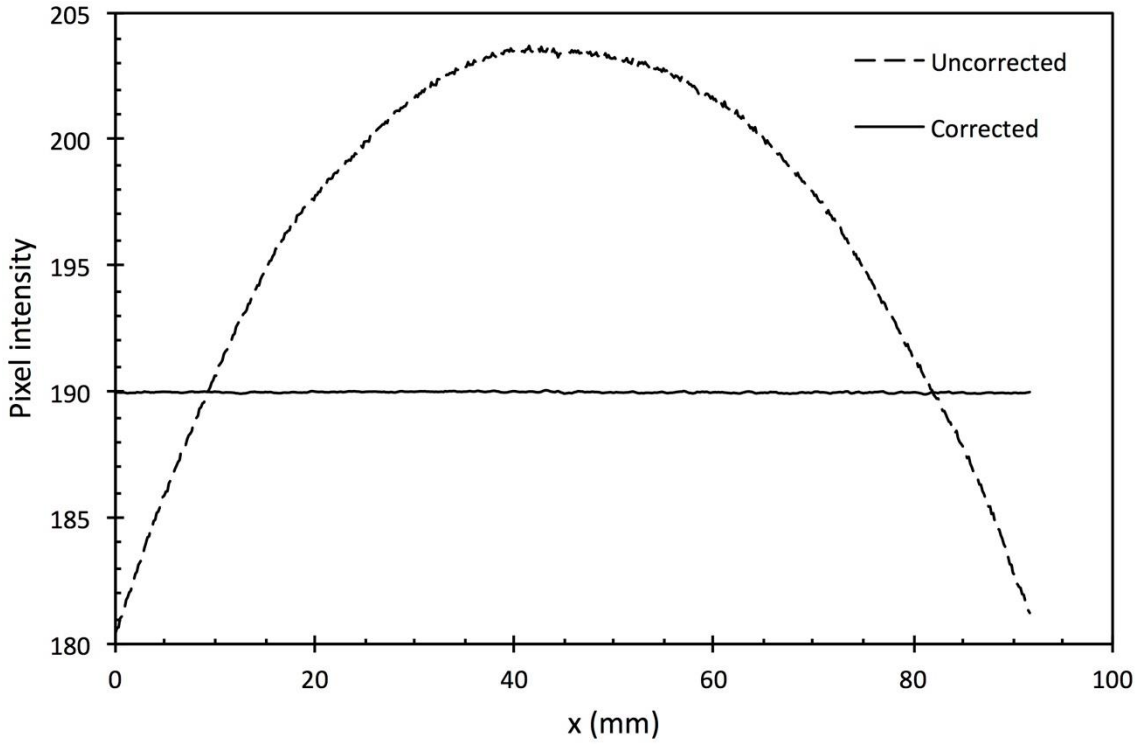

Figure 4.14 Longitudinal-averaged pixel intensity along a vertical transect of the lower cell domain before and after background correction.

In order to account for the spatial variation in lighting, background correction was performed using ImageJ software. Image sequences from each experimental run were imported into ImageJ along with a separate image file of a clear empty cell. This empty cell image acts as a reference and captures the distribution and unevenness of the light illuminating the cell. Using ImageJ, each image in the experimental sequence was then normalised by dividing each image pixel ($Image_{original}$) by the corresponding pixel value of the reference image of a clear empty cell ($Image_{reference}$) and then multiplying by the average pixel intensity of the domain (190 for the case in Figure 4.14).

$$Image_{corrected} = \frac{Image_{original}}{Image_{reference}} \times average\ intensity \tag{4.15}$$

Any remaining noise was reduced by applying a median smoothing filter to each image. A 3 by 3 pixel square was taken around a given pixel and this pixel was then replaced with the median value of the 9 pixels in the square. This smoothing calculation was performed for every pixel in the domain and as shown in Figure 4.14, the background correction method used almost entirely eliminates the effect of uneven lighting on the pixel intensity, yielding a uniformly lit image required for analysis.

4.4.2 Image enhancement

After the background correction steps were performed, it was still difficult to distinguish the convective fingers from the surrounding bulk fluid solution. The images were then enhanced and processed using ImageJ.

The colour intensity of each pixel that makes up an image ranges from 0 to 255, where a value of 0 corresponds to a total absence of colour and 255 corresponds to a complete presence of that colour. The image brightness and contrast were adjusted to a minimum value of 170 and a maximum of 210 for all images in the experimental sequence. An original experimental photograph before any image manipulation has taken place is shown in Figure 4.15 (a) and the resulting image after background correction and image enhancement is shown in Figure 4.15(c). The enhancement of the pixel colours makes it possible to see the fluid convective patterns in the lower cell that could not be observed by the naked eye.

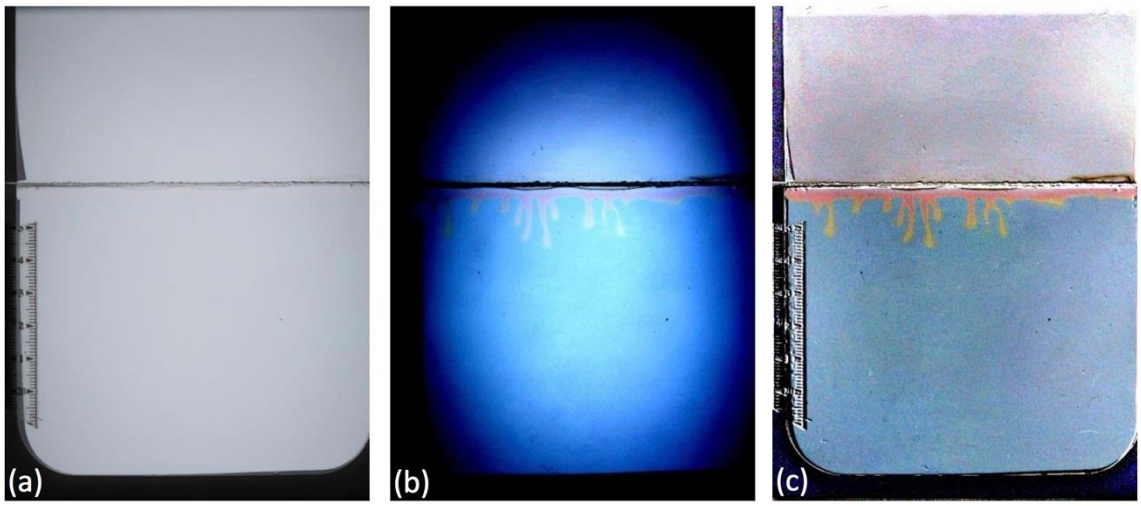

Figure 4.15 (a) Original image and effect of image processing steps: (b) without background correction and (c) with background correction.

The effect of background correction on the final enhanced image is apparent when comparing Figure 4.15(b) and (c). Both images had the same image enhancement techniques applied to them, but the lack of background correction in Figure 4.15(b) results in an image with a radially uneven brightness making it hard to accurately identify the characteristics of the fingers.

The final enhanced images are then further processed using MS Excel and Matlab to determine the lengths and wavelengths of the fingers. It is also possible to convert the colour intensity of each pixel to a corresponding pH required for the indicator to yield that particular colour. The pH measurements can then be used to calculate the concentrations of each species in solution and this method is outlined in the next chapter.

5 CALIBRATION AND VALIDATION OF EXPERIMENTAL SYSTEM

Having identified an analogue physicochemical system to model CO_2 in a saline aquifer, it was necessary to develop a method to quantitatively characterise the fluid flow. In section §5.1, we outline how it was possible to use the information from the images recorded during each run to determine the pH and concentration of the chemical species present in solution at a given time. To check the validity of this colorimetric method, the experimental results using the MIBK – acetic acid – water physicochemical system were compared to previous work for inert systems in section §5.2.

5.1 pH CALIBRATION

The flow in the physicochemical system was visualised using a pH indicator and the observed colour corresponds to the pH and thus the concentration of H^+ ions in the solution. The relationship between the colour and the pH was characterised by photographing aqueous solutions of know pH inside the lower cell. The resulting images were processed using ImageJ software to correlate the pH with the colour information of the image pixels. The RGB and HSV colour space models are discussed in sections §5.1.1 and §5.1.2 respectively, and after the pH of a solution has been identified from the images, the steps required to calculate the concentration of chemical species are given in §5.1.3.

5.1.1 RGB colour space

The colour information of an image is digitally stored in each pixel using the three primary colours: red, green and blue. The red, green and blue (RGB) components form a three-dimensional colour space to represent a particular colour as shown in Figure 5.1. If the three components are at their maximum value, white light is produced.

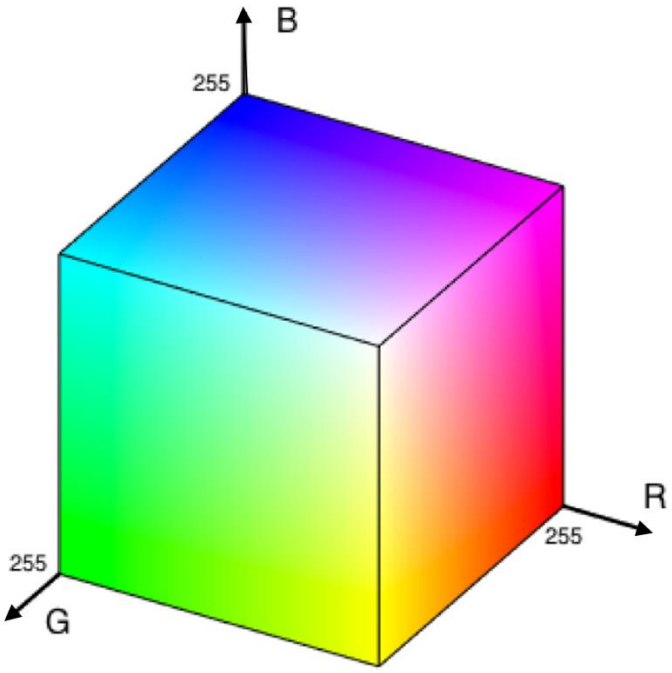

Figure 5.1 RGB colour space model.

Aqueous solutions of known pH were photographed to determine how the colour of the indicator changes with pH and the resulting images were processed using the method described in the previous chapter to produce images shown in Figure 5.2. It can be seen that the colour of the solution changes from red to yellow to blue as the pH is increased.

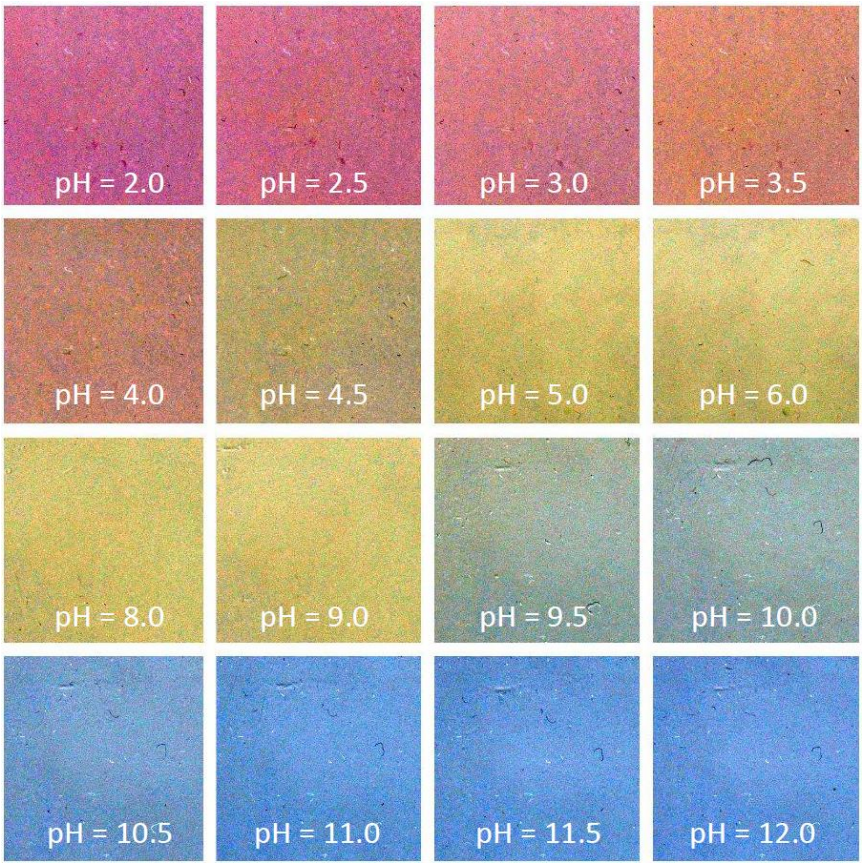

Figure 5.2 Processed images of aqueous solutions used for colorimetric pH calibration.

The average of the red, green and blue component pixel values of the reference solution images in the range $2 \leq pH \leq 12$ were plotted in Figure 5.3 with the error bars corresponding to the standard deviation in the image pixel values. In the high pH region, $9 \leq pH \leq 11$, the red and blue channels have been found to show a linear dependence on pH and the green channel also shows a linear relationship in the low pH range $2 \leq pH \leq 5$. However, the same green channel pixel value is assigned to a solution of pH 4 as to that of pH 10 making it impossible to directly map a RGB colour channel to the whole pH range.

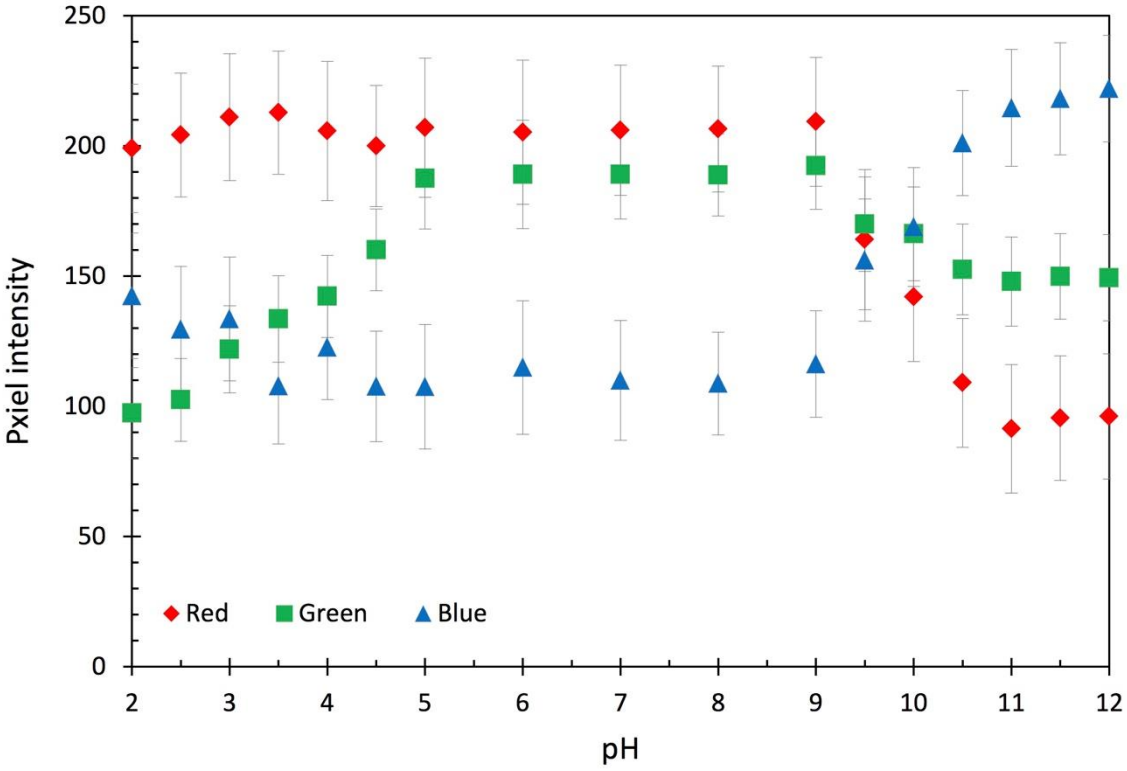

Figure 5.3 Plot showing the effect of pH on the average of the red, green and blue pixel values of reference solution images.

When the pH of the solution is increased from low to high, the indicator colour changes from red to yellow and then to blue – the order of these colours matches the visible light spectrum from long to short wavelengths. A limitation of the RGB colour space is that it is not directly related to the wavelengths of the light spectrum so a different colour space model was explored to quantitatively correlate colour to the pH.

5.1.2 HSV colour space

An alternative to the RGB model used to describe colour is the HSV colour space. The hue (H) channel is able to distinguish between the different colour wavelengths, whilst the saturation (S) and value (V) channels provide supplementary information on the colour details. This model is cone-shaped and rotating around the axis of the cone changes the hue which is the main descriptor of a particular colour independent of its intensity or greyness as shown in Figure 5.4.

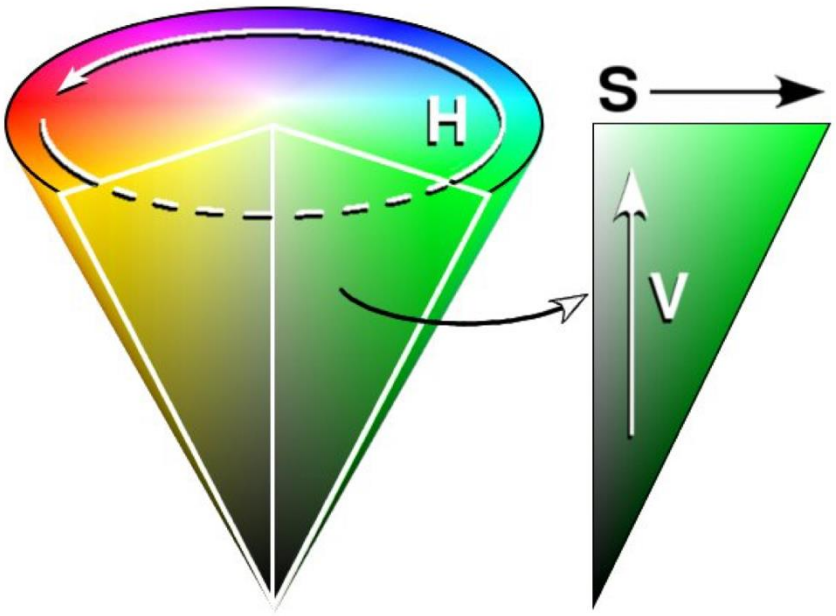

Figure 5.4 HSV colour space model.

It has also been reported by Florea et al. (2013) that the HSV colour model is less sensitive to changes in ambient light than the RGB colour space. Given that it was not possible to have complete control over the lighting conditions in the laboratory, this tolerance to ambient light variations is advantageous when trying to measure the pH from the images.

A digital camera records experimental images using the RGB colour space, so it was necessary to convert to HSV using the equations derived by Smith (1978) where R′ = R/255, G′ = G/255 and B′ = B/255 correspond to the normalised pixel values of the red, green and blue channels.

$$H = 255\left(\frac{G' - B'}{max_{channel}' - min_{channel}'} + 0\right)/6 \qquad \text{if } max = R^* \qquad (5.1)$$

$$H = 255\left(\frac{B' - R'}{max_{channel}' - min_{channel}'} + 2\right)/6 \qquad \text{if } max = G \qquad (5.2)$$

$$H = 255\left(\frac{R' - G'}{max_{channel}' - min_{channel}'} + 4\right)/6 \qquad \text{if } max = B \qquad (5.3)$$

*if H is negative add 255 to H

$$S = \frac{max_{channel} - min_{channel}}{max_{channel}} \tag{5.4}$$

$$V = max_{channel} \tag{5.5}$$

The hue channel pixel intensity values vary from 0 to 255, as illustrated using the colour wheel in Figure 5.5(a) and the hue values were measured and then averaged over the lower cell domain for the reference pH solutions. However, it was discovered that for solutions of low pH, their red colour was assigned pixel values either side of the zero/maximum on the hue colour wheel. This meant that for a solution with a pH of 3, the calculated average was in the blue region of the hue wheel instead of the red, as shown in Figure 5.5(b).

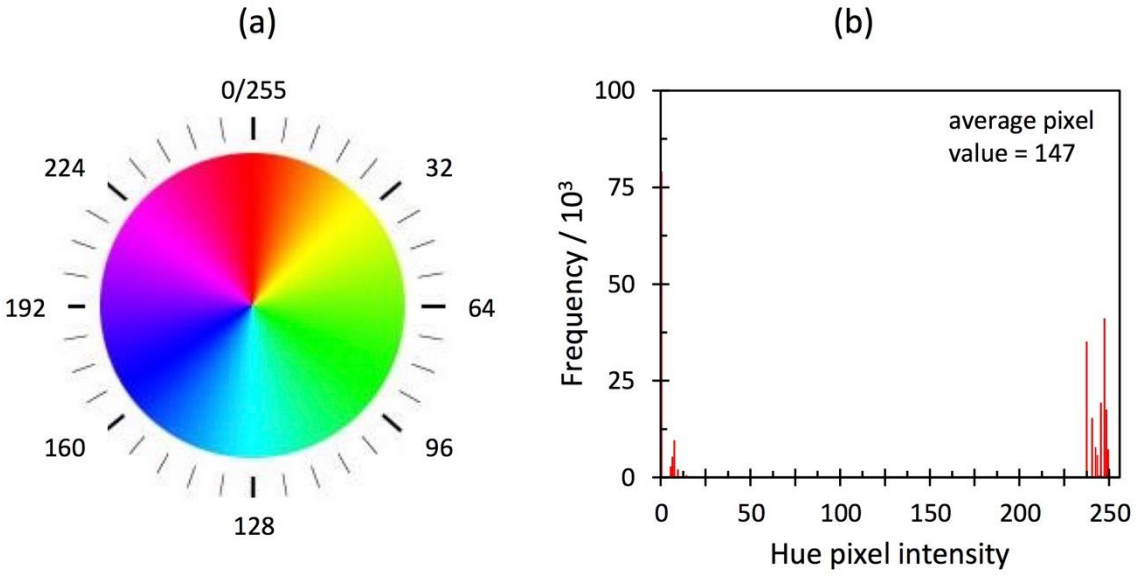

Figure 5.5 (a) Hue colour wheel showing range of pixel values from 0 to 255 and their corresponding hue. (b) Histogram showing frequency distribution of hue channel pixel values in a processed image of a reference solution with pH = 3.

To avoid this distortion of the average hue, the hue colour wheel was adjusted to start at what previously was 205 and the new hue channel values were plotted against pH in Figure 5.6.

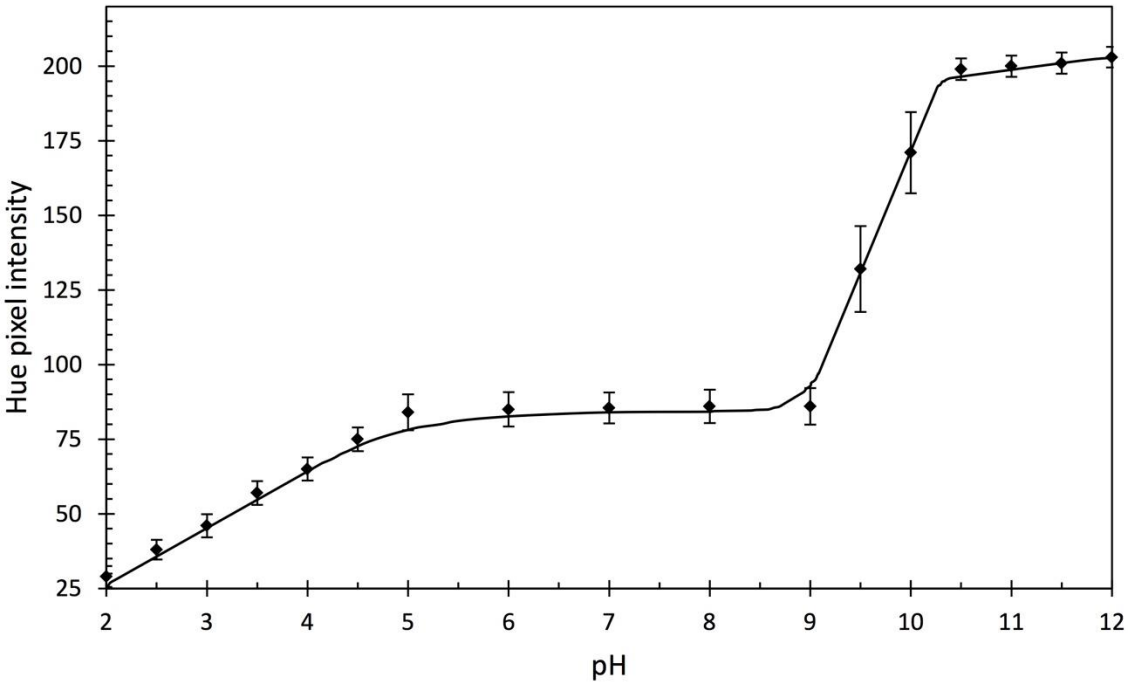

Figure 5.6 Plot of average hue channel pixel values as a function of pH.

As the pH of the solution was increased and the solution colour changed from red to yellow and then to blue, the measured average hue value was found to also increase as desired. A one-to-one linear relationship was observed between the hue channel pixel intensity and pH in the low and high pH ranges. In the near-neutral range, $5 < pH < 9$, the solution colour remains yellow and does not change enough to cause a measurable difference in the hue intensity. However, this limitation in the near-neutral region can be shown to be insignificant when using the measured pH to calculate the concentration of chemical species.

5.1.3 Calculation of species concentration from pH

Assuming that the dissolved acid and base species are in equilibrium, it is possible to calculate their concentration if the solution's pH is known. As mentioned in the previous chapter, acetic acid and ammonia are classed as a weak acid and base respectively, and partially dissociate in water. The dissociation of acetic acid produces H^+ ions and its conjugate base pair acetate (CH_3COO^-) ions, whilst the dissociation of ammonia releases hydroxide ions (OH^-) and its conjugate acid ammonium (NH_4^+) ions. The overall charge balance for the dissolved aqueous species is

$$[CH_3COO^-] + [OH^-] = [NH_4{}^+] + [H^+] \tag{5.6}$$

The concentration of all the dissociated and undissociated forms of acetic acid present in solution must equal the total concentration of acid added C_{AT}. It is assumed that ammonia is evenly distributed in the lower aqueous layer and the total concentration of ammonia species C_{BT} is equal to C_{Bo}, the initial concentration of ammonia in the lower cell, for each pixel in the domain. The concentration of the ammonium acetate product of reaction is equal to C_C.

$$C_{AT} = [CH_3COOH] + [CH_3COO^-] = C_A + C_C \tag{5.7}$$

$$C_{BT} = [NH_3] + [NH_4{}^+] = C_{B_0} \tag{5.8}$$

Substituting the acetic acid and ammonia equilibrium dissociation expressions K_a = ($[CH_3COO^-][H^+]$)/$[CH_3COOH]$ and K_b = ([NH4+][OH^-])/$[NH_3]$ into equations (5.7) and (5.8) respectively

$$[CH_3COO^-] = \frac{C_{AT}K_a}{[H^+] + K_a} \tag{5.9}$$

$$[NH_4{}^+] = \frac{C_{B_0}K_b[H^+]}{K_w + K_b[H^+]} \tag{5.10}$$

The expressions for $[CH_3COO^-]$ and $[NH_4{}^+]$ can be used to rewrite the charge balance equation (5.6) to give

$$\frac{C_{AT}K_a}{[H^+] + K_a} + \frac{K_w}{[H^+]} = \frac{C_{B_0}K_b[H^+]}{K_w + K_b[H^+]} + [H^+] \tag{5.11}$$

Rearranging to make C_{AT} the subject, the total concentration of acid transferred can be expressed as

$$C_{AT} = \left(1 + \frac{[H^+]}{K_a}\right)\left(\frac{C_{B_0}K_b[H^+]}{K_w + K_b[H^+]} + [H^+] - \frac{K_w}{[H^+]}\right) \tag{5.12}$$

Here, $[H^+]$ can be calculated from the pH and the rest of the terms are known constants, where a 1% change in K_a, K_b and K_w leads to a 1.8% uncertainty in C_{AT}. Given that the pH can be determined from the image pixel hue values, it is possible to estimate the concentration of the chemical species during each experimental run. For inert cases without reaction, there are no ammonia species present in solution so C_{Bo} is zero and $C_{AT} = C_A$. For the reactive cases, the concentration of ammonium acetate product can be expressed as the concentration of acid that has been neutralised by reaction:

$$C_C = [\mathrm{CH_3COO^-}] - [\mathrm{H^+}] = \frac{C_{AT}K_a}{[\mathrm{H^+}] + K_a} - [\mathrm{H^+}] \tag{5.13}$$

The concentration of unreacted acid C_A can then also be calculated by rearranging (5.7) and substituting for C_C

$$C_A = C_{AT} - C_C = C_{AT} - \frac{C_{AT}K_a}{[\mathrm{H^+}] + K_a} + [\mathrm{H^+}] \tag{5.14}$$

5.1.4 Calibration curves

The equations above were used to convert the pH of an aqueous solution to the total concentration of acetic acid C_{AT} present in solution for each of the experimental cases. The plots in Figure 5.7 show the conversion curves for the different reactive cases with different initial concentrations of ammonia C_{Bo} in the lower aqueous layer. These reactive cases are investigated and discussed in detail in the next chapter.

The limitation identified in Figure 5.6 where the solution colour remains yellow in the near-neutral pH range is proved not to be significant because the concentration of acid required to yield a solution with pH 5 – 9 is insensitive to the pH, as shown in Figure 5.7(a). Indeed, Figure 5.7(b) shows that a one-to-one relationship is obtained between the hue pixel intensity and the total acid concentration C_{AT} for the entire working range of pH in each of the reactive cases investigated.

Knowing C_{AT}, it is also possible to calculate the total mass of acid transferred to the lower layer domain and thus its mass flux. The transfer rate of solute has been previously modelled theoretically and experimentally to gain an understanding about the dissolution of CO_2 into brine. By comparing the mass flux and other characteristic measurements of convective flow with the results previously obtained by others, we can assess whether this experimental system is a suitable analogue for modelling the geo-storage of CO_2.

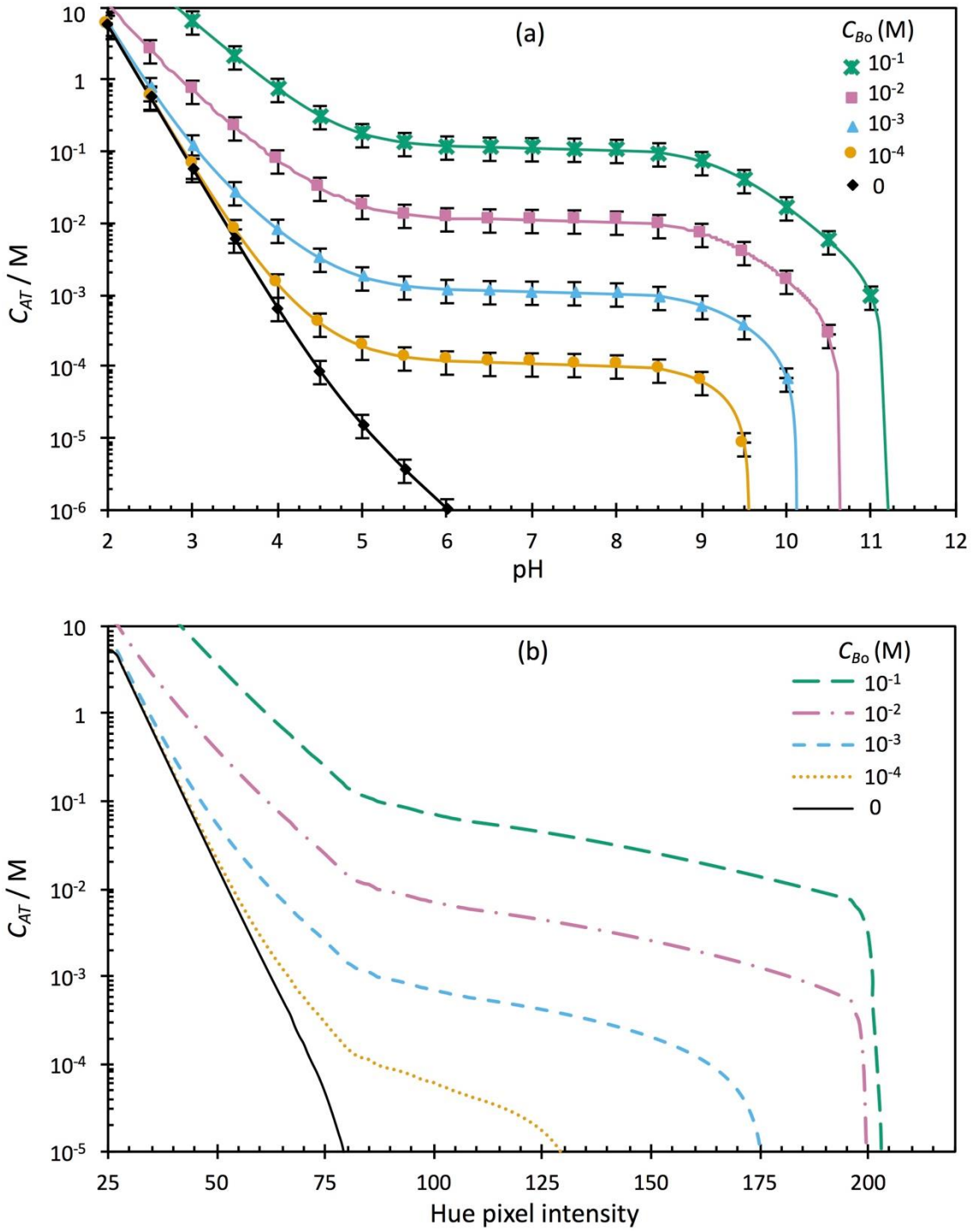

Figure 5.7 (a) Total concentration of acetic acid C_{AT} added to aqueous solutions of different initial concentrations of ammonia C_{Bo} as a function of pH. Error bars correspond to the propagation of pH measurement error in the calculation of C_{AT} using equation (5.12). (b) Relationship between C_{AT} and the hue channel pixel values for the different reactive cases plotted by combining Figure 5.6 and 5.7(a).

5.2 INERT SYSTEM VALIDATION

To test the MIBK – acetic acid – aqueous ammonia experimental system as a potential analogue to model the dissolution and flow of CO_2, the results had to be validated against previous work. The effect of chemical reaction on the fluid flow has not been well documented in literature, so inert case experiments without reaction were carried out for comparison purposes.

The lower layer of the experimental cell was filled with pure water (C_B', $C_C' = 0$) and combinations of different acetic acid concentrations and gap widths were used to investigate cases in the range $4.8 \times 10^3 \leq \mathrm{Ra} \leq 3.4 \times 10^5$ as described in the previous chapter. The observed patterns due to the dissolution of acetic acid are described in §5.2.1. For complete characterisation, qualitative descriptions are not enough so the development of the observed pattern was quantitatively analysed by measuring the depth to which the convective fingers sink in the domain (§5.2.2), the wavelength of the fingers (§5.2.3) and the time at which convective fingers were first observed (§5.2.4). The mass flux of solute into the lower aqueous layer was also measured (§5.2.5) and these results were then presented in dimensionless form, using the scaling relationships outlined in chapter 3, and compared to previous work.

5.2.1 Experimental observations

The transfer of acetic acid from the upper organic layer to the lower aqueous layer resulted in the formation of convective fingers in the lower layer. Figure 5.8 shows an image sequence depicting the evolution of convective fingers for the inert case with $\mathrm{Ra} = 3.4 \times 10^4$ ($C_{As} = 0.113$ M, $h = 1.0$ mm). The bulk aqueous fluid in the domain appears yellow corresponding to a near-neutral pH. This is expected given that the lower layer was initially filled with deionised water and 0.5 ml of the methyl red/thymol blue pH indicator mixture. The convective fingers were made up of acid and they show up as red with a pH of approximately equal to 3. The acidic fingers are denser than the surrounding fluid and sink independently in the domain with little lateral motion. As the fingers channel more solute away from the interface, they grow longer and wider, eventually becoming large enough to interact with one another. When the roots of neighbouring fingers get close enough together, they zip together and merge to become one finger. The observed fluid behaviour for this system mimics that of CO_2 in brine and the flow pattern is quantitatively analysed in the next section.

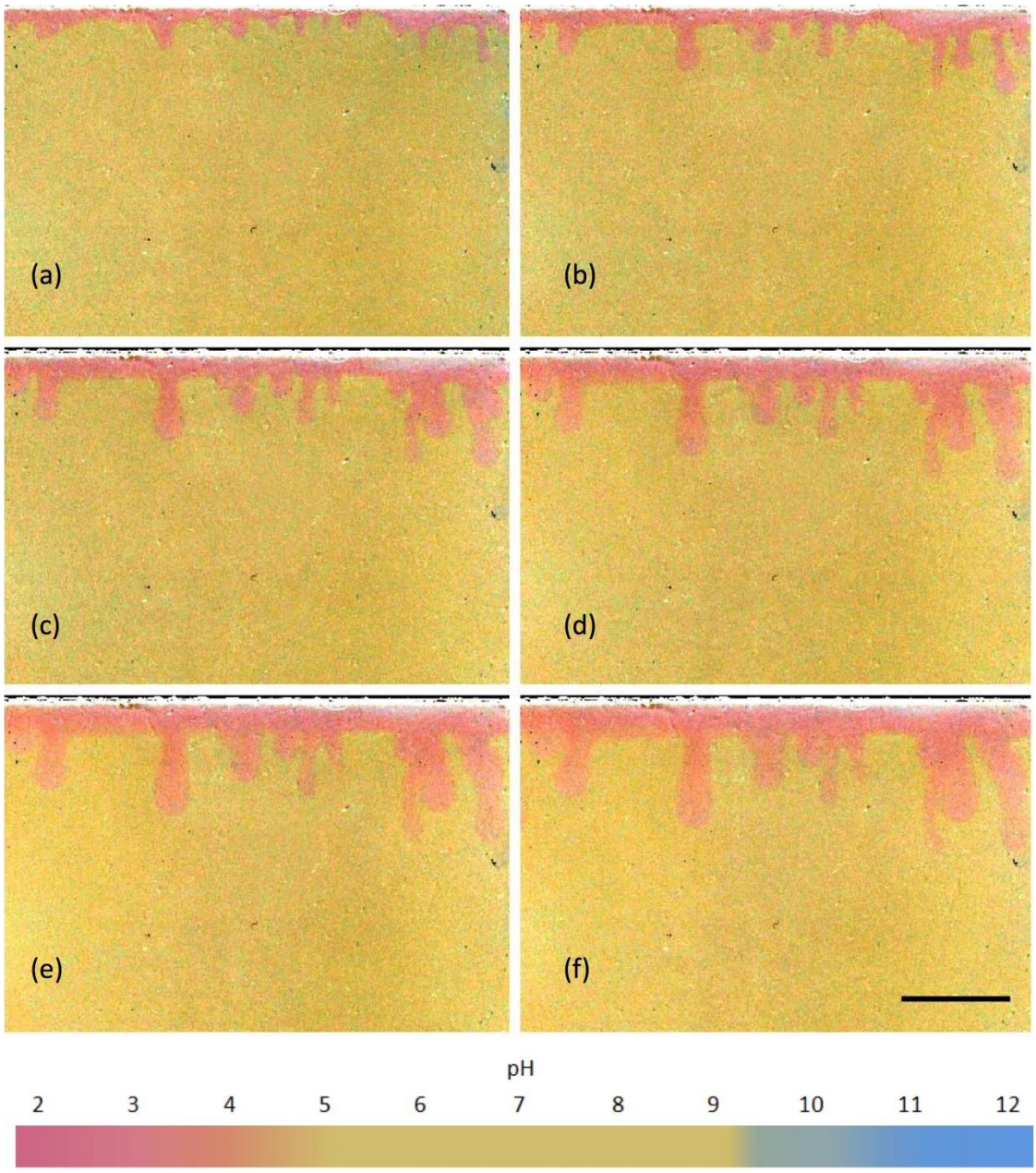

Figure 5.8 Sequence of photographs showing the development of convective instability for the inert case, Ra = 3.4×10^4, at dimensionless times (a) $t' = 5.0 \times 10^4$, (b) $t' = 1.0 \times 10^5$, (c) $t' = 1.5 \times 10^5$, (d) $t' = 2.0 \times 10^5$, (e) $t' = 2.5 \times 10^5$, and (f) $t' = 1.0 \times 10^5$. The scale bar represents 20 mm (dimensionless length $L' = 10^4$).

5.2.2 Convective finger depth

To quantify the evolution of the convective fingers, the vertical extent of the domain penetrated by the solute was measured. This length was defined as the distance from the interface to the tip of the longest finger and was tracked by measuring the transverse-averaged concentration profiles $\langle C_{AT}{}'(z',t')\rangle = (1/L_x{}') \int_0^{L_x{}'} C_{AT}{}'(x',z',t')\,dx'$ at specific times. The dimensionless total concentration of acid added $C_{AT}{}'$ was calculated from the images using the hue pixel value conversion method outlined in §5.1 .The transverse-averaged profiles for the inert case with Ra = 3.4×10^4 are shown in Figure 5.9 with the error bars corresponding to the propagation of pH measurement error when calculating $C_{AT}{}'$ using Figure 5.7.

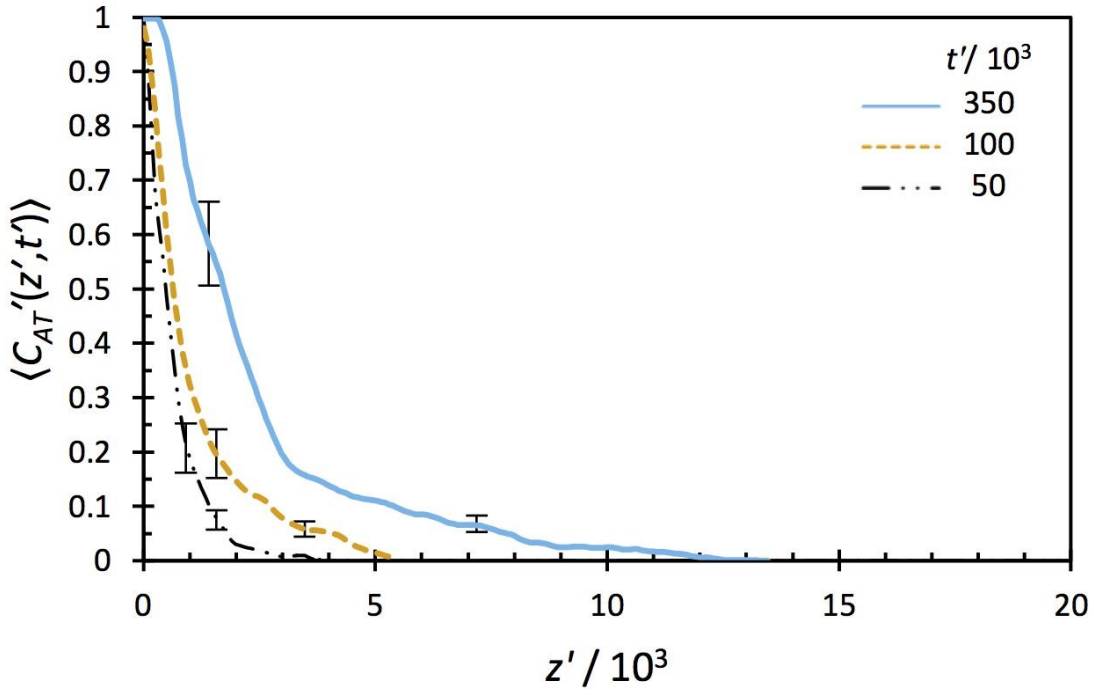

Figure 5.9 Transverse-averaged solute concentration profiles $\langle C_{AT}{}'(z',t')\rangle$ for the inert case Ra = 3.4×10^4, with the bottom, middle and top curves representing the profile at t' = 5.0×10^4, t' = 1.0×10^4 and t' = 3.5×10^5 respectively.

The peaks of the curves grow wider at later times corresponding to an increase in the thickness of the diffusive boundary layer and the area under the curves becomes greater as more solute is transferred to the domain and channelled away from the top boundary. It can be seen that the dimensionless averaged concentration at the interface is approximately 1.0 and thus equal to the aqueous solubility of acetic acid C_{As} in

dimensional form. The averaged concentration decreases with distance from the top boundary and the curves penetrate deeper into the domain at later times.

The maximum dimensionless depth of the domain penetrated by the convective fingers L_f' was calculated from the transverse-averaged profiles. This depth was defined as the value of z' at which the transverse-averaged concentration $\langle C_A'(z',t')\rangle$ drops below 0.01 (Nagatsu and De Wit, 2011; Andres and Cardoso, 2012). The evolution of the maximum convective finger depth against time for four different inert cases Ra = 1.1×10^4, 2.2×10^4, 3.4×10^4 and 6.9×10^4 is presented in Figure 5.10. The solute fingers in Figure 5.10(a) were observed to initially grow at a rate similar to that calculated for a purely diffusive profile (Slim, 2014), before convection dominates and fingers display linear growth consistent with previous work. Figure 5.10(b) shows that at later times, the linear growth of convective fingers was observed to slow down for all four inert cases. This has been previously shown by Slim (2014), where the pioneer plumes, penetrating deepest into the domain, were found to decelerate at around $t' \approx 1.6 \times 10^4$ as the rate of mass transfer of solute into the domain reached a constant steady-state value. Despite the differences in the concentrations and gap widths between the different inert cases, it is apparent that they all show the same trend after nondimensional scaling.

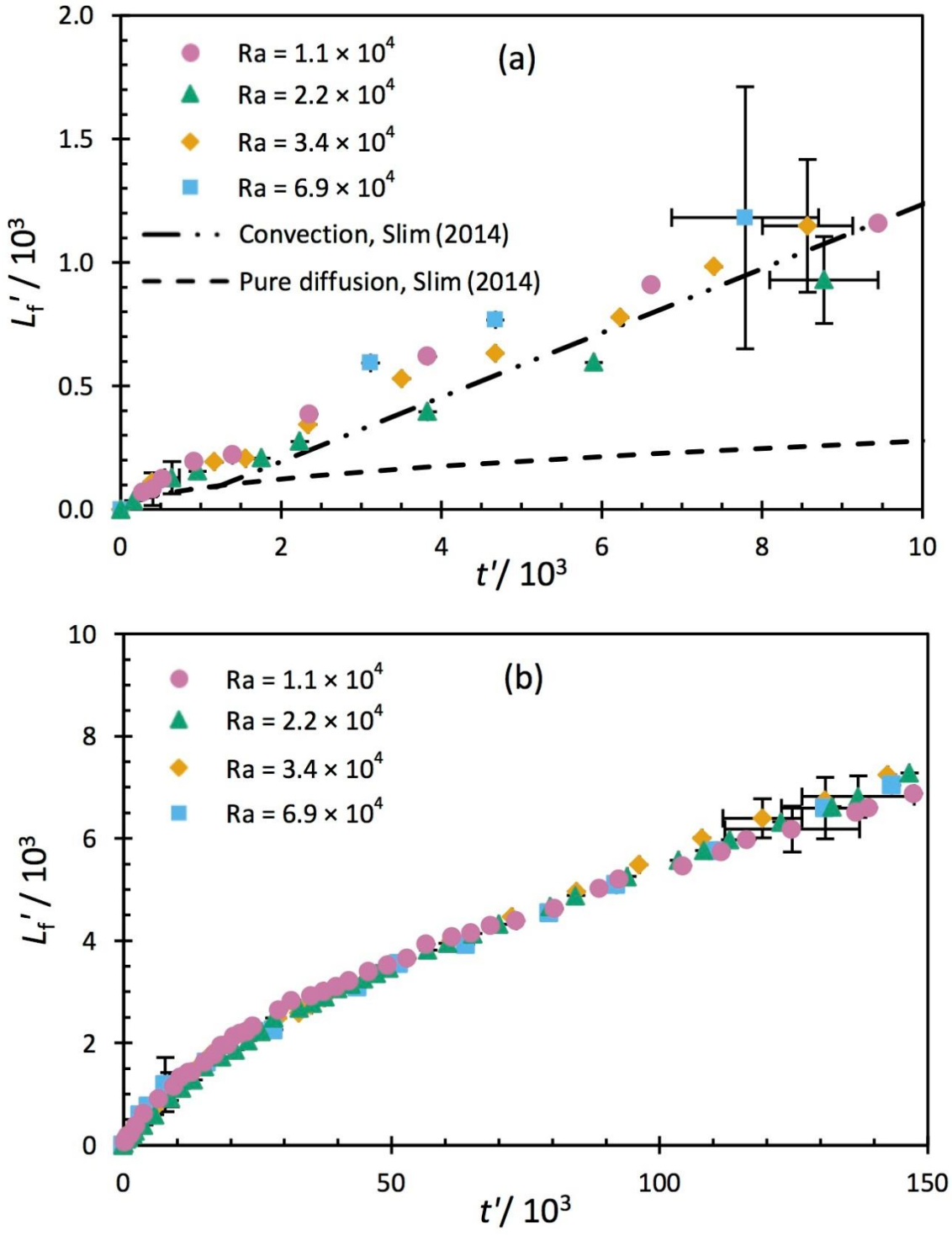

Figure 5.10 Evolution of the maximum dimensionless depth of fingers L_f' for various inert system cases at (a) dimensionless time $0 \leq t' \leq 1.0 \times 10^4$ and (b) $0 \leq t' \leq 1.5 \times 10^5$. Previous numerical simulations for the maximum finger depth for solutal convection and pure diffusion (from Fig. 5 of Slim, 2014) are also shown in (a).

5.2.3 Convective finger wavelength

The interaction between convective fingers was measured by taking the longitudinal-averaged concentration profiles $\langle C_{AT}{}'(x',t')\rangle = (1/L_z{}')\int_0^{L_z{}'} C_{AT}{}'(x',z',t')\,dz'$ across the domain. The longitudinal-averaged profiles for inert case Ra = 3.4×10^4 are shown in Figure 5.11 at dimensionless times of $t' = 5.0 \times 10^4$, $t' = 1.0 \times 10^5$ and $t' = 3.5 \times 10^5$. The bottom curve shows the concentration profile at $t' = 5.0 \times 10^4$ and the peaks represent the convective fingers that develop from the boundary layer. The peaks of subsequent curves grow taller and wider as the fingers grow and sink deeper into the domain. The small peaks that are visible at early times merge together to form fewer, larger peaks consistent with the merging behaviour of neighbouring convective fingers as time proceeds.

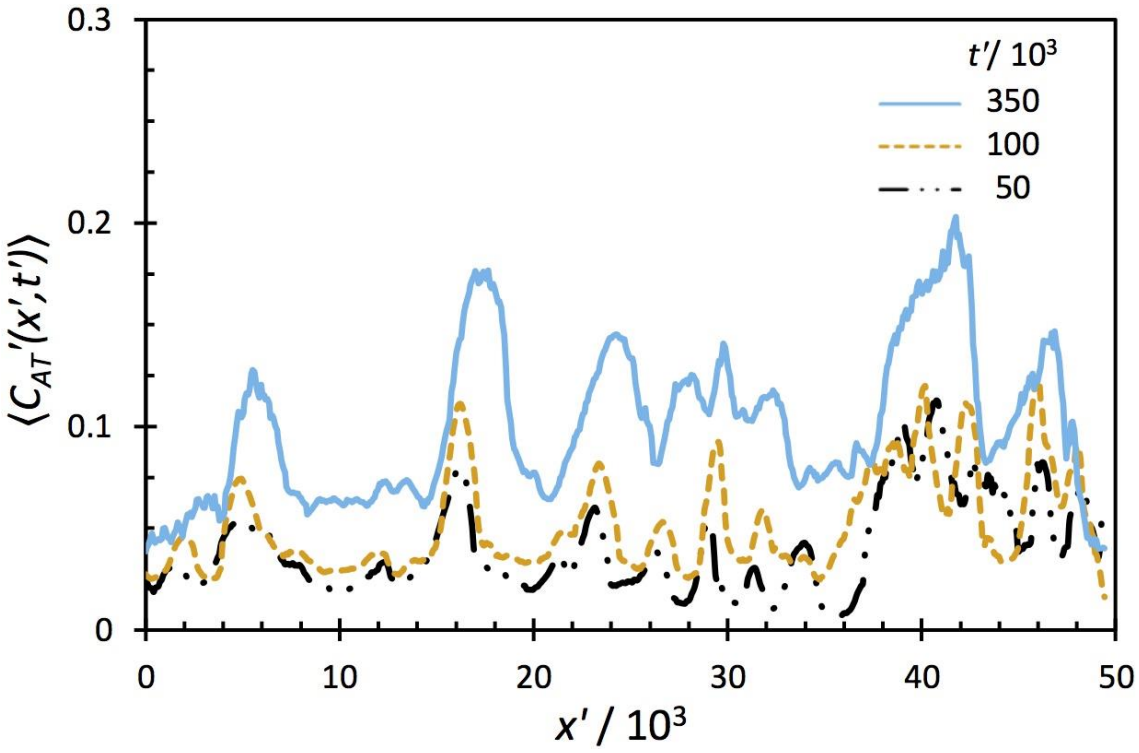

Figure 5.11 Longitudinal-averaged solute concentration profiles $\langle C_{AT}{}'(x',t')\rangle$ for the inert case Ra = 3.4×10^4, with the bottom, middle and top curve representing the profile at $t' = 5.0 \times 10^4$, $t' = 1.0 \times 10^5$ and $t' = 3.5 \times 10^5$ respectively.

The distance between the peaks can be measured to give the wavelength of the convective fingers and thus make it possible to quantitatively assess the extent of finger interaction. The longitudinal-averaged profiles were decomposed into Fourier modes to quantify the dimensionless averaged wavelength of the fingers $\lambda' = 2\pi/\langle f'(t')\rangle$. The power averaged mean wavenumber was defined as $\langle f'(t')\rangle = \sum f_i' P_i / \sum P_i$ where f_i' are the Fourier modes of the Fast Fourier Transform of the longitudinal-averaged profile and $P(f')$ are their amplitudes in Fourier space (Zimmerman and Homsy, 1991). The evolution of the dimensionless wavelength for the four inert cases investigated in the previous section is plotted in Figure 5.12.

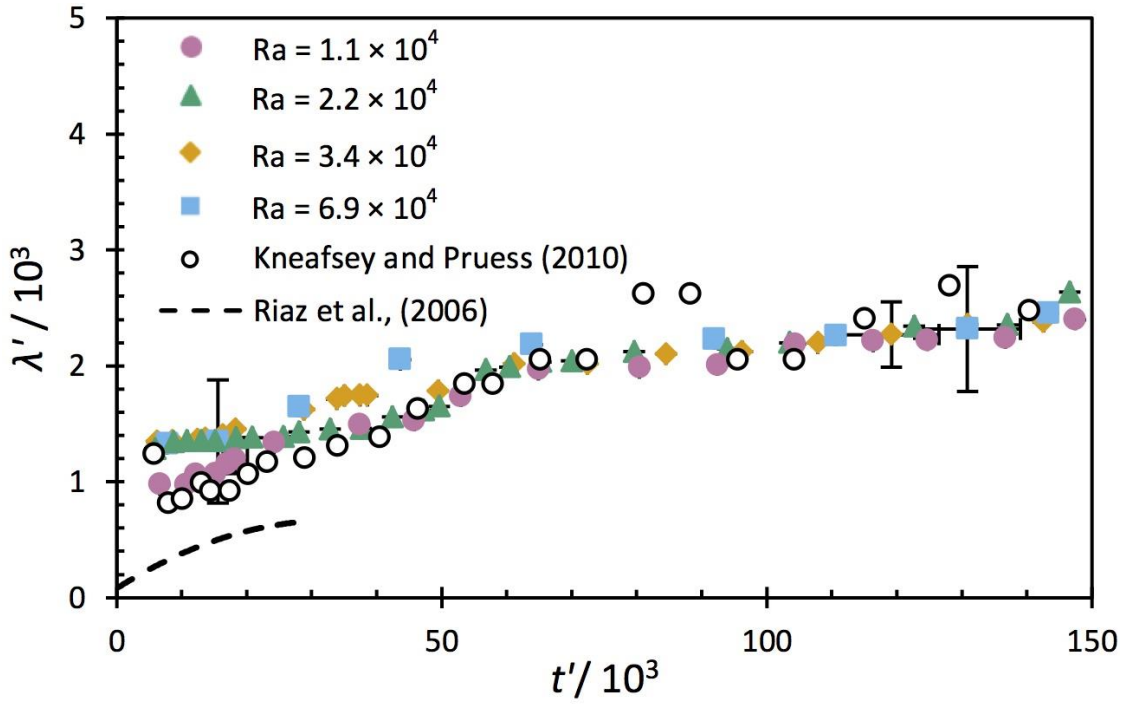

Figure 5.12 Dimensionless wavelength of fingers λ' as a function of dimensionless time t' for various inert system cases. Previous experimental (Fig. 4, Kneafsey and Pruess, 2010) and numerical results (Fig. 11, Riaz et al., 2005) are also shown.

The four cases again show very similar results after scaling and are in agreement with the results of previous experiments carried out by Kneafsey and Pruess (2010) for a CO_2 – brine laboratory system at ambient conditions. The average initial dimensionless wavelength for the inert cases was measured to be $(1.23 \pm 0.28) \times 10^3$ and as neighbouring fingers merge together during the course of each experiment, the wavelength of instability was seen to increase as a function of time. The initial wavelength for the experimental cases was measured to be larger than the wavelengths

from numerical simulations performed by Riaz et al. (2005). This is most likely due to the fact that some finger merges may have already occurred before the instabilities become visible in experiments, giving rise to a larger wavelength.

5.2.4 Time for onset of convection

The time for onset of convection t_{oc}', was defined as the time at which convective fingers were first observed to emerge from the diffusive boundary layer. The sequence of images in Figure 5.13 shows how the dissolution of acetic acid into the lower aqueous layer results in the development of convective instabilities for the inert case with Ra = 2.2×10^4 (C_{As} = 0.113 M, h = 0.8 mm). The red acidic boundary layer grows with time until the density between the acetic acid solute and the surrounding bulk fluid is great enough for convective fingers to form. The first instance of regular finger-like structures can be observed in Figure 5.13(c) and therefore the dimensionless time for onset of convection for this case was recorded as approximately 38 secs ($t_{oc}' \approx 6 \times 10^3$). It could be argued that there is some evidence of instabilities forming on the right hand side of Figure 5.13(b), however it was decided to take the value of t_{oc}' at the time when it could be said that convective fingers are visible.

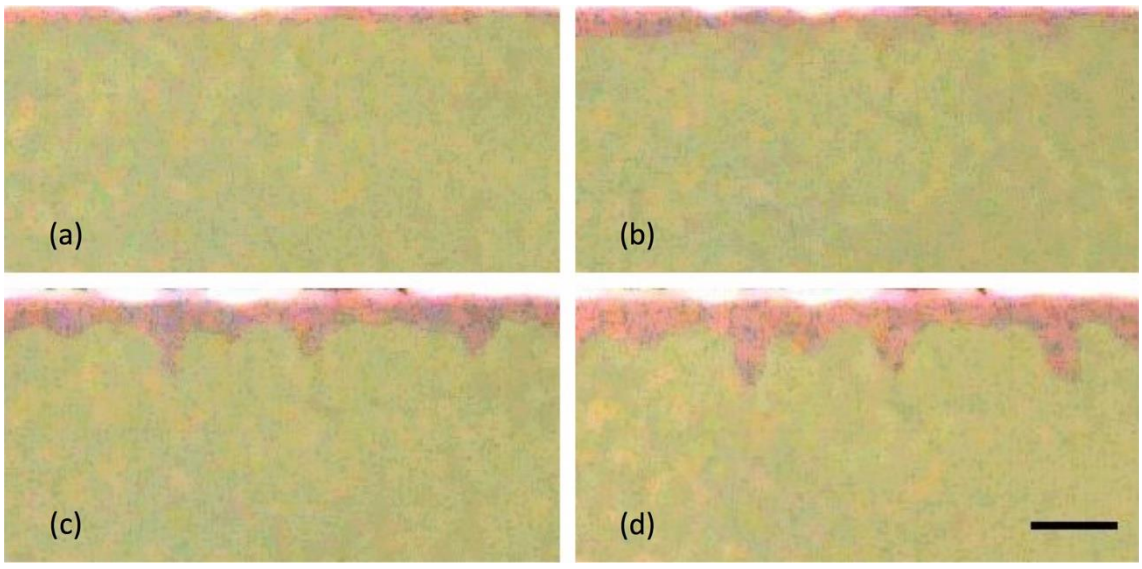

Figure 5.13 Development of convective instability for the inert case, Ra = 2.2×10^4, at dimensionless times (a) $t' = 4 \times 10^3$, (b) $t' = 5 \times 10^3$, (c) $t' = 6 \times 10^3$ and (d) $t' = 7 \times 10^3$. The scale bar represents 3 mm corresponding to a dimensionless length $L' = 10^3$.

Numerical studies have reported dimensionless times for onset of convection ranging from $t_{oc}' = 8.50 \times 10^2$ (Ghesmat et al., 2011) to $t_{oc}' = 5.62 \times 10^3$ (Hidalgo and Carrera, 2009). The average observed $t_{oc}' \approx (6.17 \pm 0.49) \times 10^3$ for the inert cases in this experimental system is slightly larger than the previously determined values. However, this overestimation can again be attributed to the uncertainty associated with differentiating early convective fingers by the naked eye. Although the average dimensionless onset time was consistent for all of the inert cases, the convective flow developed faster in the dimensional time-scale for cases with increasing Rayleigh number due to the increase in the density difference driving convection and/or the permeability of the cell. It was therefore not possible to determine an accurate estimate of the onset time for the cases with Ra > 3.4×10^5 as the flow was too fast to be resolved by the laboratory equipment.

5.2.5 Mass flux

The rate of solute mass transfer is an important measure in understanding the dissolution of CO_2 and the storage potential of saline aquifers. The total mass of acetic acid transferred to the domain per unit interfacial area was calculated in dimensional form $M_A(t) = (1/L_x) \int_0^{L_z} \int_0^{L_x} C_{AT}(x,z,t)\, dxdz$ for each inert case. The dissolution flux of acetic acid was defined as the rate of total mass transferred $J_A = dM_A/dt$ and a constant steady-flux regime was observed after the onset of convection.

The steady-flux regime has previously been quantified for the CO_2 – brine and other analogue systems using the dimensionless Sherwood number $\mathrm{Sh} = J_A L_z/(DC_{As})$, the ratio of convective mass transfer rate to the rate of diffusive mass transport. The Sherwood number for the inert cases of the MIBK – acetic acid – water experimental system was calculated and plotted as the black diamonds in Figure 5.14. The results show a sublinear scaling relation between the Sherwood and Rayleigh numbers $\mathrm{Sh} = (0.040 \pm 0.018)\mathrm{Ra}^{0.86\pm0.04}$. This agrees with existing numerical (Farajzadeh et al., 2013) and experimental (Backhaus et al., 2011; Neufeld et al., 2010; Tsai et al., 2013) results with Ra exponents approximately equal to 0.8. These slight variations in the value of the exponent are attributed to the error in calculating the convective flux, the differences in fluid systems and the different experimental setups.

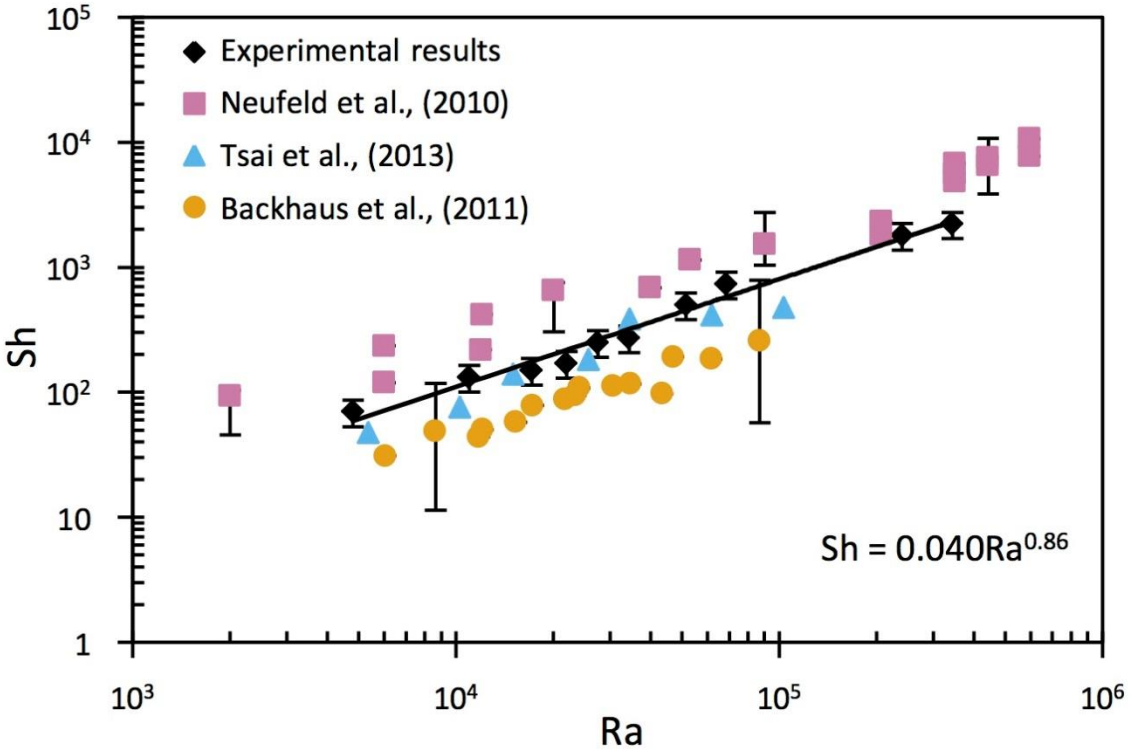

Figure 5.14 Dimensionless convective flux expressed as the Sherwood number, Sh = $J_A H/(D\phi C_{As})$, as a function of Rayleigh number, Ra, for different inert systems. The solid line is the best power-law fit of the form Sh = $(0.040 \pm 0.018)\mathrm{Ra}^{0.86\pm0.04}$ for the inert MIBK – acetic acid – water system under investigation.

5.2.6 Conclusions

Experiments for the inert cases of the MIBK – acetic acid – water system have shown that the transfer of acetic acid to the lower aqueous results in the formation of convective fingers. These fingers were found to sink into the domain and merge to form larger fingers with time. This behaviour was quantified and the results agree with previous work, thus validating the proposed experimental system as a suitable analogue for modelling the dissolution of CO_2 in brine. Using the same methodology, the more complex effect of reaction on the flow pattern of solute is investigated in the next chapter.

6 EXPERIMENTAL RESULTS: REACTIVE SYSTEM

Theoretical analysis of buoyancy-driven convection in a fluid saturated porous medium coupled with an $A + B \rightarrow C$ second-order chemical reaction has shown that the flow is governed by: the dimensionless solutal expansion coefficients of the chemical species β_A', β_B', β_C'; the initial dimensionless concentration of reactant B, C_{Bo}'; and the dimensionless group Da/Ra^2 which measures the timescale of convection compared to those for reaction and diffusion.

For a given chemical system, the values for the solutal expansion coefficients are fixed, so the dynamics of the reactive system are fully determined by C_{Bo}' and Da/Ra^2. For the MIBK – acetic acid – aqueous ammonia system used as an experimental analogue to model the flow of CO_2 in saline aquifers, the dimensionless solutal expansion coefficients for acetic acid, ammonia and the ammonium acetate product of reaction are $\beta_A' = 1.0$, $\beta_B' = -0.9$, and $\beta_C' = 1.8$ respectively. The destabilising effect of reaction on the system is investigated in this chapter and the results of a systematic experimental study varying C_{Bo}' and Da/Ra^2 are presented in sections §6.1 and §6.2 respectively. The experimental results are then compared to theoretical work and numerical simulations of the same physicochemical system in section §6.3.

6.1 EFFECT OF C_{BO}'

To understand the effect of the excess of the environmental reactant species relative to the diffusing solute, Da/Ra^2 was kept constant and equal to 2.9×10^7 (C_{As} = 0.113 M, h = 1.0 mm, Ra = 3.4×10^4), whilst the initial dimensionless concentration of ammonia dissolved in the lower aqueous layer C_{Bo}' was varied in the range 0 – 1. It is expected that for the physicochemical system under investigation, the formation of dense aqueous product will have a destabilising effect on the system and an increase in C_{Bo}' will result in the acceleration of buoyant convection.

An image sequence portraying the evolution of convective fingers in the lower layer is shown in Figure 6.1. The acid *A* diffuses from the upper cell into the lower layer forming a boundary layer that grows in thickness with time. Concomitantly, *A* reacts with the base *B* present in the lower layer to form the heavy product *C*. Eventually, this boundary layer becomes unstable, breaking into a number of dense fingers that sink into the lower layer domain. There is a sharp visible boundary that separates the fingers, where $C_{AT}' > 0$ and $C_B' = 0$, from the bulk fluid, where $C_{AT}' = 0$ and $C_B' = C_{Bo}'$. Given that the initial concentration of *B* is much smaller than the concentration of *A* at the top boundary for all cases except for $C_{Bo}' = 1$, depletion of *B* is rapid compared to the time scale of mixing, and therefore reaction is limited to a narrow region between the solute and the base *B*. The fingers for the inert case ($C_{Bo}' = 0$) show up red as they are acidic. As C_{Bo}' is increased, neutral yellow-coloured product can be observed to form around the tips and edges of the fingers. With increasing C_{Bo}', the pH of fingers increases and they become more yellow, suggesting that a greater amount of product is formed by reaction. The convection mechanism is essentially the same for the reactive cases as for the inert case with no reaction, except that the density contribution of denser product *C* adds to that of the dissolving species *A*. The formation of product is seen to disturb the regular pattern of rounded fingers that is observed for the inert and weakly reactive cases, with the boundary layer at the interface becoming narrower and the dense product sinking deeper in the domain via thinner and more irregular convective fingers at higher C_{Bo}'. The yellow-coloured fingers for the cases with $C_{Bo}' = 10^{-2}$, 10^{-1} and 1 undergo tip-splitting as the heavy product pulls solute away from the interface and induces stronger convection in the lower layer.

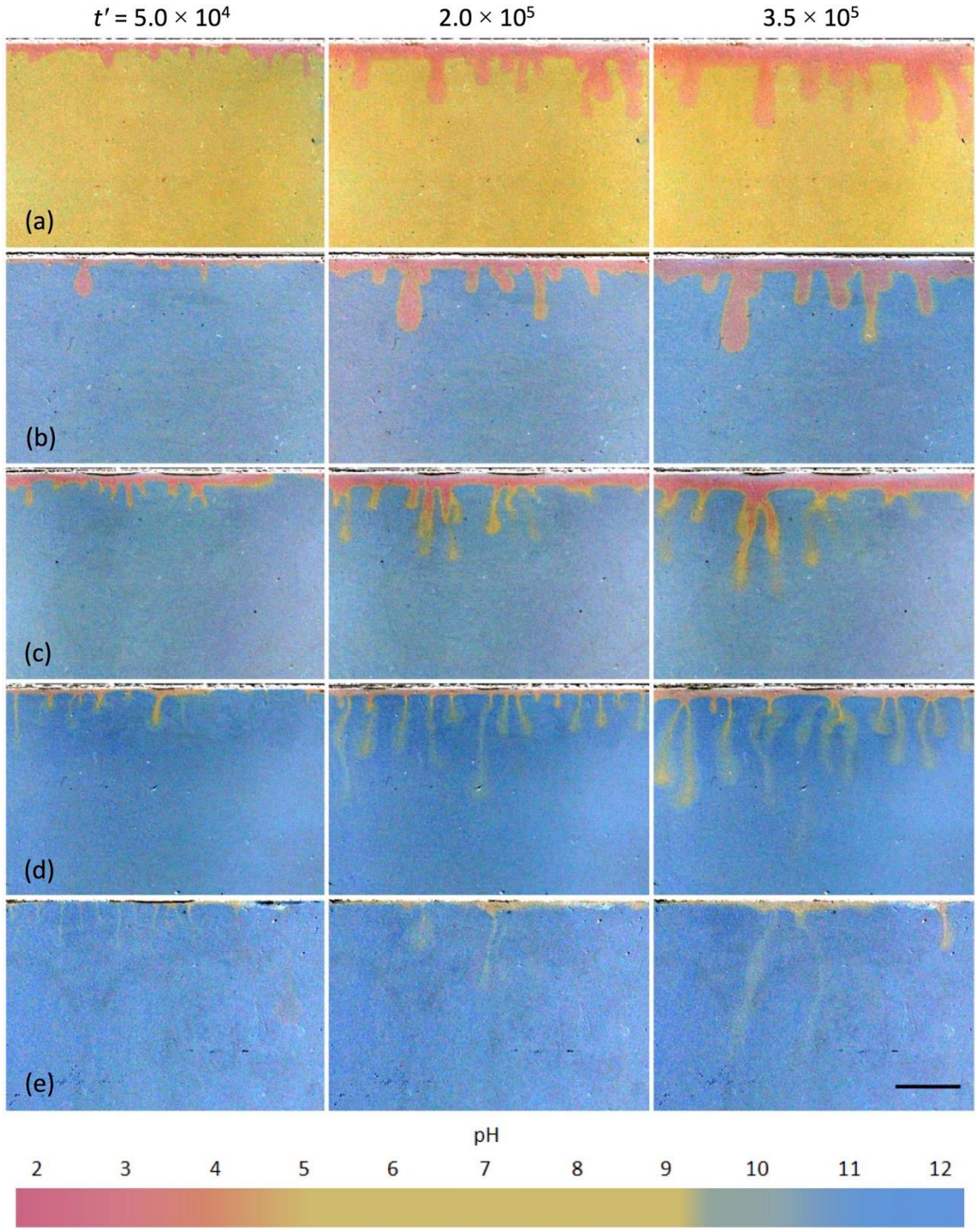

Figure 6.1 Sequence of photographs showing the development of convective instability for experimental cases with various initial dimensionless concentrations of ammonia (a) $C_{Bo}' = 0$, (b) $C_{Bo}' = 10^{-3}$, (c) $C_{Bo}' = 10^{-2}$, (d) $C_{Bo}' = 10^{-1}$ and (e) $C_{Bo}' = 1$. The scale bar represents 20 mm (dimensionless length $L' = 10^4$). Each image was edited using ImageJ.

6.1.1 Convective finger depth

Transverse-averaged concentration profiles were calculated for the experimental cases shown in Figure 6.1 by averaging the concentration field $\langle C_{AT}'(z',t')\rangle = = (1/L_x') \int_0^{L_{x'}} C_{AT}'(x',z',t')\, dx'$ at specific times. The average concentration profiles in Figure 6.2 cover the same dimensionless time range for each case, showing the growth of the acid solute layer from the top of the domain towards the bottom boundary. As C_{Bo}' increases, the fingers become poorer in *A* and the heavy product accelerates their downward motion with convection occurring in a deeper region of the domain, but containing only a small concentration of solute *A*. The diffusive boundary layer for $C_{Bo}' = 10^{-1}$ is narrower than for the other cases in Figure 6.2(a) – (c), suggesting that reaction is strong enough to consume the solute and transport the product in rapidly descending fingers before the boundary layer can build up.

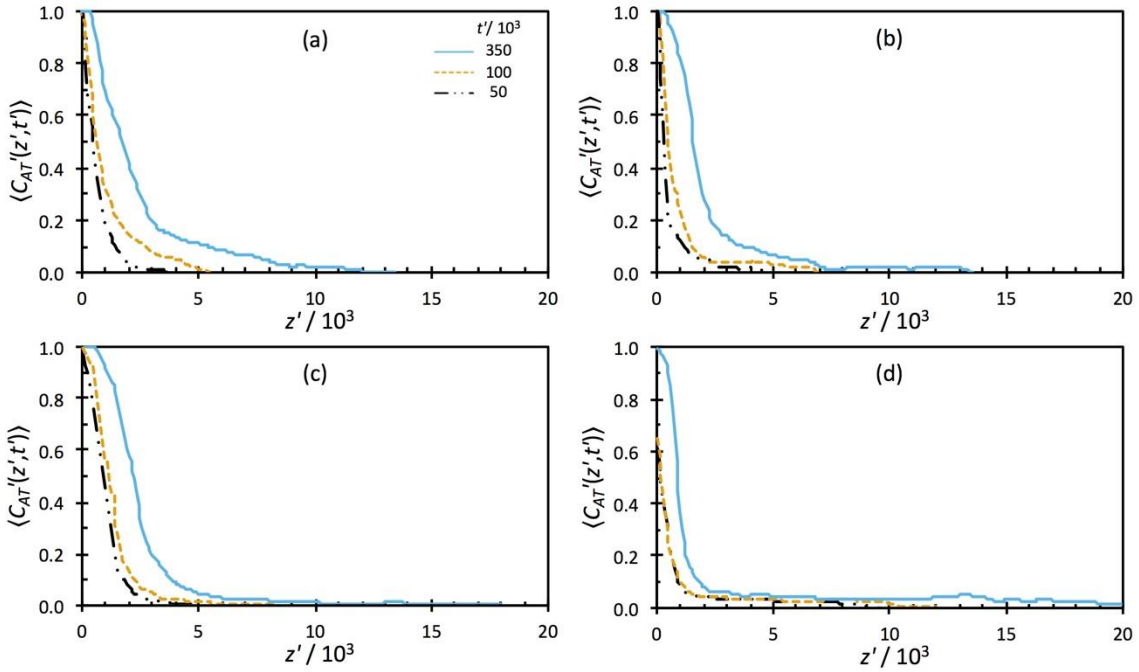

Figure 6.2 Transverse-averaged solute concentration profiles of cases $\langle C_{AT}'(z',t')\rangle$ of cases: (a) $C_{Bo}' = 0$, (b) $C_{Bo}' = 10^{-3}$, (c) $C_{Bo}' = 10^{-2}$ and (d) $C_{Bo}' = 10^{-1}$. All four plots cover the same time range $0 \leq t' \leq 3.5 \times 10^5$, each with the bottom, middle and top curve representing the profile at $t' = 5.0 \times 10^4$, $t' = 1.0 \times 10^5$ and $t' = 3.5 \times 10^5$ respectively.

The effect of C_{Bo}' on the maximum dimensionless depth of the domain penetrated by convective fingers was calculated by measuring the value of z' at which the transverse-averaged concentration $\langle C_{AT}'(z',t') \rangle$ drops below 0.01 and plotted as a function of dimensionless time in Figure 6.3.

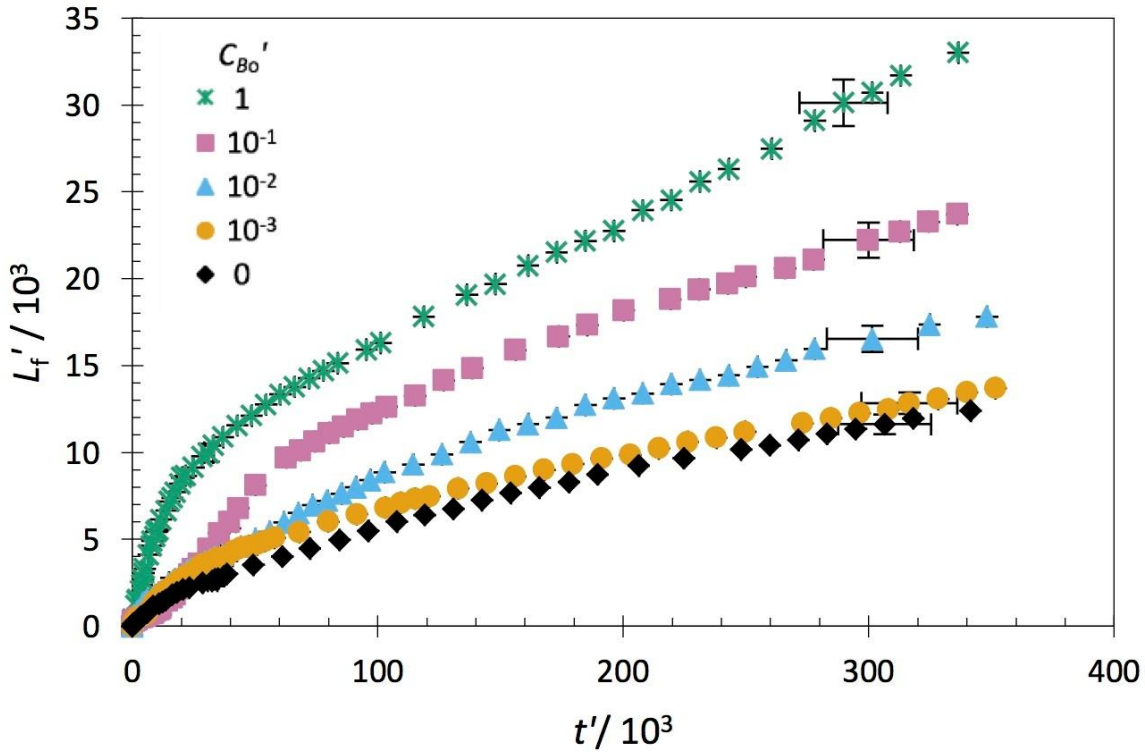

Figure 6.3 Evolution of the maximum dimensionless depth of convective fingers L_f' for various C_{Bo}' in the range 0 – 1.

After convection is established, the location of the finger front initially advances linearly in time, with the rate increasing as C_{Bo}' increases. As the fingers merge and channeling slows down at larger times, the growth rate of the larger fingers decelerates. The inert and weakly reactive cases (C_{Bo}' = 0 and 10^{-3}) grow at very similar rates suggesting that the effect of reaction and formation of product is not sufficient to affect the development of the fingers. As C_{Bo}' increases the fingers penetrate deeper into the domain when considering the whole finger which contains both the solute and product species. Convective fingers contain the solute and product species at different concentrations. To differentiate the region where the solute A remains the dominant species, only the parts of the fingers with pH less than 4.75 were taken into account in Figure 6.4.

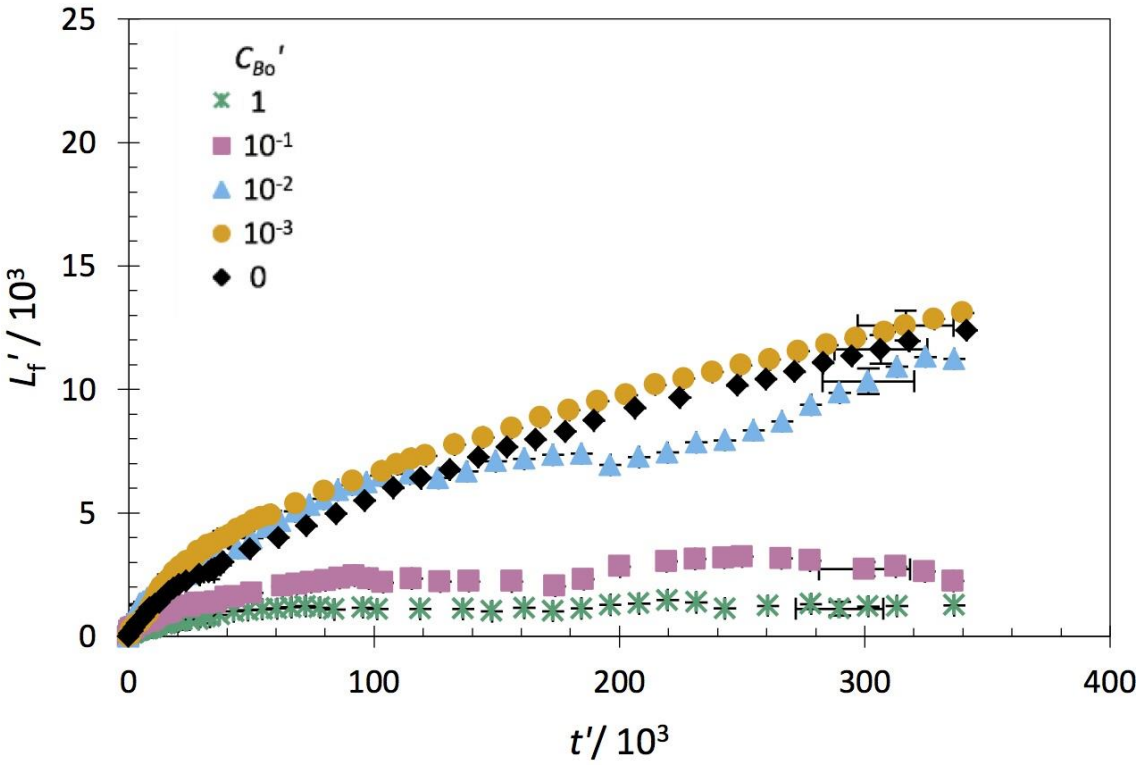

Figure 6.4 Evolution of the maximum dimensionless depth of convective fingers L_f' for various C_{Bo}' when considering only the region of the fingers with pH ≤ 4.75 where solute *A* is the dominant species.

It can be seen that the growth and development of the solute-rich zone for the case with $C_{Bo}' = 10^{-3}$ remains more or less identical to the inert case, just as in Figure 6.3. When ignoring the product species for the cases with strong reaction ($C_{Bo}' = 10^{-1}$ and 1), a very different type of behaviour was observed compared to when considering the whole finger, with the solute-rich region slowly growing to approximately $z' = 2 \times 10^3$ for $C_{Bo}' = 10^{-1}$ and $z' = 1 \times 10^3$ for $C_{Bo}' = 1$ in Figure 6.4 and this reactive layer remains confined to a narrow region close to the top boundary interface of the domain. This implies that for the cases with $C_{Bo}' = 10^{-1}$ and 1, the fingers sinking deep into the lower aqueous layer consist predominantly of the nonreactive and chemically neutral product of reaction. This means that the deeper parts of the domain, outside of the solute rich layer, are chemically inactive and it is the density difference between the product and the bulk fluid that is responsible for enhancing the depth penetrated by the mixed layer.

6.1.2 Convective finger wavelength

To quantify the interaction between fingers as a function of time, the longitudinal-averaged concentration profiles, $\langle C_{AT}'(x',t')\rangle = (1/L_z')\int_0^{L_z'} C_{AT}'(x',z',t')\,dz'$ were calculated. Each plot in Figure 6.5 covers the same dimensionless time range, with the lowest profile taken at the earliest time. As fingers develop in the domain, they are observed to grow individually before merging into fewer, larger fingers. As more solute is transferred and the fingers penetrate deeper into the lower layer, the average concentration can be seen to increase with time for each case. As C_{Bo}' is increased, the finger peaks become narrower corresponding to the long slender fingers in Figure 6.1. With increasing C_{Bo}', the number of fingers in the domain was also found to increase, suggesting that the presence of strong reaction considerably enhances the formation of fingers over the same period of time.

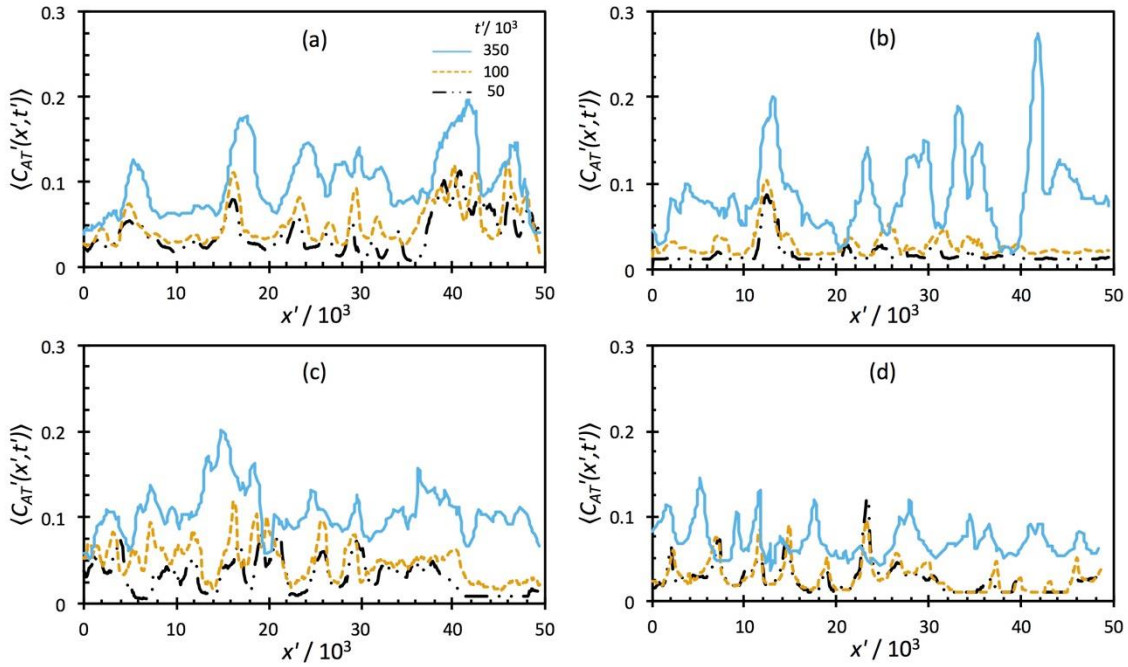

Figure 6.5 Longitudinal-averaged solute concentration profiles $\langle C_{AT}'(x',t')\rangle$ of cases: (a) $C_{Bo}' = 0$, (b) $C_{Bo}' = 10^{-3}$, (c) $C_{Bo}' = 10^{-2}$ and (d) $C_{Bo}' = 10^{-1}$. All four plots cover the same time range $0 \leq t' \leq 3.5 \times 10^5$, each with the bottom, middle and top curve representing the profile at $t' = 5.0 \times 10^4$, $t' = 1.0 \times 10^5$ and $t' = 3.5 \times 10^5$ respectively.

The dimensionless averaged wavelength of the fingers $\lambda' = 2\pi/\langle f'(t')\rangle$ was measured by calculating the Fast Fourier Transform of the longitudinal-averaged concentration profiles to find the power averaged mean wave number using the method described in the previous chapter. The plots in Figure 6.6 show that the averaged wavelength was found to increase with time for each of the experimental cases.

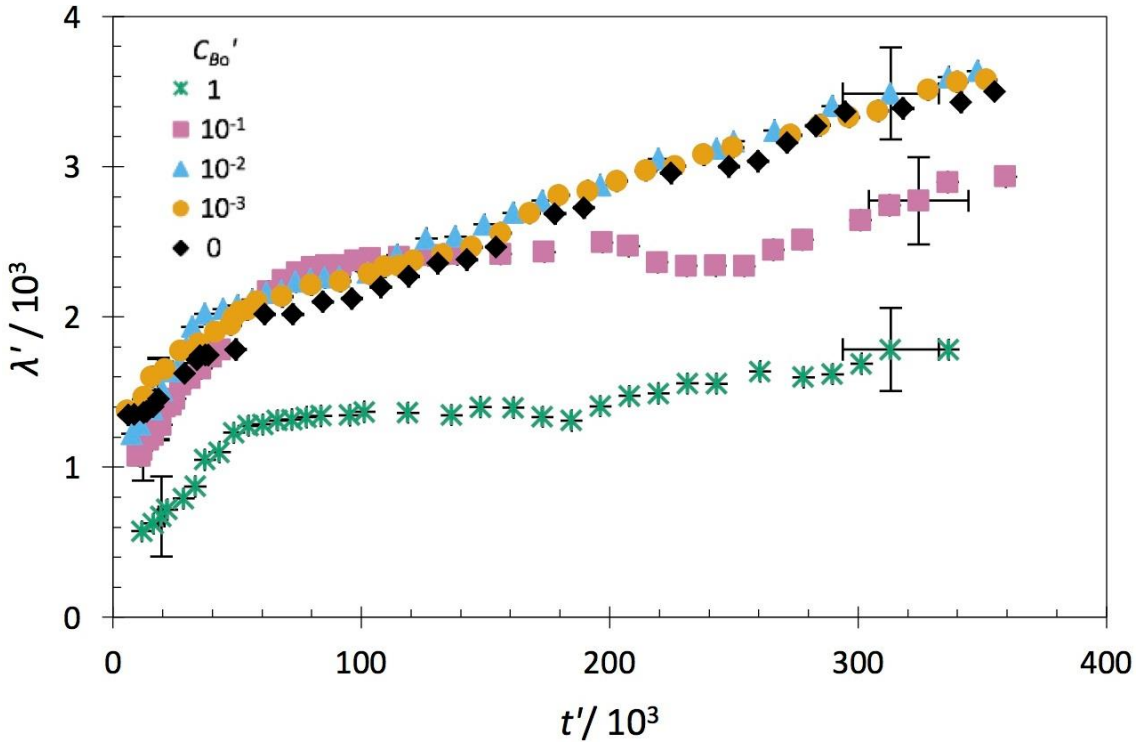

Figure 6.6 Dimensionless wavelength of convective fingers λ' as a function of dimensionless time t' for various C_{Bo}'.

Very similar behaviour was observed for the inert and weakly reactive cases ($C_{Bo}' = 0$, 10^{-3} and 10^{-2}), where the initial fingers were found to have a dimensionless wavelength on average equal to approximately $(1.31 \pm 0.27) \times 10^3$ and as these fingers grew and developed, their number decreased due to adjacent fingers merging together, resulting in a steady increase in the averaged wavelength.

For the cases with strong reaction, the dimensionless wavelength of the initial instability was measured to be $(1.07 \pm 0.27) \times 10^3$ for $C_{Bo}' = 10^{-1}$ and $(5.73 \pm 2.65) \times 10^2$ for $C_{Bo}' = 1$. As C_{Bo}' is increased more of the acid solute is converted to the heavy product resulting in an even more unstable boundary layer and the formation of a greater number of convective instabilities that grow to become fully formed fingers, thus reducing the averaged wavelength. At later times, the wavelengths for $C_{Bo}' = 10^{-1}$ and 1

are lower than for the weakly reactive cases because the boundary layer continues to be sufficiently unstable to keep producing new fingers of product. This behaviour counteracts the effect of merger between neighbouring fingers that was found to increase the averaged wavelength of the convective instabilities.

6.1.3 Time for onset of convection

The dimensionless time for onset of convection t_{oc}', at which fingers were first observed to emerge from the diffusive boundary layer, was plotted in Figure 6.7. As expected, the destabilising effect of increasing C_{Bo}' was found to decrease the time for onset of convection: the instabilities develop earlier and descend deeper into the domain as C_{Bo}' is increased. The effect is most pronounced for the case with strong reaction, C_{Bo}' =1, where fingers were observed almost four times sooner than for the inert case with no reaction.

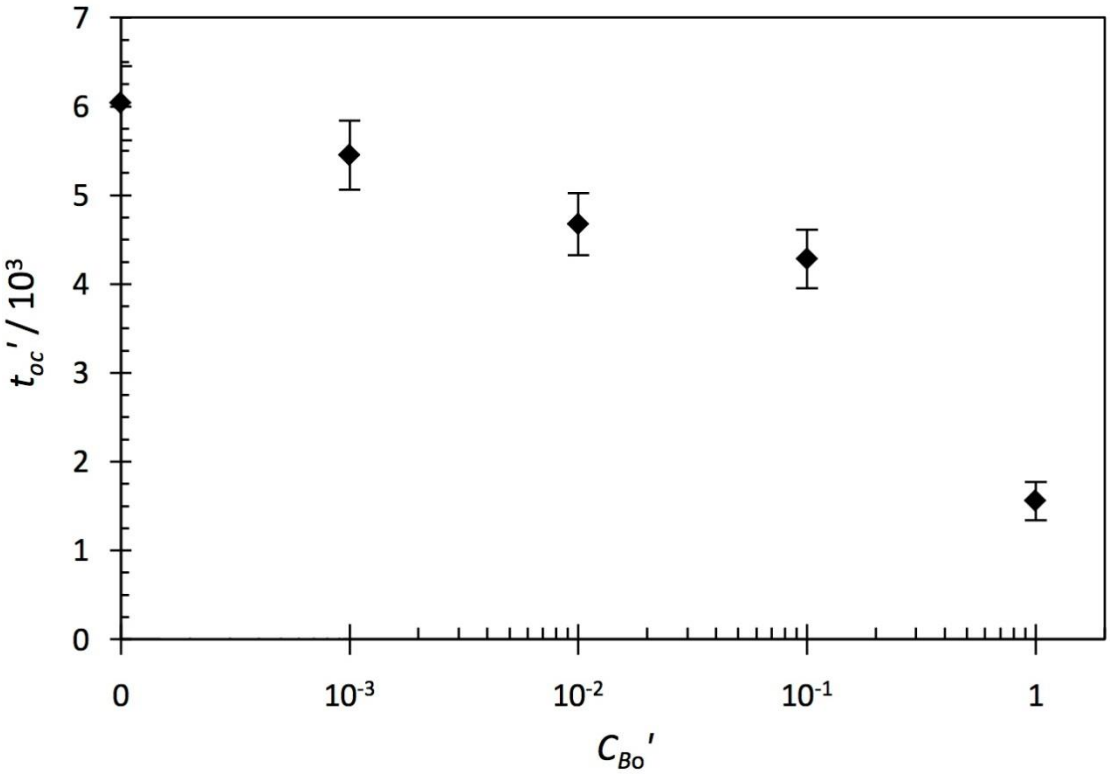

Figure 6.7 The effect of C_{Bo}' on the dimensionless time for onset of convection t_{oc}', defined as the time at which convective fingers were first observed by the naked eye.

6.1.4 Mass flux

The dimensionless mass of solute transferred per unit interfacial area $M_A'(t') = (1/L_x') \int_0^{L_z'} \int_0^{L_x'} C_{AT}'(x', z', t')\, dx' dz'$ is shown as a function of dimensionless time in Figure 6.8. This estimate was made assuming that the concentration of *B* in the environment surrounding the fingers remains approximately constant and equal to C_{Bo}' during the course of an experiment. Measurements of the pH of the bulk fluid deep in the domain away from the fingers and within one finger width from a finger boundary confirmed that the pH was constant within the error of the measurement of ± 0.11.

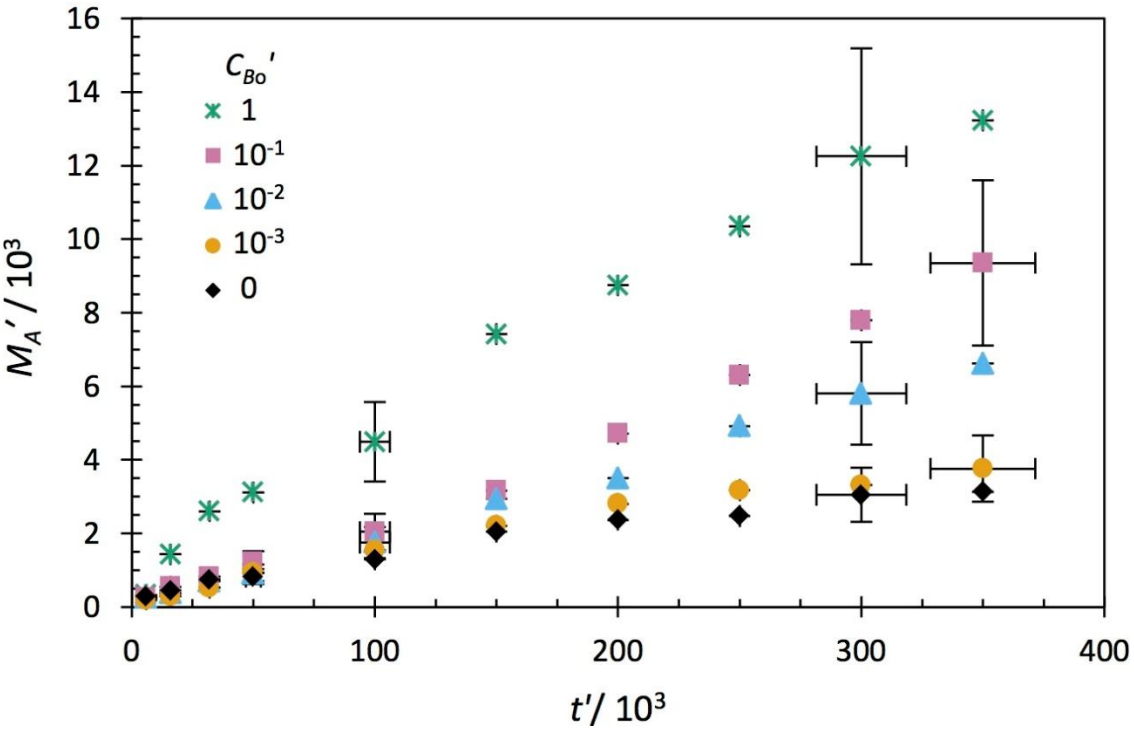

Figure 6.8 Dimensionless mass M_A' of solute *A* transferred to the domain as a function of dimensionless time *t'* for various C_{Bo}'.

The dimensionless mass of *A* presented in Figure 6.8, includes both solute that remains as unreacted acid in the lower aqueous layer as well as the solute that has reacted to form the ammonium acetate product. During the course of each experiment, the amount of acetic acid solute transferred to the domain was found to increase as a function of time. The inert and weakly reactive cases show similar behaviour and the amount of solute transferred is enhanced with increasing C_{Bo}', consistent with earlier observations.

It can be seen that all cases attain a constant mass flux regime, in which M_A' increases linearly as a function of time, with the gradient yielding the dimensionless dissolution

flux of solute $J_A' = dM_A'/dt'$ (Figure 6.9). As expected, reaction increases the transport of *A* into the lower layer, both through accelerated convection and through depletion of *A* near the interface. A deeper convective zone ensures an efficient transport of *A*, with the steady state total mass flux in Figure 6.9 growing by a factor of ~1.5 for each ten-fold increase in C_{Bo}'.

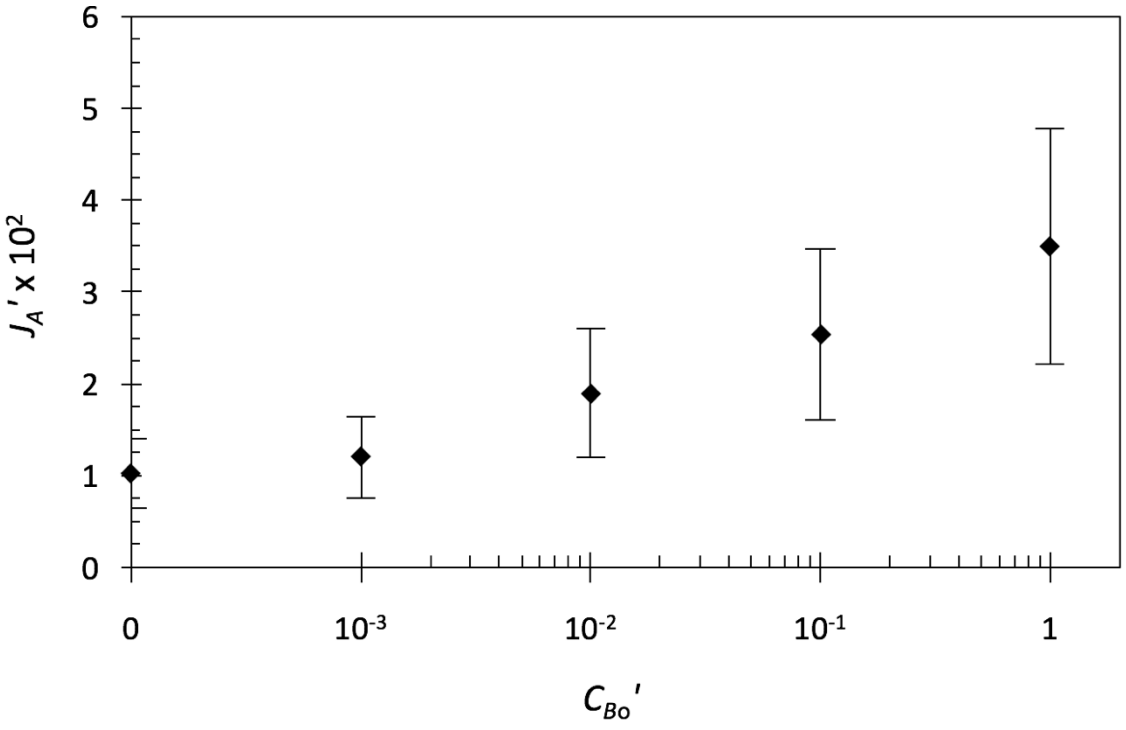

Figure 6.9 Dimensionless steady state total mass flux of solute *A*, $J_A' = J_A L_s/(DC_{As})$ during the constant mass flux regime for various C_{Bo}'.

6.1.5 Conclusions

It has been shown that the extent of convective mixing in the aqueous layer depends strongly on the magnitude of the concentration ratio between the environmental reactant and the diffusing solute species. Experimental measurements suggest that for low C_{Bo}', the fingers are rich in solute and approximately homogeneous in composition. As C_{Bo}' is increased, more of the heavy reaction product is formed, resulting in faster-growing, thinner fingers than before. These complex hydrodynamic and chemical interactions are most pronounced for $C_{Bo}' = 10^{-1}$ and 1, leading to faster growth, smaller wavelength and accelerated mass transport in the reactive system compared to that in the inert.

6.2 Effect of Da/Ra^2

The dimensionless parameter Da/Ra^2 measures the rate of reaction and diffusion compared to convection. As Da/Ra^2 is increased, reaction is expected to dominate over the hydrodynamics and therefore a greater amount of heavy product to be formed per unit time. To evaluate the effect of Da/Ra^2 on the flow in the MIBK – acetic acid – aqueous ammonia system, experiments that were carried out in the previous section were repeated with Da/Ra^2 in the range $2.9 \times 10^6 – 7.1 \times 10^7$. It was not possible to extend the range to lower values of Da/Ra^2 because for $Da/Ra^2 < 2.9 \times 10^6$ the rate of convection was too high and the experiments were therefore too fast to be tracked using the camera. The camera was able to record at a maximum rate of 5 images per second so the development of flow for each case had to be within this limitation to allow for measurements to be made.

The values of Da/Ra^2 were varied by changing the gap width between the cell plates and the initial concentration of acetic acid in the upper organic layer. The initial concentration of ammonia in the lower layer was also varied accordingly to maintain the dimensionless concentration C_{Bo}' at a fixed value for each different case of Da/Ra^2. The same characteristic measurements were taken as in the previous section to determine the effect of Da/Ra^2 on the development of the fluid flow in the lower aqueous layer.

6.2.1 Convective finger depth

The tip of the longest finger was tracked against time to determine how the maximum dimensionless convective finger depth is affected by changes in Da/Ra^2. The experiments were repeated for different values of C_{Bo}' in the range $10^{-3} – 1$ and the dashed line in Figure 6.10 represents the average result for the inert case where $C_{Bo}' = 0$ and Da/Ra^2 is also zero, given that there is no reaction.

The results in Figure 6.10 show that when C_{Bo}' is fixed, the evolution of the convective fingers is very similar for the four different values of Da/Ra^2 under investigation. The slight differences in how the fingers develop, grow and retard with varying Da/Ra^2 are within the error bars for each case, suggesting that Da/Ra^2 has little effect on the results.

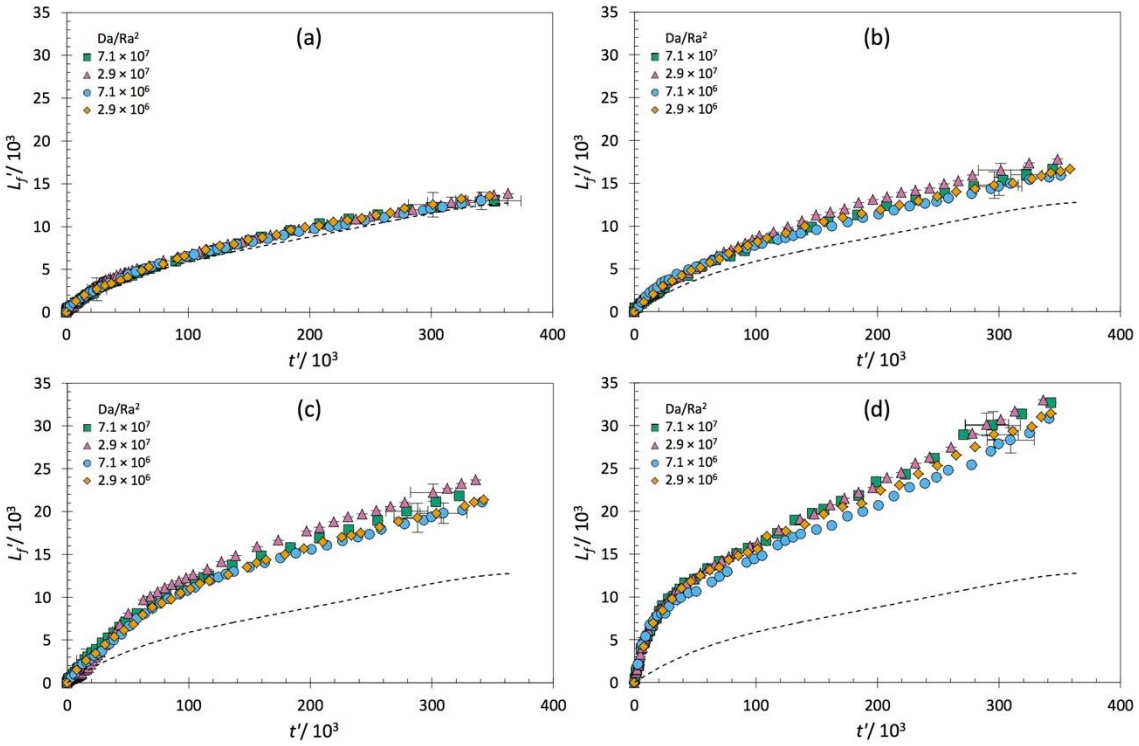

Figure 6.10 Evolution of the maximum dimensionless depth of convective fingers L_f' for various Da/Ra^2 with: (a) $C_{Bo}' = 10^{-3}$, (b) $C_{Bo}' = 10^{-2}$, (c) $C_{Bo}' = 10^{-1}$ and (d) $C_{Bo}' = 1$. The dashed line represents the average result for the inert case with no reaction ($C_{Bo}' = 0$, Da/Ra$^2 = 0$).

The different plots in Figure 6.10 were combined together in Figure 6.11 to show the effects of both C_{Bo}' and Da/Ra^2 on the temporal evolution of the maximum convective finger depth. The different symbol colours represent the results of cases with different C_{Bo}' and the different symbol shapes correspond to the results of the runs with different Da/Ra^2. The same coloured symbols appear grouped together and show a similar growth rate despite the changes in Da/Ra^2. The different coloured results for cases with varying C_{Bo}' are much more distinctive, with an increase in C_{Bo}' shown to enhance the growth rate of the convective fingers. This means that based results from the range of the parameters that have been experimentally investigated, the rate at which the fingers sink into the domain is dependent on C_{Bo}' and not Da/Ra^2.

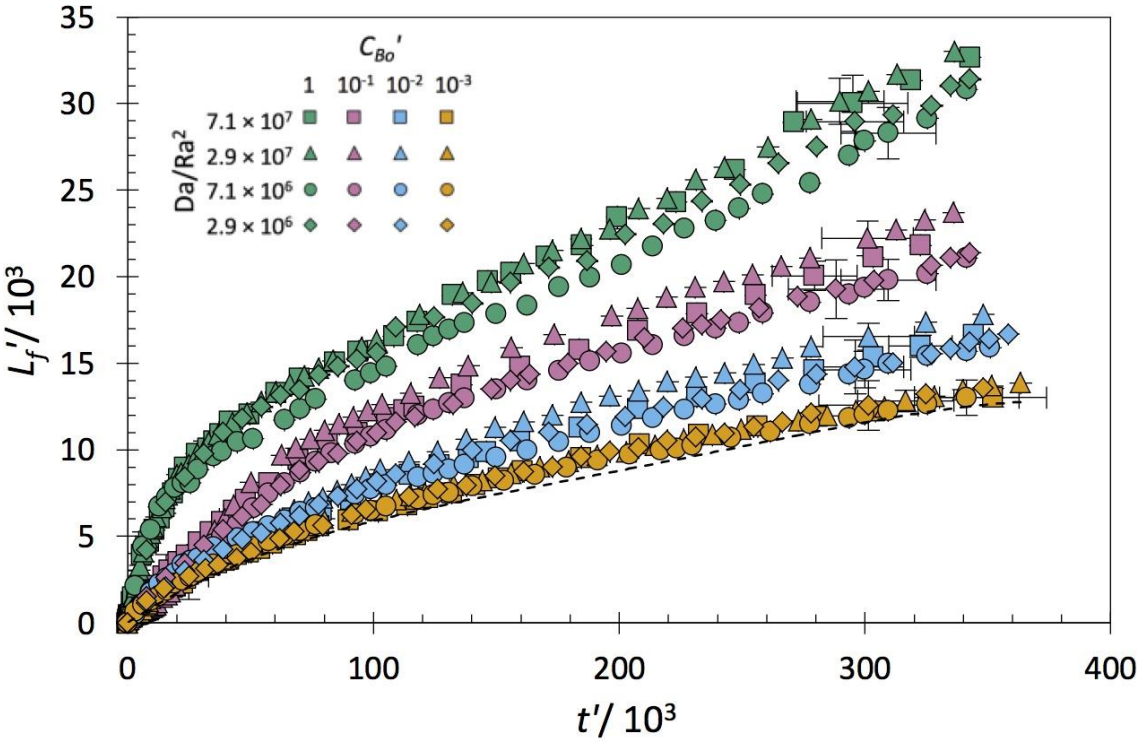

Figure 6.11 Evolution of the maximum dimensionless depth of convective fingers L_f' for all reactive cases. The diamond, circle, triangle and square symbols represent results for $Da/Ra^2 = 2.9 \times 10^6$, 7.1×10^6, 2.9×10^7 and 7.1×10^7, respectively. The dashed line represents the average result for the inert case with no reaction ($C_{Bo}' = 0$, $Da/Ra^2 = 0$).

6.2.2 Convective finger wavelength

The effect of Da/Ra^2 on the temporal development of the dimensionless averaged wavelength of the fingers was also measured for each case of C_{Bo}' and shown in Figure 6.12. It can again be seen that when C_{Bo}' is fixed at a given value, the experimental runs with different Da/Ra^2 produce very similar results. The initial wavelengths measured for the cases with $Da/Ra^2 = 7.1 \times 10^7$ are shown to be smaller than for the cases with $Da/Ra^2 = 2.9 \times 10^6$, suggesting that the increase in the rate of dense product formation may lead to the creation of more instabilities in the boundary layer and therefore more fingers with a smaller initial wavelength. However, these discrepancies are well within the errors quoted for each case, so it is not possible to determine a definite trend in the range of Da/Ra^2 that has been studied. The results also confirm what was seen in the previous section for all four values of Da/Ra^2: the weakly reactive cases ($C_{Bo}' = 10^{-3}$ and 10^{-2}) show very similar results to the inert case with no reaction ($C_{Bo}' = 0$) and the averaged wavelength becomes smaller as C_{Bo}' is increased to 10^{-1}, with the effect even more pronounced for $C_{Bo}' = 1$.

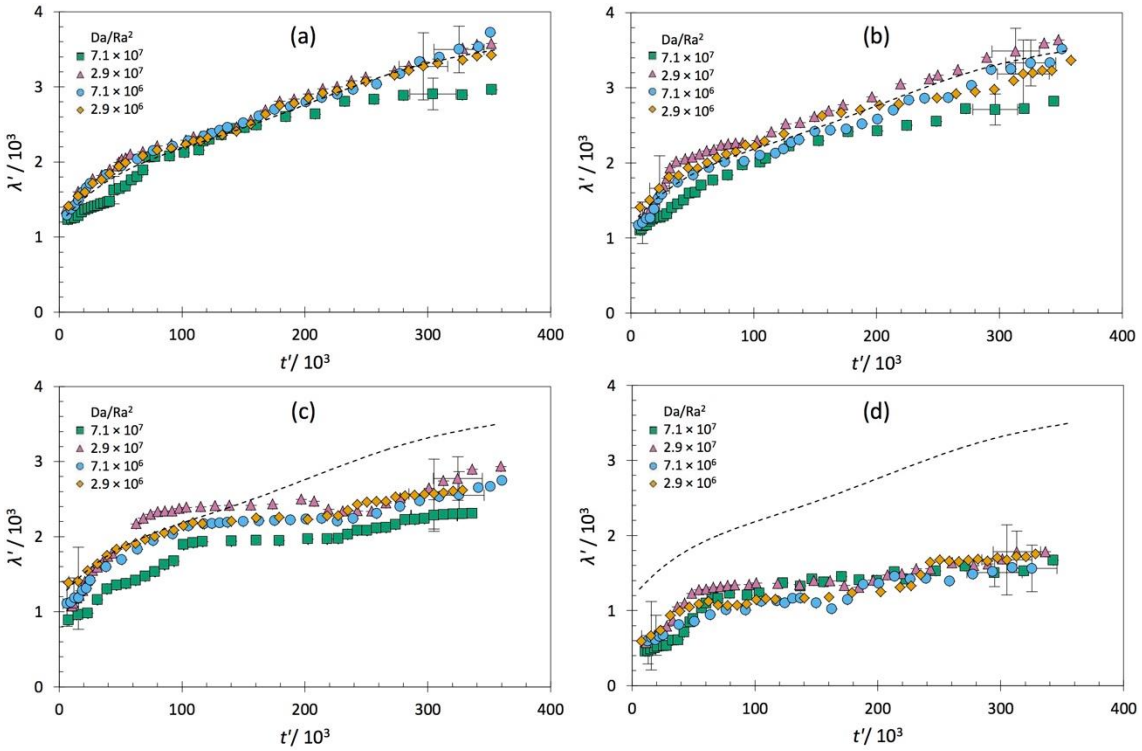

Figure 6.12 Evolution of the dimensionless wavelength of convective fingers λ' for various Da/Ra^2 with: (a) $C_{Bo}' = 10^{-3}$, (b) $C_{Bo}' = 10^{-2}$, (c) $C_{Bo}' = 10^{-1}$ and (d) $C_{Bo}' = 1$. The dashed line represents the average result for the inert case with no reaction ($C_{Bo}' = 0$, $Da/Ra^2 = 0$).

The increase in the dimensionless averaged wavelength of the fingers appears to increase proportional to the square root of dimensionless time initially, and at later stages of the experiment, the increase becomes linear. The slope of the linear regime decreases with increasing C_{Bo}' suggesting that the faster sinking fingers merge more slowly with time.

6.2.3 Time for onset of convection

The dimensionless time for onset of convection t_{oc}' was measured for each of the reactive cases and plotted in Figure 6.13. The cases with $Da/Ra^2 = 2.9 \times 10^7$ and 7.1×10^7 show almost identical results for a given C_{Bo}' and the convection onset was observed at an earlier dimensionless time than for cases with $Da/Ra^2 = 2.9 \times 10^6$ and 7.1×10^6. The same result was obtained for all cases with $Da/Ra^2 = 2.9 \times 10^6$, but it is very likely that fingers developed at an earlier time than shown, especially when $C_{Bo}' = 10^{-1}$ and 1. This is because the dimensionless times for onset of convection for $Da/Ra^2 = 2.9 \times 10^6$ all correspond to a time of 0.2 seconds – the earliest that it was possible for the camera to capture an image. As convective fingers had already formed by the time this

image was taken and there are no earlier images, it was not possible to determine a more accurate time for onset of convection closer to the start of the experiment.

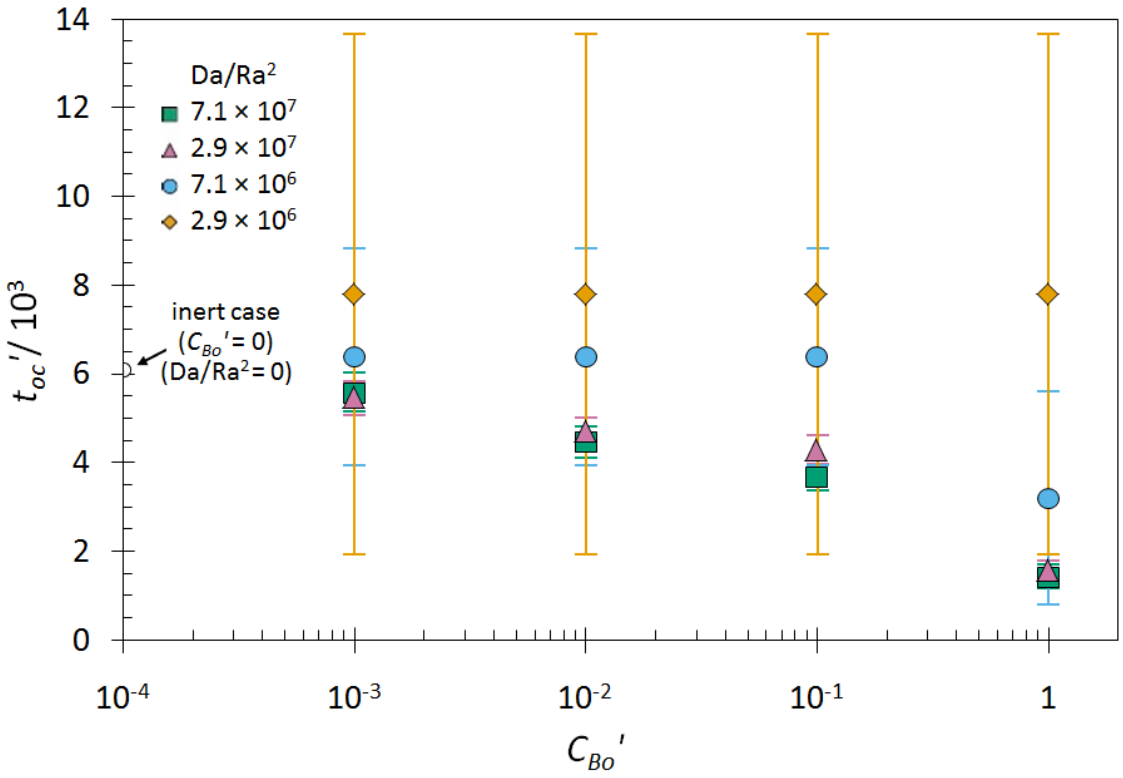

Figure 6.13 The dimensionless time for onset of convection t_{oc}', measured for all reactive cases. The diamond, circle, triangle and square symbols represent results for Da/Ra^2 = 2.9 × 10^6, 7.1 × 10^6, 2.9 × 10^7 and 7.1 × 10^7, respectively.

For cases with Da/Ra^2 = 2.9 × 10^6, the length scale $L_s = \mu D\phi/(k\beta_A C_{As} g)$ = 1.9 × 10^{-7} is small due to the relatively large C_{As} = 1.13 M and h = 1 mm (k = 8.33 × 10^{-8} m^2). The small scaling term means that after nondimensionalisation, there is a big jump in dimensionless time between each recorded image. This is the reason why the error bars in Figure 6.13 are so large and why cases with Da/Ra^2 < 2.9 × 10^6 could not be investigated. Given that the very large error bars for Da/Ra^2 = 2.9 × 10^6 and 7.1 × 10^6 overlap with the results from the cases with Da/Ra^2 = 2.9 × 10^7 and 7.1 × 10^7, it was not possible to confirm whether changes in Da/Ra^2 have any effect on the dimensionless time for onset convection.

6.2.4 Mass flux

Once convection had established in the lower aqueous layer and the system transitioned to the constant mass flux regime for each reactive case, the dimensionless total mass flux of solute *A* was calculated and presented in Figure 6.14. The presence of reaction was found to enhance solute transfer to the domain as the total mass flux of *A* is greater for each of the reactive cases than for the inert case with no reaction, which was represented by the dashed black line in Figure 6.14.

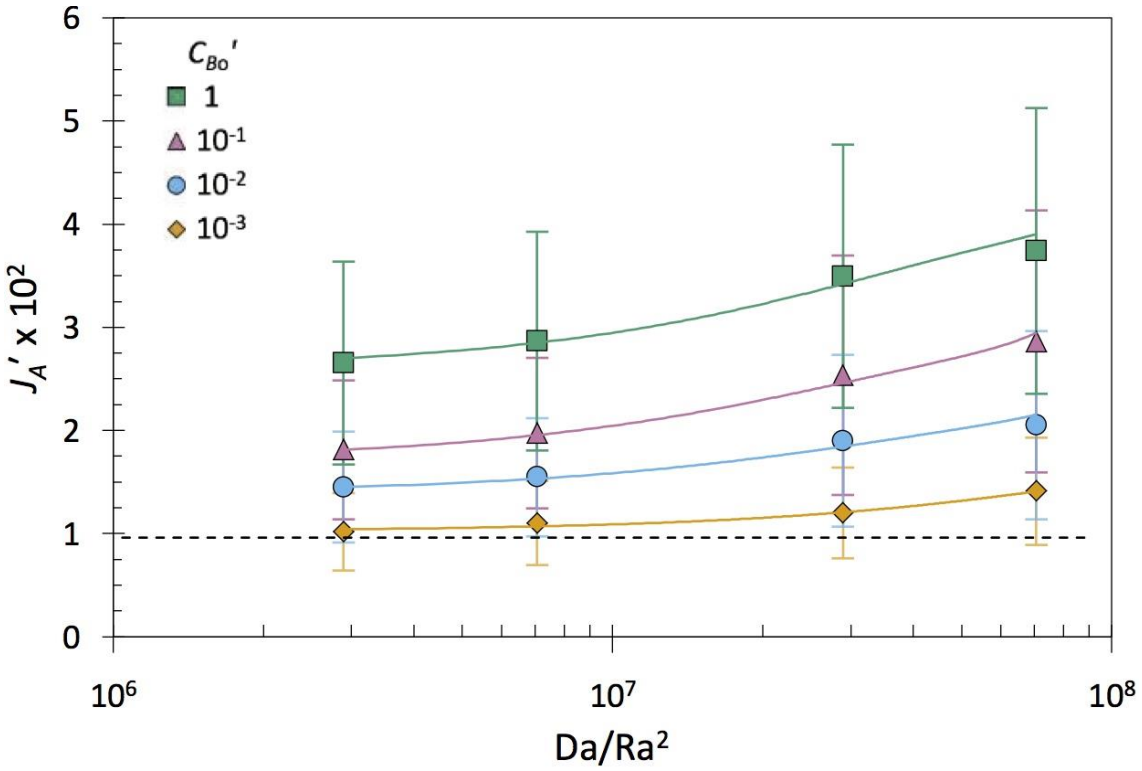

Figure 6.14 Dimensionless steady state total mass flux of solute *A*, during the constant mass flux regime for all reactive cases with various Da/Ra^2 and C_{Bo}'. The dashed line represents the average result for the inert case with no reaction ($C_{Bo}' = 0$, $Da/Ra^2 = 0$).

As the initial concentration of *B* in the aqueous layer was increased from $C_{Bo}' = 10^{-3}$ to $C_{Bo}' = 1$, the dimensionless steady state mass flux was found to increase by 161%, 160%, 192% and 165% for cases with $Da/Ra^2 = 2.9 \times 10^6$, 7.1×10^6, 2.9×10^7 and 7.1×10^7 respectively. The percentage increase for $Da/Ra^2 = 2.9 \times 10^7$ is a little higher than for the other three sets of Da/Ra^2 suggesting that the result with $Da/Ra^2 = 2.9 \times 10^7$ and $C_{Bo}' = 1$ is a slight overestimate. However, the very large error bars due to the error associated with calculating the concentration of solute from the pH of the solution mean that there is uncertainty in the exact values for each result.

It can be argued that the results in Figure 6.14 show that an increase in Da/Ra^2 has an increase on the total mass flux of solute transferred to the lower layer for a given C_{Bo}'. The total flux was found to grow by approximately 40% as Da/Ra^2 was increased from 2.9×10^6 to 7.1×10^7 and the trend is consistent for each set of C_{Bo}'. This increase in total flux could be due to the greater influence of reaction and heavy product formation at higher Da/Ra^2, however it is not possible to confirm whether this is the case as the increase lies within the uncertainty set by the error bars.

6.2.5 Conclusions

Experiments were performed with Da/Ra^2 in the range $2.9 \times 10^6 – 7.1 \times 10^7$. For a given value of Da/Ra^2 similar trends were observed with increasing C_{Bo}' as previously described in section §6.1. For all Da/Ra^2, weakly reactive cases with $C_{Bo}' \leq 10^{-2}$ yielded results akin to the inert case with no reaction and as C_{Bo}' was increased convective fluid motion was enhanced with the effects most pronounced when $C_{Bo}' = 1$.

For a fixed value of C_{Bo}' it was difficult to determine if changes in Da/Ra^2 had a significant effect on the fluid flow as any variations between the results at different Da/Ra^2 were relatively small and within the associated error bars. It is likely that the values of Da/Ra^2 under investigation were in fact too large due to the very fast reaction between acetic acid and ammonia and the system approached the limit where Da/Ra^2 tends to infinity. In order to check whether this was indeed the case, the experimental results were compared to theoretical and numerical work which assumed an instantaneous reaction for this system.

6.3 COMPARISON WITH NUMERICAL SIMULATIONS

The MIBK – acetic acid – aqueous ammonia physicochemical system was modelled numerically by Professor Min Chan Kim, Jeju National University, South Korea using the same initial and boundary conditions as outlined in chapter 3. It was assumed that the chemical reaction in the lower aqueous layer is instantaneous meaning that $Da/Ra^2 \rightarrow \infty$ and that species *A* and *B* cannot coexist. The numerical method is described in detail in the appendix. Linear stability equations were solved analytically and numerically by Professor Kim and the results of the linear analysis were then used as the initial conditions for nonlinear numerical simulations to determine the long-term behaviour of the system.

The flow visualisations from the nonlinear simulations are presented alongside the corresponding images for the experimental cases with $Da/Ra^2 = 7.1 \times 10^7$ in Figure 6.15 to compare the effect of C_{Bo}' on the development of convective instability patterns. Short round regularly-spaced fingers were observed for the cases with $C_{Bo}' \leq 10^{-2}$ in both the experiments and simulations. As C_{Bo}' was increased, convective fingers were found to appear thinner and penetrate deeper into the domain owing to the increase in the amount of heavy product formed by reaction. The similarity in the patterns observed in the experiments and the simulations, where the reaction is assumed to be infinitely fast and $Da/Ra^2 \rightarrow \infty$, suggests that for this experimental system, the reaction between acetic acid and ammonia can be treated as instantaneous and the flow is thus governed only by the initial concentration ratio of reactants.

The results of the numerical work were found to be strongly dependent on the initial perturbation level ε, which was set to 10^{-2} for the simulations presented in Figure 6.15 and could be adjusted to accelerate or retard the onset and growth of the fingers. Therefore the visualisation in Figure 6.15 act only as guide and do not offer direct quantitative measurements of the convective finger characteristics. The reason for the strong dependence of numerical results on the initial perturbation level is most likely due the domain being semi-infinite and therefore unconfined below. The work carried out by Selim and Rees (2007) shows that had the domain been modelled as a finite layer of fixed thickness, it is expected that the ensuing convection would not depend on the nature of perturbation.

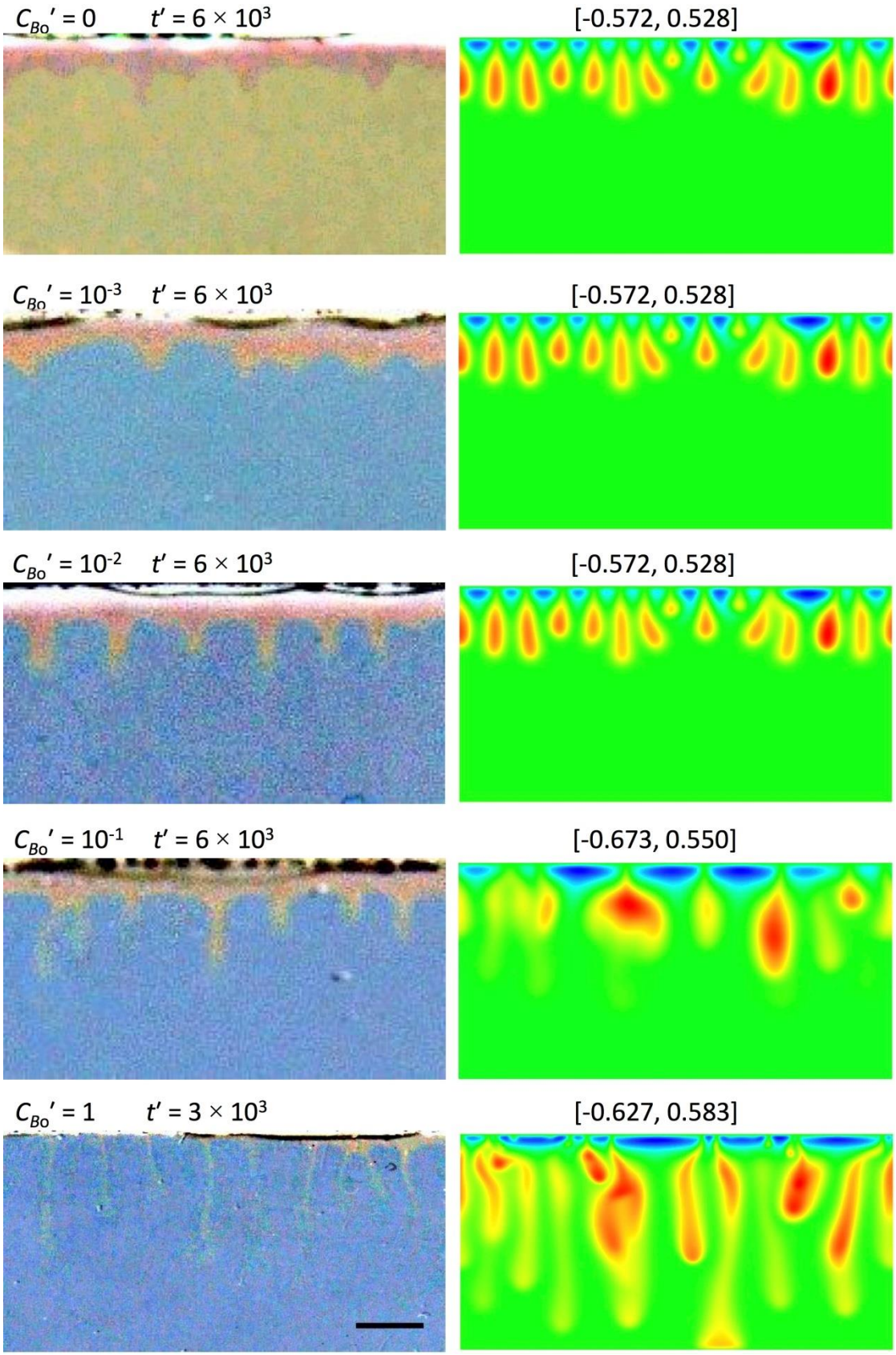

Figure 6.15 Comparison of images from experiments with $Da/Ra^2 = 7.1 \times 10^7$ and nonlinear simulations. The experimental scale bar represents $L' = 10^3$ and the nonlinear domain $[0, L_x'] \times [0, L_z']$ set to $[0, 2 \times 10^3] \times [0, 10^3]$. The numbers in brackets are the minimum (blue) and maximum (red) of the concentration perturbation field, C_{AT1}'.

6.3.1 Time for onset of convection

The neutral stability curves for varying C_{Bo}' were calculated with the initial perturbation level ε set to 10^{-2} and plotted in Figure 6.16(a). The dimensionless critical onset time t_c' (Figure 6.16(b)) and corresponding dimensionless critical wavenumber a_c' (Figure 6.16(c)) were determined by the minimum of the neutral stability curve for each C_{Bo}'. As expected, the onset of instability motion is accelerated as the reactants concentration ratio C_{Bo}' increases. Also, given that the wavenumber is the inverse of the wavelength ($a' = 1/\lambda'$), the initial width of instability motion decreases as C_{Bo}' increases, consistent with the experimental findings presented earlier in this chapter.

The critical onset times obtained from the minimum of the neutral stability curves are more than an order of magnitude smaller than the times determined experimentally. An alternate definition for the onset time is the time at which the dissolution mass flux reaches its minimum t_m' marked by the arrows in Figure 6.17. At this point, the mass flux changes from the diffusive to the convective regime and convection begins to influence the rate of mass transport of solute away from the interface, leading to an increase in the dissolution flux. This implies that the instability motion onset at t_c' is too weak to increase the mass flux significantly, so a longer period of time is necessary during which the instability can grow and for convective effects to be noticeable.

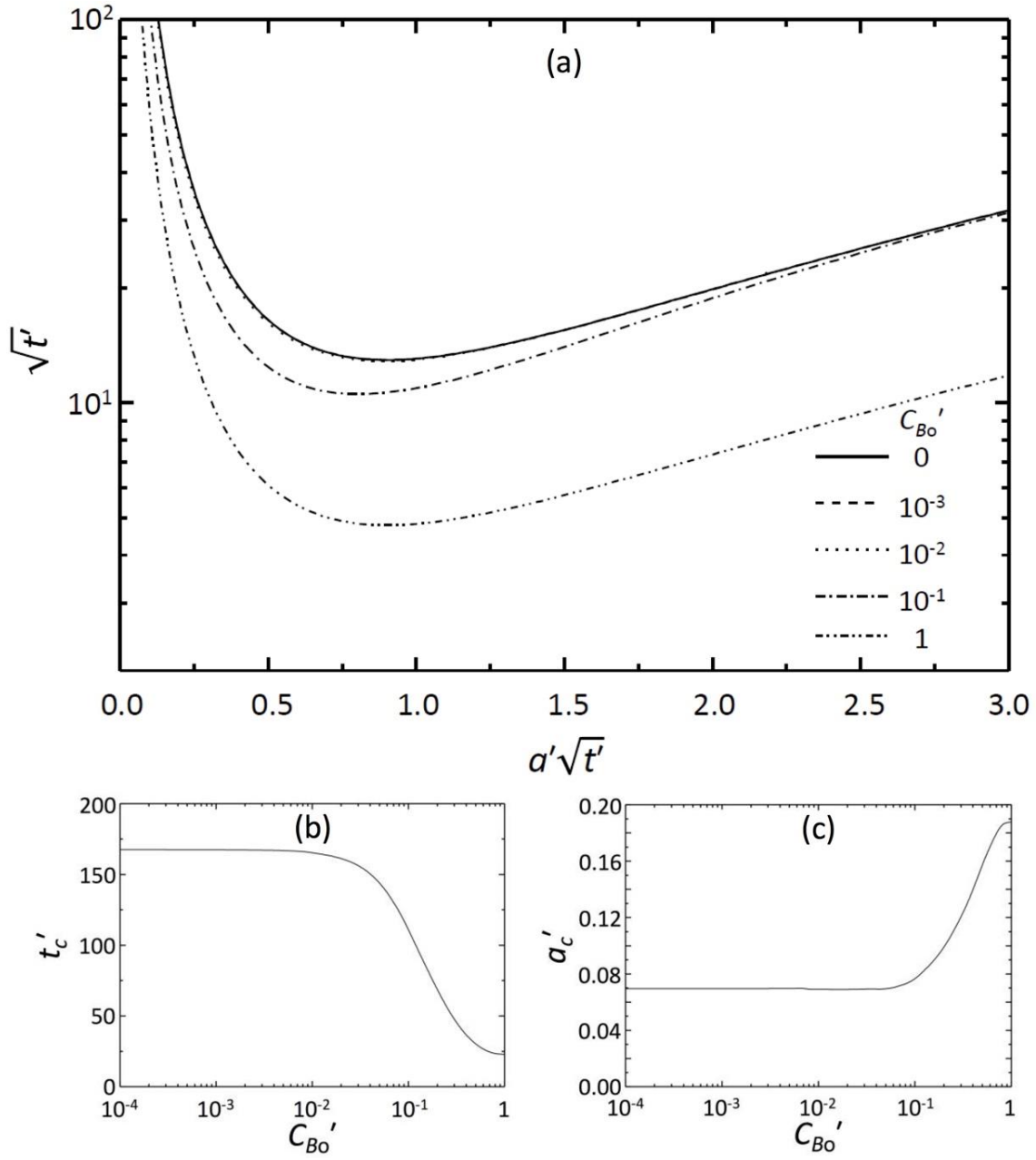

Figure 6.16 (a) Neutral stability curves for various C_{Bo}'. (b) The dimensionless critical onset time t_c' as a function of C_{Bo}'. (c) The dimensionless critical wavenumber a_c' as a function of C_{Bo}'.

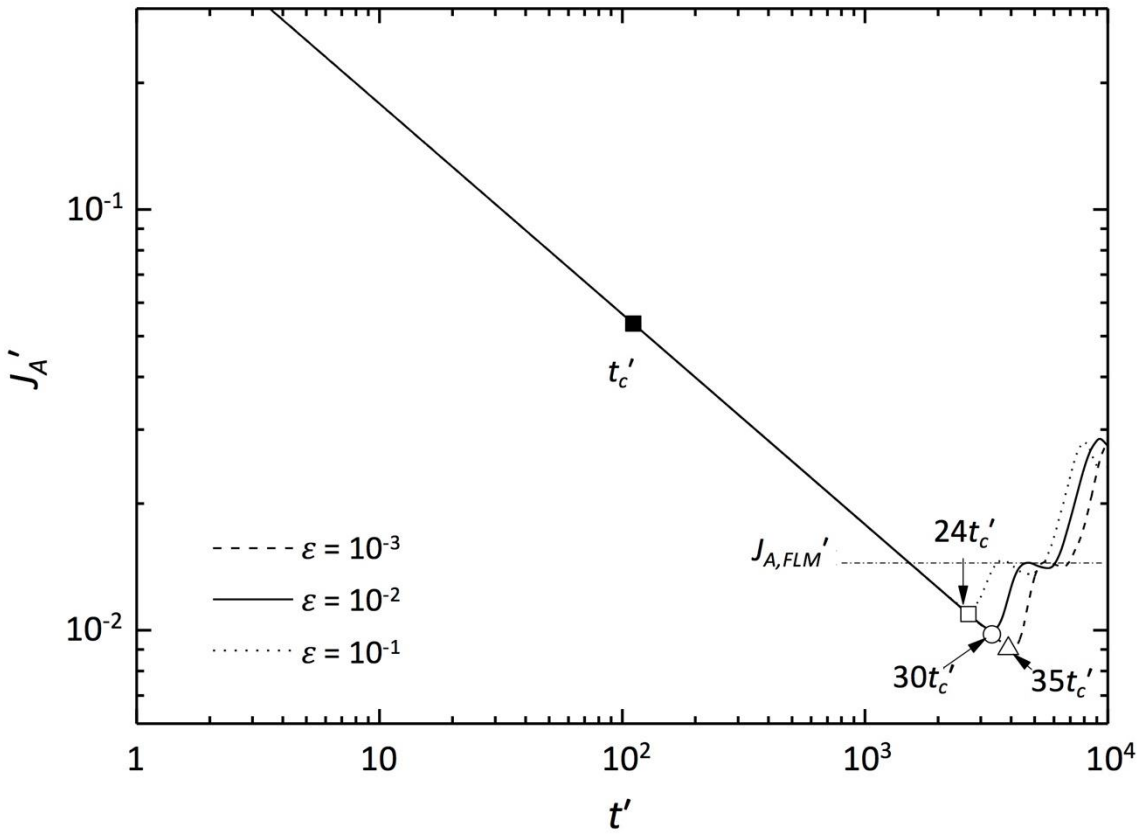

Figure 6.17 Dimensionless total mass flux of solute J_A' as a function of dimensionless time t' for $C_{Bo}' = 10^{-1}$. The black square represents the critical onset time t_c' and the white square, circle and triangle symbols represent the time for total mass flux to reach its minimum t_m', when the initial perturbation level $\varepsilon = 10^{-1}$, 10^{-2} and 10^{-3} respectively. The characteristic first local maximum mass flux $J_{A,FLM}'$, which is discussed in detail in section 6.3.2, is also shown

The results of the numerical simulations are sensitive to the initial perturbation level ε so the time at which the flux reached its minimum was found to vary depending on what the initial perturbation level was set to during the simulation. These lower and upper estimates for the onset time based on the different initial perturbation levels were plotted for different C_{Bo}' in Figure 6.18. It can be seen that for the low C_{Bo}' region, where $C_{Bo}' \leq 10^{-2}$, the numerically determined onset time is nearly independent of C_{Bo}' and as C_{Bo}' is increased to 1, the onset of convection is rapidly accelerated.

The experimental onset times for $Da/Ra^2 = 2.9 \times 10^7$ and 7.1×10^7 are also included in Figure 6.18. The results of experiments with $Da/Ra^2 = 2.9 \times 10^6$ and 7.1×10^6 were not displayed as it was not possible to determine the accurate onset times for these cases as convection had started before the first image could be recorded. Figure 6.18 shows that the onset of convection determined by experiments occurs slightly later than in the

nonlinear simulations, but both sets of results follow a similar trend with increasing C_{Bo}'. The quantitative discrepancy between the experiments and simulations is most likely due to the fact that it was difficult to distinguish early instabilities in experiments. This means that convective fingers would have formed well before they were detected by eye, leading to an overestimation of the onset time. Albeit, it is obvious from Figure 6.18 that the existence of *B* in the aqueous phase accelerates the onset of instabilities.

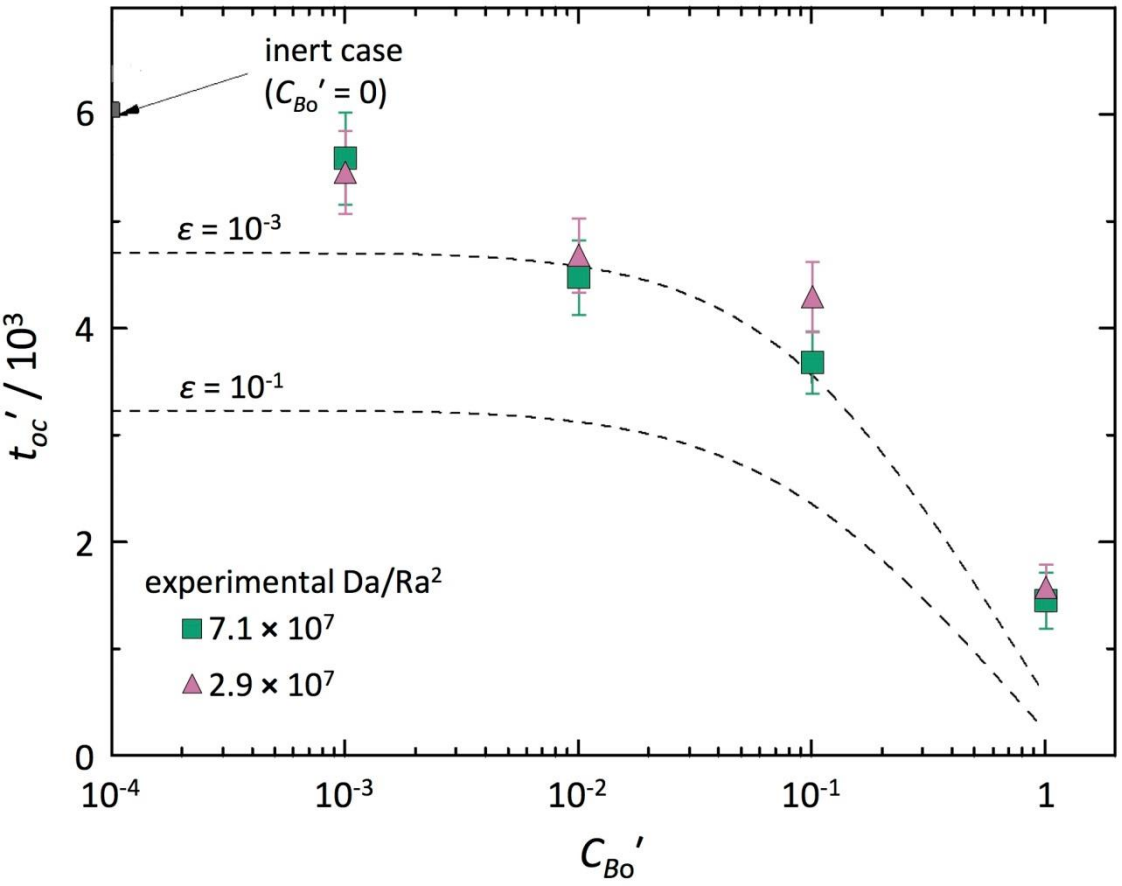

Figure 6.18 Comparison of dimensionless time for onset of convection t_{oc}' obtained from numerical simulations and experiments as a function of C_{Bo}'. The dotted lines represent the onset time from nonlinear simulations with $\varepsilon = 10^{-3}$ and 10^{-1}. The pink triangle and green square symbols correspond to experiments where $Da/Ra^2 = 2.9 \times 10^7$ and 7.1×10^7 respectively. The error bars correspond to a temporal resolution error of ±0.5 s.

6.3.2 Mass flux

The results of the nonlinear numerical simulations for the evolution of total mass flux at the interface shown in Figure 6.17 suggest that there exists a characteristic first local maximum (FLM) dimensionless mass flux $J_{A,FLM}'$. This characteristic flux is almost insensitive to the initial perturbation level, except for the upper limit case where C_{Bo}' = 1, as shown in Figure 6.19(b). The plots in Figure 6.19 show that initially, the flux decays diffusively until it reaches its minimum at which point enough dense solute has accumulated for convection to dominate over diffusion. After the onset of convection, the system enters a flux growth regime where the dissolution flux increases and reaches a maximum value. It can be seen that in Figure 6.19 there is a greater flux of solute and an earlier transition from the diffusive to the convective regime for the case with C_{Bo}' = 1 than for the inert case with no reaction. The oscillations in the mass flux shown in Figure 6.19 are most likely due to the interaction between the recently formed fingers after the onset of convection. Eventually the system would transition to a constant flux regime for each case, however before this could happen, the convection fronts reached the bottom boundary of the calculation domain (L_z' = 10^3). This means that it was not possible to determine a value for the steady state flux from the numerical simulations so the characteristic dimensionless mass flux $J_{A,FLM}'$ was used together with the global maximum mass flux $J_{A,max}'$ for comparison with experiments.

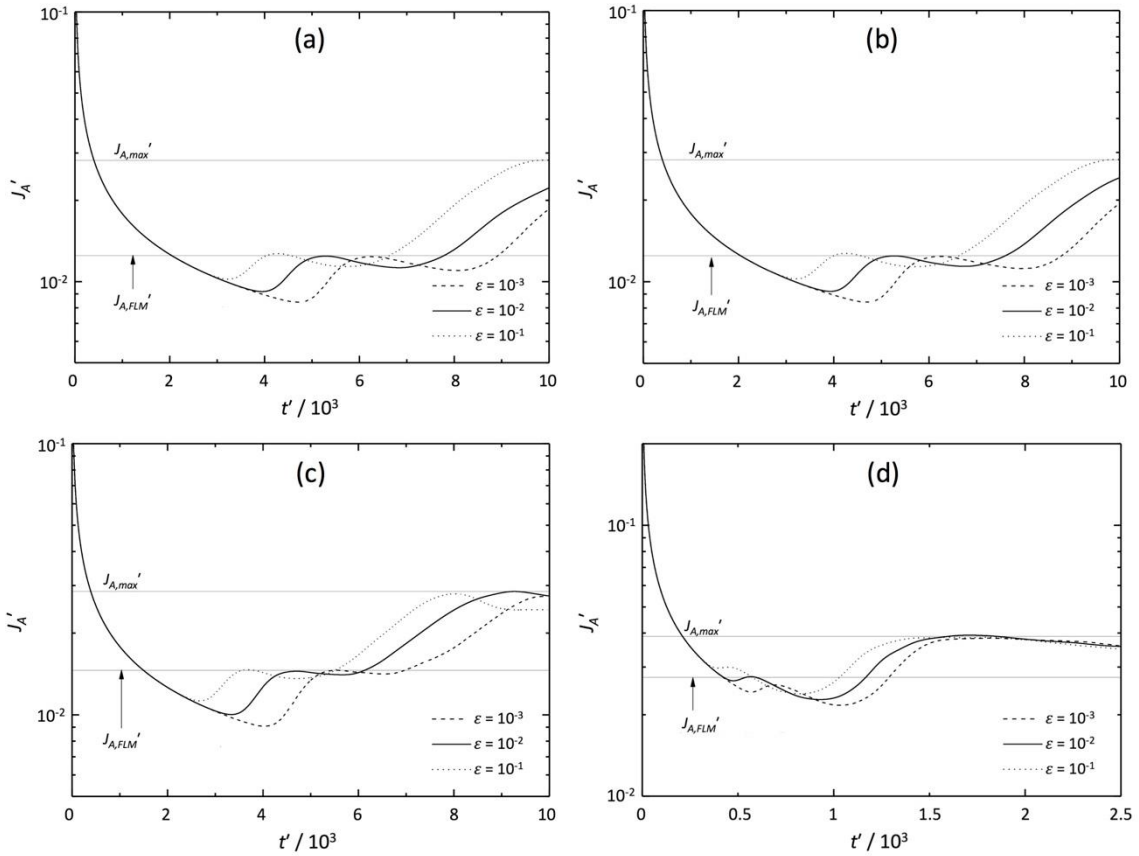

Figure 6.19 Results of nonlinear simulations for the dimensionless total mass flux of solute J_A' as a function of dimensionless time t'. The effect of the initial perturbation level ε on the mass flux is show for the cases with (a) $C_{Bo}' = 0$, (b) $C_{Bo}' = 10^{-2}$, (c) $C_{Bo}' = 10^{-1}$ and (d) $C_{Bo}' = 1$. The characteristic first local maximum mass flux $J_{A,FLM}'$ and the global maximum flux $J_{A,max}'$ are labelled for each case.

The characteristic flux $J_{A,FLM}'$ and the global maximum flux $J_{A,max}'$ from simulations with the initial perturbation level ε set to 10^{-2} were compared to the experimentally determined steady state total mass flux in Figure 6.20. The characteristic flux was found to be approximately constant and equal to 0.0125 for $C_{Bo}' \leq 10^{-2}$ and this would increase to 0.0144 for $C_{Bo}' = 10^{-1}$ and to 0.0275 for $C_{Bo}' = 1$, corresponding to an increase in the rate of total solute uptake of 15% and 120%, respectively, compared to the inert case.

The increase in the mass flux with increasing C_{Bo}' suggests that reaction accelerates convection and increases the transport of solute into the lower layer. Taking into account the experimental error associated with calculating the concentration and thus the mass of solute in the domain, Figure 6.20 shows good agreement between the experiments and the numerical model. The steady state mass flux from experiments falls within the bounds predicted by numerical simulations suggesting that the flux depends on C_{Bo}' and that Da/Ra^2 has a very low effect when it is large.

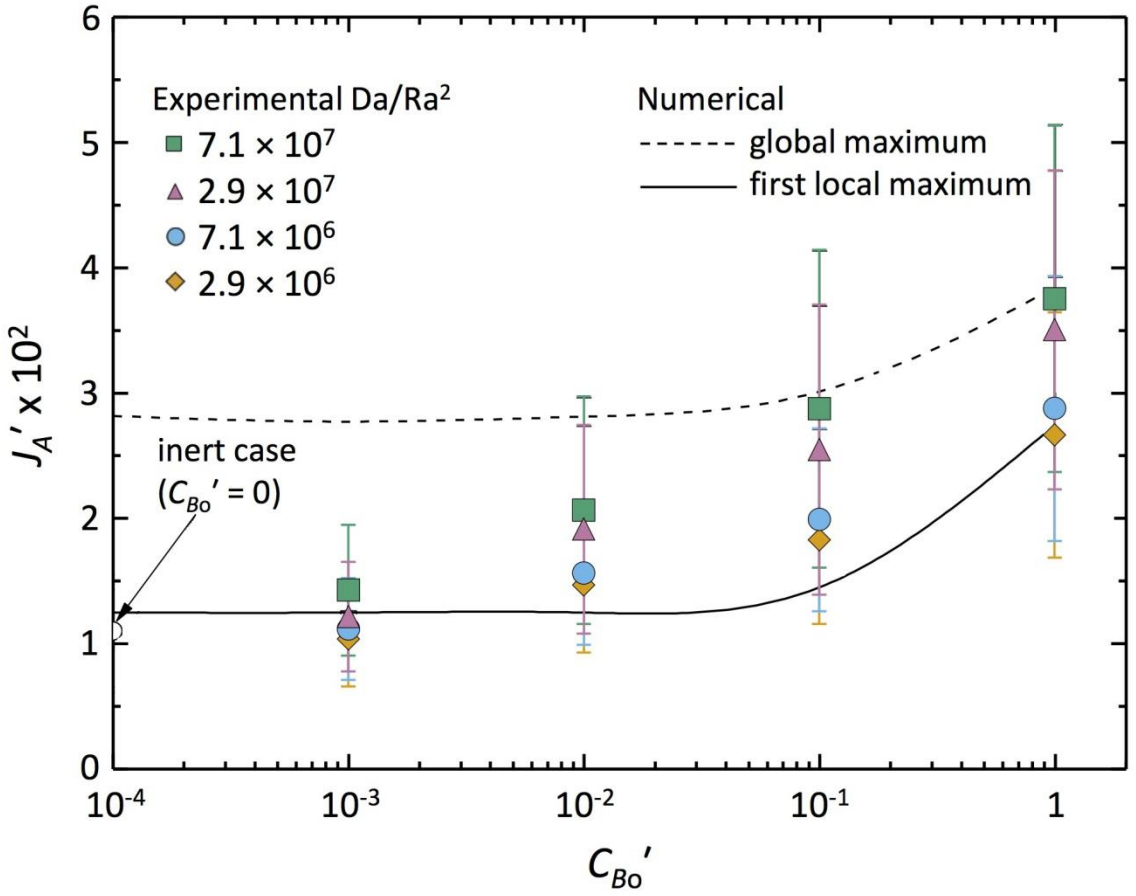

Figure 6.20 Dimensionless total mass flux of solute *A*, J_A', for various C_{Bo}'. The coloured symbols correspond to the steady state mass flux from experiments. The solid line represents the first local maximum mass flux $J_{A,FLM}'$ and the dotted line represents the global maximum flux $J_{A,max}'$ obtained from nonlinear simulations.

6.3.3 Conclusions

Nonlinear numerical simulations of buoyancy-driven flow in a two-layer immiscible system were performed to determine the critical conditions for onset of motion and the rate of dissolution of acetic acid. The effect of instantaneous reaction with aqueous ammonia was investigated and it was found that for $C_{Bo}' \leq 10^{-2}$ the development of flow and convective instability mimicked the inert case with $C_{Bo}' = 0$. As C_{Bo}' was increased from 10^{-2} to 1, more of the dense product of reaction was formed leading to a sharp increase in the dissolution flux, accompanied by a decrease in the time for onset of convection.

The numerical results were shown to have good agreement with the experiments and similar trends were observed with increasing C_{Bo}' for $Da/Ra^2 = 2.9 \times 10^7$ and 7.1×10^7. The agreement between the experimental work and the simulations, where reaction was

assumed to be instantaneous, therefore suggests that the variation in the experimental results for different Da/Ra^2, over the range studied, is insignificant and the rate of reaction is so fast that Da/Ra^2 approaches infinity.

The MIBK – acetic acid – aqueous ammonia physicochemical system was used as an analogue for the flow and reaction of CO_2 in underground porous reservoirs and these results thus demonstrate that chemical reaction can enhance the convective dissolution of CO_2 and optimise the storage capacity of saline aquifers, as discussed in the next chapter.

7 APPLICATION TO CARBON DIOXIDE SEQUESTRATION

The effect of a destabilising chemical reaction on the dissolution of CO_2 in a real world sequestration scenario was investigated in this chapter. The candidate geological formation and chemical reaction are selected and described in section §7.1. The theoretical model from the previous chapter was adapted in section §7.2 to predict the time for onset of convection and the dissolution mass of flux of carbon dioxide in two different geological storage scenarios. Finally, the assumptions made in this analysis are discussed in §7.3.

7.1 CHOICE OF STORAGE SITE AND CHEMICAL REACTION

It has been estimated that there are more than 800 sedimentary formations worldwide that have potential to become sites for industrial-scale CO_2 storage (Bachu, 2003). These sites can be characterised using the Rayleigh number based on their in-situ properties. Given the relatively large values of the Rayleigh number for the MIBK – acetic acid – aqueous ammonia analogue system, storage sites with similarly large Rayleigh numbers were considered to determine the characteristic flow behaviour of CO_2. The Utsira Sand saline aquifer in the Sleipner gas field was chosen as the site for analysis and its properties are outlined in section §7.1.1. The proposed destabilising chemical reaction scheme is described in §7.1.2 and the parameters were chosen to satisfy $3 \times 10^6 \leq \mathrm{Da}/\mathrm{Ra}^2 \leq 7 \times 10^7$, consistent with the range investigated using the experimental system.

7.1.1 Properties of the Sleipner geological formation

The Sleipner gas field in the North Sea is the site of the world's first industrial-scale operation dedicated to the geological storage of CO_2 in a saline formation. The natural gas at Sleipner has approximately 9% CO_2 as an impurity, which is separated from the methane at the surface and then stored underground instead of being released to the atmosphere. During storage, CO_2 is injected into the Utsira Sand saline aquifer at a depth of approximately 1 km below the sea floor, where the temperature is 40^{o}C and the pressure is 10 MPa (Ennis-King and Paterson, 2005). The salinity of the pore water brine within the formation is taken as 1 mol kg^{-1} H_2O (Duan and Sun, 2003). At these conditions the CO_2 solubility is 1 mol kg^{-1} H_2O (Portier and Rochelle, 2005) corresponding to a concentration C_{As} of 1 M and this concentration is assumed to be constant at the upper boundary of the domain. The fluid in the aquifer is initially free of CO_2 and the increase in the fluid density $\Delta\rho$ due to CO_2 dissolution is assumed to be 10 kg m^{-3} (equivalent to 1%). The viscosity of the fluid and the diffusivity of CO_2 were taken to be 5×10^{-4} Pa s and 2×10^{-9} m^2 s^{-1} respectively (Hassanzadeh et al., 2007). The average fluid and geological properties for the Utsira Sand formation are summarised in Table 7.1.

Table 7.1 Average geophysical properties of the Utsira Sand saline aquifer in Sleipner.

Property	Value
Temperature [^{o}C]	40
Pressure [MPa]	10
Domain height, L_z [m]	50
Porosity, ϕ [-]	0.25
Salinity, [mol kg^{-1} H_2O]	1
CO_2 solubility, C_{As} [M]	1
Reference density, ρ_0 [kg m^{-3}]	1000
Density difference, $\Delta\rho$ [kg m^{-3}]	10
Viscosity, μ [Pa s]	5×10^{-4}
Diffusivity, D [m^2 s^{-1}]	2×10^{-9}

The storage reservoir found in Sleipner has an unconsolidated sandstone lithology with a high porosity and permeability. Chadwick et al. (2008) estimated the porosity to vary in the range 20 – 40% and a value of 25% was chosen to be used for the calculations carried out in this chapter. The permeability of the formation is discussed in section §7.1.3, where it is shown that the parameters for this storage site yield high characteristic Rayleigh numbers as desired. Seismic surveys have shown that the thick shale cap rock overlying the aquifer forms an effective seal that prevents CO_2 migration out of the storage formation and leakage to the surface (Torp and Gale, 2004).

7.1.2 Destabilising chemical reaction with sodium hydroxide

Geochemical reactions between CO_2 and the minerals present in the pore water or the formation rock result in the precipitation of solid product. In general, these reactions have slow kinetics (Gunter et al., 1997) and withdraw CO_2 from solution, which in turn stabilises the system and inhibits convection. In order to enhance convection, the product must be soluble and have a greater density than the reactants, so it was therefore necessary to engineer a chemical reaction that does not naturally occur in a saline aquifer.

One potential reaction that fits the desired criteria is the reaction between CO_2 and sodium hydroxide, NaOH. The absorption of CO_2 into an aqueous solution of sodium hydroxide has been well studied due to its industrial importance and involves the following two aqueous phase reactions (Hikita et al., 1976)

$$\mathrm{CO}_{2(aq)} + \mathrm{NaOH}_{(aq)} \rightleftharpoons \mathrm{NaHCO}_{3(aq)} \tag{7.1}$$

$$\mathrm{NaHCO}_{3(aq)} + \mathrm{NaOH}_{(aq)} \rightleftharpoons \mathrm{Na}_2\mathrm{CO}_{3(aq)} \tag{7.2}$$

Reaction (7.1) is irreversible and reaction (7.2) is considered to be instantaneous, thus the overall reaction can be expressed as

$$\mathrm{CO}_{2(aq)} + 2\mathrm{NaOH}_{(aq)} \rightarrow \mathrm{Na}_2\mathrm{CO}_{3(aq)} \tag{7.3}$$

Given that reaction (7.2) is a proton transfer reaction, it has a much larger rate constant than reaction (7.1). The rate limiting step of the overall reaction scheme (3.1) is therefore reaction (7.1) and the overall rate of reaction can be expressed as $k_r[CO_{2(aq)}][NaOH_{(aq)}]$, where $[CO_{2(aq)}]$ and $[NaOH_{(aq)}]$ are molar concentrations of aqueous carbon dioxide and sodium hydroxide respectively. The second-order rate

constant k_r was calculated to equal 2.11 × 10^4 M^{-1} s^{-1} at the conditions present in the Utsira Sand aquifer (Gondal et al., 2015).

To satisfy the $A + 2B \rightarrow C$ stoichiometry, the conservation equations for the dissolved species in this system can be expressed in dimensionless terms as

$$\nabla'^2 C_A' - \mathbf{v}' \cdot \nabla' C_A' = \frac{\partial C_A'}{\partial t'} + \frac{\mathrm{Da}}{\mathrm{Ra}^2} C_A' C_B' \tag{7.4}$$

$$\nabla'^2 C_B' - \mathbf{v}' \cdot \nabla' C_B' = \frac{\partial C_B'}{\partial t'} + \frac{2\mathrm{Da}}{\mathrm{Ra}^2} C_A' C_B' \tag{7.5}$$

$$\nabla'^2 C_C' - \mathbf{v}' \cdot \nabla' C_C' = \frac{\partial C_C'}{\partial t'} - \frac{\mathrm{Da}}{\mathrm{Ra}^2} C_A' C_B' \tag{7.6}$$

The reaction term of Equation (7.4) is multiplied by a factor of two due to the fact that two moles of reactant *B* are consumed for every mole of product *C* formed. The diffusivities of all the species are assumed to be equal and initially (C_A', C_B', C_C') = (0, C_{Bo}', 0) for $z' > 0$ where C_{Bo}' is the initial dimensionless concentration of reactant *B*, sodium hydroxide. At the upper boundary $z' = 0$, the concentration is fixed so that $C_A' + C_C' = 1$ while as $z' \rightarrow \infty$, (C_A', C_B', C_C') → (0, C_{Bo}', 0).

The addition of Equation (7.5) and 2 × Equation (7.6) shows that $C_C' = (C_{Bo}' - C_B')/2$ remains a conserved quantity over time. Using this expression for C_C', the buoyancy contribution due to the concentration of the dissolved species can therefore be rewritten in terms of species *A* and *B*

$$\sum \beta_i' C_i' = \beta_A' C_A' - \left(\frac{\beta_C'}{2} - \beta_B'\right) C_B' + \frac{\beta_C' C_{Bo}'}{2} \tag{7.7}$$

The dimensionless solutal expansion coefficients β_i' (β_i/β_A) for this system can be calculated using the parameters in Table 7.2 to give $\beta_A' = 1$ (Garcia, 2001), $\beta_B' = 4.89$ and $\beta_C' = 12.23$ (Novotny and Sohnel, 1988). These values show that the density profile for this system is unstable and that the formation of product is expected to enhance the density difference driving convection.

Table 7.2 Physicochemical properties of the reactive species.

Parameter	Value
CO_2 solutal expansion coefficient β_A [kg m^{-3} M^{-1}]	8.13
NaOH solutal expansion coefficient β_B [kg m^{-3} M^{-1}]	39.77
Na_2CO_3 solutal expansion coefficient β_C [kg m^{-3} M^{-1}]	99.45
Reaction rate constant k_r [M^{-1} s^{-1}]	2.11×10^4

7.1.3 Summary of the geological sites

Two storage scenarios were considered based on two different values for the permeability of the site. The typical permeability of the porous media in the Utsira Sand formation is approximately 2,000 mD, corresponding to $k \sim 2 \times 10^{-12}$ m^2 (Chadwick et al., 2012), however it has been measured to be as high as 10^{-11} m^2 (Bickle et al., 2007) in certain regions. Using these values together with the fluid and reservoir parameters outlined earlier in this chapter, the length scale $L_s = \mu D\phi/(k\beta_A C_{As} g)$, Rayleigh number $\mathrm{Ra} = k\beta_A C_{As} g L_z/(\mu D\phi)$ and Damköhler number $\mathrm{Da} = k_r C_{As} {L_z}^2/(D\phi)$ were calculated and presented in Table 7.3 for each of the two storage scenarios under consideration.

Table 7.3 Average permeability, length scale and dimensionless groups for two different storage scenarios in the Utsira Sand formation.

	Scenario 1	Scenario 2
k [m^2]	10^{-11}	2×10^{-12}
L_s [m]	2.6×10^{-4}	1.3×10^{-3}
Ra	2.0×10^5	3.9×10^4
Da	1.1×10^{17}	1.1×10^{17}
Da/Ra^2	3×10^6	7×10^7

The high permeability of the aquifer results in a high Rayleigh number where the convective flow is dominant over diffusion for both scenarios and the fast reaction leads to $Da/Ra^2 = 3 \times 10^6$ and 7×10^7 for Scenarios 1 and 2 respectively. These values of Da/Ra^2 are within the range investigated using the MIBK – acetic acid – aqueous ammonia analogue system in the previous chapter where it was shown that for cases with such high Da/Ra^2, the reaction can be treated as instantaneous when modelling the system.

7.2 RESULTS

The model developed by Professor Min Chan Kim, Jeju National University, South Korea, was used to conduct linear stability analysis and nonlinear simulations to determine how the introduction of a chemical reaction with sodium hydroxide affects the flow and storage of CO_2 in the Utsira Sand aquifer. For this system, the upper layer consists of pure CO_2 so that the concentration of CO_2 at the interface for the inert case is equal to its aqueous solubility $C_A = C_{As}$. It has been assumed that the reactive cases conform to the same boundary condition at the interface as outlined in the theory. The initial dimensionless concentration of sodium hydroxide C_{Bo}' in the reservoir formation pore water was varied from 0 – 1 and the inward mass flux of CO_2 solute dissolving at the top boundary of the reservoir domain was calculated for each case. The solute is stored in the aquifer in the form of dissolved CO_2 (A) and the product of reaction (C).

The evolution of the dimensionless total dissolution mass flux J_A' against dimensionless time is shown in **Figure 3.2** where the initial perturbation level ε was set to 10^{-3}, 10^{-2} and 10^{-1} for each C_{Bo}'. The results show that initially the dissolution of solute occurs by molecular diffusion into the formation water until the flux curve reaches its minimum. This point marks the onset of convection where the convective instability is sufficiently strong to dominate over diffusion and therefore becomes the principal solute transport mechanism in the system, resulting in an increase in the mass flux of CO_2.

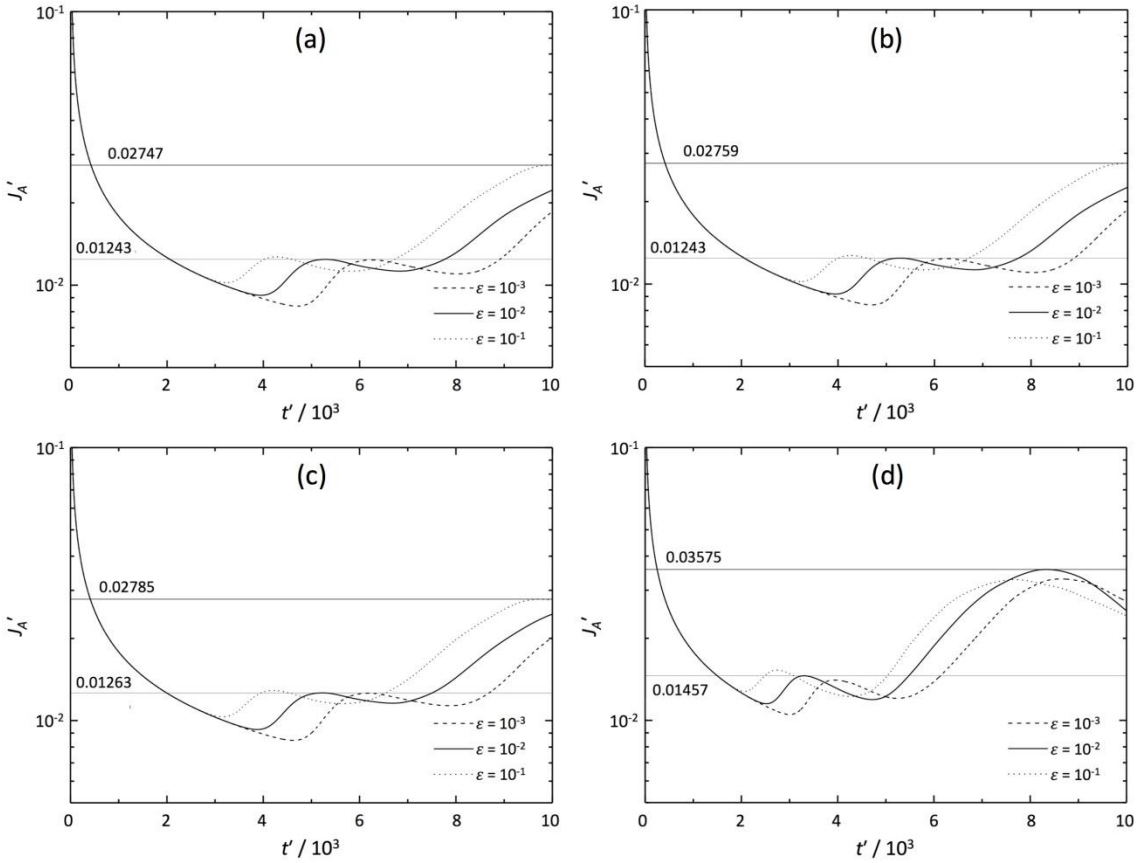

Figure 7.1 Dimensionless total mass flux of solute J_A' as a function of dimensionless time t' for the cases with (a) $C_{Bo}' = 0$, (b) $C_{Bo}' = 10^{-2}$, (c) $C_{Bo}' = 10^{-1}$ and (d) $C_{Bo}' = 1$. The initial perturbation level ε set to 10^{-3}, 10^{-2} and 10^{-1} for each case. The characteristic first local maximum mass flux $J_{A,FLM}'$ and the global maximum flux $J_{A,max}'$ are also labelled.

The minima of the flux curves for $C_{Bo}' = 0$ and 10^{-2} in **Figure 3.2**(a) and (b) appear at approximately the same dimensionless time and as the reactant concentration ratio is then increased to 10^{-1} and 1, an earlier onset time can be observed. **Figure 3.2** also shows that the time at which the minimum of the flux curve occurs depends on the initial perturbation level ε for each case, with an earlier onset for convection recorded as ε is increased from 10^{-3} to 10^{-2} and then to 10^{-1}. The result with $\varepsilon = 10^{-3}$ was therefore taken as the upper bound and $\varepsilon = 10^{-1}$ as the lower bound estimate for the time for onset of convection for each different value of C_{Bo}'. These estimates were plotted in Figure 7.2 and show that for $C_{Bo}' \leq 10^{-2}$, the dimensionless time for onset of convection falls within the range $3.2 \times 10^3 \leq t_{oc}' \leq 4.7 \times 10^3$. As C_{Bo}' is increased to 1, the formation of the denser soluble reaction product creates a greater density difference driving convection and leads to an earlier onset time of $2.1 \times 10^3 \leq t_{oc}' \leq 3.0 \times 10^3$.

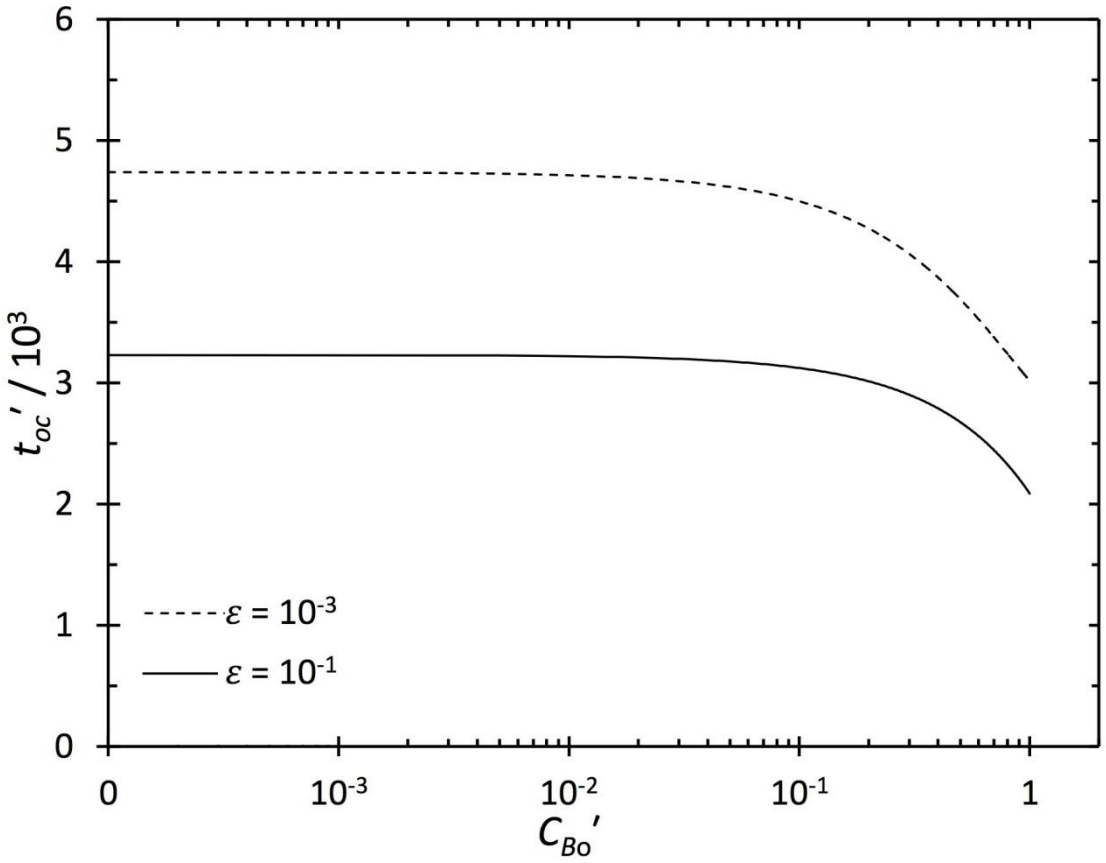

Figure 7.2 Comparison of dimensionless time for onset of convection t_{oc}' as a function of C_{Bo}'. The dotted line provides an upper estimate based on the initial perturbation level $\varepsilon = 10^{-3}$ and the solid line corresponds to the lower estimate with $\varepsilon = 10^{-1}$.

The characteristic first local maximum mass flux and the global maximum flux are also labelled for the curves in **Figure 3.2** to provide an estimate of the mass transfer rate of solute into the reservoir domain. These results were plotted in Figure 7.3 to show that the introduction of sodium hydroxide has little effect on the total solute mass flux for $C_{Bo}' < 10^{-1}$ as it is approximately equal to the dissolution flux of CO_2 into inert brine where $1.2 \times 10^3 \leq J_A' \leq 2.7 \times 10^3$. As the dimensionless concentration of sodium hydroxide is increased to $C_{Bo}' = 1$, there is a sharp increase in the flux and reaction is found to enhance convection and the mass transfer of solute.

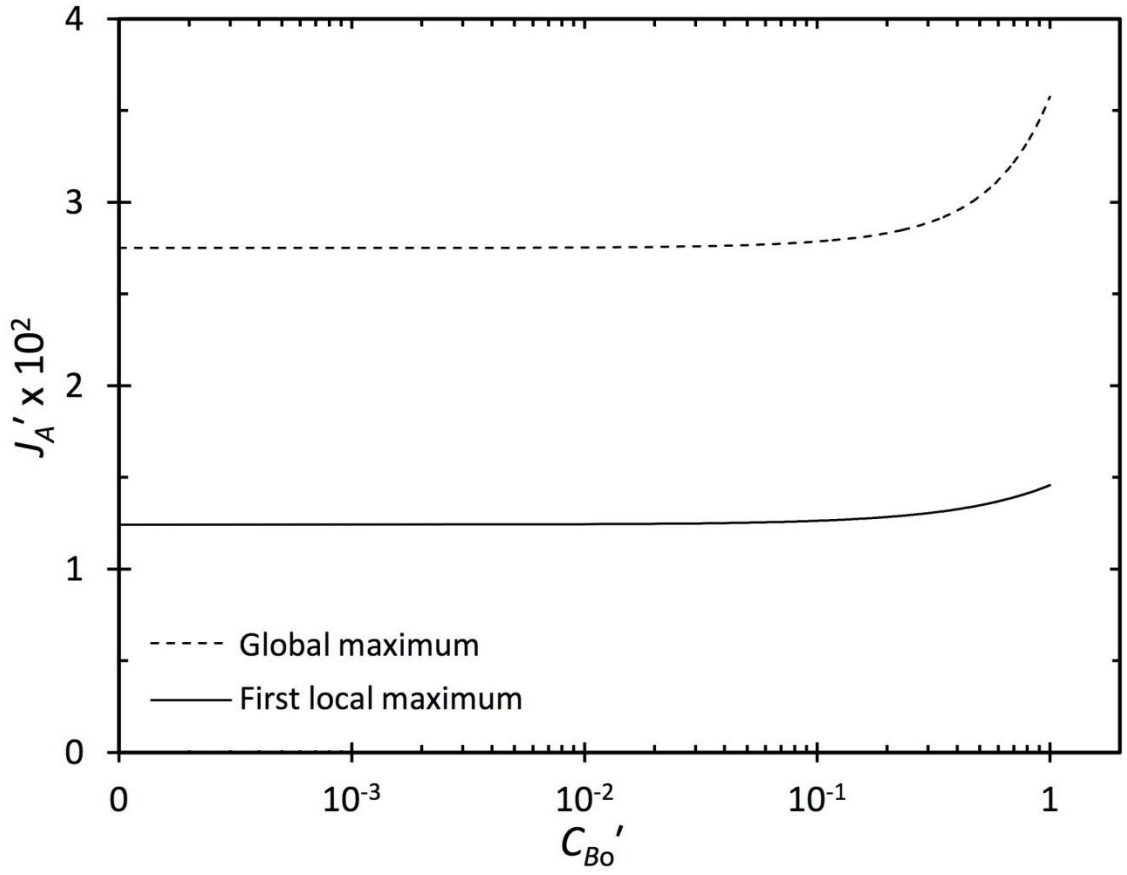

Figure 7.3 Dimensionless total mass flux of CO_2 (solute A), J_A', for various C_{Bo}'. The dotted line corresponds to the global maximum flux $J_{A,max}'$ and the solid line represents the characteristic first local maximum mass flux $J_{A,FLM}'$.

The figures in this section present the results for the time for onset of convection and the total mass flux of CO_2 dissolving into the domain in terms of generalised, dimensionless quantities. In order to calculate the dimensional values for the two proposed storage scenarios in the Utsira Sand saline aquifer, the dimensionless results have been recast using the scales $t_s = L_s^2/D$, $J_s = D\phi C_s/L_s$ and the parameters presented in the tables in the previous section. The dimensional values for the lower and upper bound estimates of the onset time and the inward dissolution flux of CO_2 into the reservoir domain are listed in Table 7.4. The results show that when the initial concentration of sodium hydroxide is greater than 0.1 M, reaction accelerates convection leading to earlier convection onset times and enhanced mass transfer of CO_2. The onset of convection is 36% earlier and the total mass flux of solute increases by 30% when C_{Bo} = 1 M compared to the inert dissolution of CO_2 into brine with no

reaction. An earlier onset time reduces the time available for a potential leak to develop in the reservoir and is therefore crucial in ensuring the storage security of a given site.

Table 7.4 Estimates for the time for onset of convection t_{oc} and the total mass flux of CO_2 into the domain J with varying initial concentration of sodium hydroxide C_{Bo} for storage Scenario 1 ($Da/Ra^2 = 3 \times 10^6$) and Scenario 2 ($Da/Ra^2 = 7 \times 10^7$).

	Scenario 1				**Scenario 2**			
C_{Bo} [M]	t_{oc} [days]		J [kg m^{-2} yr^{-1}]		t_{oc} [days]		J [kg m^{-2} yr^{-1}]	
	lower	upper	lower	upper	lower	upper	lower	upper
0	1.2	1.8	34	75	31	46	6.7	15
10^{-2}	1.2	1.8	34	75	31	45	6.7	15
10^{-1}	1.2	1.7	34	76	30	43	6.8	15
1	0.8	1.1	40	97	20	29	7.8	19

The total mass flux for each storage scenario was calculated to provide an estimate of the amount of CO_2 trapped in terms of kg per m^2 per year. The areal extent of the CO_2 plume interface in Sleipner has been previously approximated as 5.6×10^6 m^2 (Neufeld et al., 2010), corresponding to a maximum total mass flux of 4.2×10^8 kg $yr^{-1}$and 8.3×10^7 kg yr^{-1} for storage Scenarios 1 and 2 respectively without chemical reaction. Table 7.4 suggests that the inward mass flux of CO_2 is lower and convection is delayed for storage Scenario 2 compared to Scenario 1 for all C_{Bo}. This is because the dimensional onset times and total mass flux are a function of the reservoir's permeability, where $t_{oc} = f\ (1/k^2)$ and $J = f\ (k)$, so the increased permeability of Scenario 1 results in a 96% decrease in t_{oc} and a 400% increase in J compared to Scenario 2.

These calculations show that although chemical reaction can enhance convection and reduce the risk of leakage of CO_2 in geological storage sites, the properties of the reservoir, such as its permeability, have to also be carefully considered. This is because selecting highly permeable geological formation as a candidate storage site can have a greater effect on accelerating convection than the introduction of an aqueous chemical reaction to a reservoir domain with a lower permeability.

7.3 ASSUMPTIONS

The numerical model used to simulate the flow of CO_2 is based on a number of assumptions to aid computation. The validity of these assumptions needs to be considered to determine the limitations of the analysis. The porous media of the geological formation has been idealised as two-dimensional, homogenous and isotropic. In reality, the reservoirs are three-dimensional and heterogeneous and this may influence the convective flow of solute. Aquifer heterogeneity leads to increased flow along the areas with higher permeability, increasing the CO_2 storage efficiency in the more permeable zones, while reducing it in where the permeability is low (Bachu, 2015). Even though seismic data and core samples have shown that the Utsira Sand reservoir is relatively homogenous (Chadwick et al., 2008), a storage scenario where the permeability is higher than the average was investigated in this chapter to get an estimate for the effect heterogeneity and increased permeability might have on the evolution of the convective instabilities. If other storage sites with highly heterogeneous porous media need to be investigated, then this model could still be used when considering areas of the formation where there is relative local homogeneity.

Temperature variations have been neglected and the system is modelled under isothermal conditions. In order to determine if these temperature variations are significant enough, the thermal effect on the fluid density difference $\Delta\rho_T$ was calculated where

$$\Delta\rho_T = \rho_0 \beta_T \Delta T \tag{7.8}$$

The thermal expansion coefficient β_T of the pore water at prevailing aquifer conditions varies from 3×10^{-4} K^{-1} to 8×10^{-4} K^{-1} (Javaheri et al., 2009). Taking the larger value for β_T, a temperature change ΔT of 12.5 K is required to cause a density difference of 10 kg m^{-3} – the density difference due to the solutal expansion of CO_2-rich brine. Temperature fluctuations in the reservoir exist due to the geothermal gradient which varies between 20 K km^{-1} and 60 K km^{-1} (Bachu, 2003). Given that the reservoir domain has a typical length of 50 m, the temperature change due to geothermal effects is 0.1 – 0.3 K resulting in a density difference of $\Delta\rho_T$ = 0.08 – 0.24 kg m^{-3}. This density difference due to the temperature variation across the layer is several orders of magnitude smaller than the density increase due to the dissolution of CO_2 and it is therefore safe to assume that the geothermal effects have negligible impact on the dynamics of the flow compared to the solutal concentration effects.

The aqueous concentration of CO_2 in the brine at the top boundary of the domain was calculated based on a number of factors such as the temperature, pressure and salinity of the pore-water. The solubility of CO_2 increases with increasing pressure and decreases with increasing temperature and salinity. In order to investigate the effect of salinity on CO_2 solubility, many previous studies used NaCl solution to represent the aquifer fluid. However, there are often a variety of other ions such as Mg^{2+} and Ca^{2+} present in reality which can affect the amount of CO_2 absorbed in solution (Yasunishi and Yoshida, 1979). These salinity, temperature and pressure effects have all been accounted for by the model developed by Portier and Rochelle (2005) as it has been previously shown to successfully predict the CO_2 solubility in the pore fluid found in the Utsira Sand formation at Sleipner.

It has also been assumed that the presence of sodium hydroxide in the domain does not significantly modify the solubility of CO_2. This is valid for dilute solutions, however for high concentrations of sodium hydroxide, the increase in the ionic strength of the aqueous solution may lead to a decrease in carbon dioxide solubility due to the salting out effect. The solubility of carbon dioxide in an electrolyte solution C_{As}* relative to its aqueous solubility in a pure fluid C_{As} can be estimated using the expression

$$\log\left(\frac{C_{As}\,*}{C_{As}}\right) = -sI \tag{7.9}$$

where s is the salting out parameter which is positive and I is the ionic strength of the solution. The value of s for the solubility of CO_2 gas in aqueous sodium hydroxide is 0.149 $m^3\ kg^{-1}$ at 20°C (Nijsing et al., 1959). Data is not available for supercritical conditions but given that the right hand side of equation (7.9) is negative, it is expected that the solubility of carbon dioxide will decrease as the concentration of sodium hydroxide in the domain is increased. This means that the result for the dimensional mass flux of CO_2 will be a slight overestimate and that the onset of convection will be slightly later than predicted for the case where $C_{Bo}' = 1$.

As more CO_2 is dissolved in the brine, the acidity of the pore water increases due to the dissociation of carbonic acid. This can initiate a series of geochemical reactions between the acidified brine and the formation rock that may result in the dissolution of alkaline earth elements and the subsequent precipitation of calcite (Rosenbauer et al., 2005). These reactions with the formation rock are kinetically very slow, taking at least in the order of tens to hundreds of years (Gunter et al., 1997). Given that the geochemical reactions occur over much longer time scales, they can be ignored and it is

possible to only consider the convection of solute and chemical reaction with sodium hydroxide as the main mechanisms for CO_2 sequestration in the short to medium term for the system investigated in this chapter. If the long term effects are deemed to be of interest and the additional dissolution of minerals occurs leading to precipitation of solute, then this mineral trapping is beneficial as it further enhances the storage capacity and security of the reservoir. The precipitation of minerals is expected to increase the rock volume and thus reduce the porosity of the formation with time. However, this effect is counter balanced by the reduction in rock volume during the dissolution of rock minerals, which increases the porosity of the porous media (Xu et al., 2004). These variations in porosity are ignored in this work due to the very long time scales required for mineral trapping to occur.

The introduction of sodium hydroxide to the reservoir pore water means that after reaction with CO_2, a dense soluble product is formed that sinks deep into the formation resulting in a larger extent of the reservoir over which the CO_2 spreads. The reaction with sodium hydroxide helps enhance the amount of CO_2 stored in the aquifer and minimise the possibility of CO_2 leakage to the surface, however it also brings about its own engineering and economic difficulties. There will be significant costs associated with the injection of sodium hydroxide into the reservoir and ensuring that it is evenly distributed within the pore water. These challenges will most likely make such a reaction very difficult to implement in practice, but it was used in this chapter to show how the dissolution and convection of CO_2 can be enhanced by chemical reaction. The analysis has shown that careful selection of a storage site with a high permeability can accelerate the flow of CO_2 by a greater extent than the introduction of a complex chemical reaction.

The analysis carried out in this chapter has relied on numerical modelling to determine the characteristic measurements for the dissolution of CO_2 in the Utsira Sand saline aquifer in Sleipner. It is clear that there are many challenges in using mathematical models to accurately predict the fate of injected CO_2. The systems modelled numerically are idealised and incorporating considerations for the nonuniformities and complexities that exist in reality is computationally much more demanding. Despite the assumptions and simplifications, numerical models used in conjunction with experimental observations are important as they provide useful estimates that help with the large-scale implementation of CO_2 storage in saline aquifers. The results of this chapter act as an illustrative example of how the geological properties of different

reservoirs have to be taken into account in order to assess the storage potential of a site and this in turn may help with the selection of future sites for the injection of CO_2.

8 CONCLUSIONS AND SUGGESTIONS FOR FUTURE WORK

The conclusions drawn from the experimental and numerical work modelling the destabilising effect of a fast chemical reaction on the dissolution of carbon dioxide in saline aquifers are summarised in section §8.1. The extensions of this analysis and suggestions for future work are also given in section §8.2.

8.1 CONCLUSIONS

The effects of climate change observed over the last century are attributed to the increase in the atmospheric concentration of greenhouse gases, in particular carbon dioxide. Geological sequestration of CO_2 in deep saline aquifers is a way to reduce emissions into the atmosphere and therefore mitigate climate change. Before large-scale industrial CO_2 storage projects are implemented on a global scale, it is necessary to understand the CO_2 trapping mechanisms to help predict the final fate of the injected CO_2. Both solubility and mineral trapping are deemed favourable as they increase the storage potential of an aquifer and reduce the amount of free supercritical CO_2 which may leak out to the atmosphere through cracks in the cap rock.

The coupled effects of convection and a second-order chemical reaction on the dissolution of supercritical CO_2 and the resulting fluid flow were characterised in this work using a theoretical model. After nondimensionalisation, the system was found to

be governed by the initial dimensionless concentration of the reactant in the aqueous phase C_{Bo}', the solutal expansion coefficients of the reactant and the product of reaction, and the dimensionless parameter Da/Ra^2. The effects of these parameters on the flow and transport of solute into the aqueous reservoir domain were analysed experimentally using a laboratory-scale physicochemical system. The experimental system consisted of an organic solution of acetic acid dissolved in MIBK, overlying an immiscible aqueous solution inside a vertically-orientated Hele-Shaw cell. The diffusion of acetic acid across the horizontal interface and into the aqueous layer resulted in the formation of buoyancy-driven instabilities, mimicking the dissolution of CO_2 in brine, with a pH indicator used to visualise the fluid flow. The development of the flow was recorded using a digital camera and the image files were then processed using a series of calibrated steps to relate the intensity of each pixel to the pH of the solution, and then the solution pH to the concentration of the dissolved species. The experimental results were quantitatively compared to previous work to validate the experimental system as a suitable analogue to model the convective dissolution of supercritical CO_2 in an aquifer.

The effect of chemical reaction was investigated by dissolving ammonia of known concentration in the aqueous layer. The aqueous product of reaction has a greater density than the reactants meaning that the chemical reaction has a destabilising effect on the system. The initial dimensionless concentration of ammonia was varied in the range $C_{Bo}' = 0 - 1$ and it was found that at low C_{Bo}' the fingers are rich in solute and reaction has little effect on the development of convective instability for $C_{Bo}' \leq 10^{-2}$. As the dimensionless concentration of ammonia was increased to $C_{Bo}' = 10^{-1}$, more of the heavy aqueous product was formed, increasing the dissolution flux of solute and the convective fingers were observed to grow at a faster rate and with a smaller wavelength compared to the inert case with no reaction. The effect of chemical reaction and dense product formation was most pronounced for the case where the initial reactant concentration ratio approaches its stoichiometric value, $C_{Bo}' = 1$, resulting in an increase in the dissolution flux of up to approximately 300%. The concentration of acetic acid and the cell gap width were also varied to investigate the effect of changing the Da/Ra^2 parameter in the range $2.9 \times 10^6 - 7.1 \times 10^7$. The results showed little variation between the cases under investigation as any discrepancies were relatively small and within the associated errors.

The physicochemical system was modelled numerically to measure the effect of the initial dimensionless concentration of ammonia on the time for onset of convection and

the mass flux of solute into the aqueous layer. As C_{Bo}' was increased above 10^{-2}, instabilities were observed to form at an earlier time, accelerating the rate of mass transport of solute into the lower layer and the convective fingers were found to appear thinner and penetrate deeper into the domain owing to the increase in the amount of heavy product formed by reaction. The agreement between the experimental work and the numerical simulations, where reaction was assumed to be instantaneous, suggests that the aqueous phase reaction between acetic acid and ammonia is so fast that Da/Ra^2 tends to infinity and the flow is therefore only governed by C_{Bo}', consistent with experimental observations.

The results show that the formation of a dense aqueous product by chemical reaction can enhance convection and, in the context of CO_2 storage, indicate that it is necessary to analyse the composition and reactivity of the aquifer pore water to ensure the selection of the optimum storage sites. The storage formation in Sleipner, with two different reservoir permeabilities, was considered as an illustrative example to demonstrate the effect that the introduction of aqueous sodium hydroxide into the domain fluid may have on the dissolution of CO_2 into the reservoir brine. The product of reaction does not precipitate out of solution as it has a high solubility and its relatively high density means that the formation of product has a destabilising effect on the system. The results of numerical simulations show that the dimensionless onset of convection is accelerated by 36% and the dimensionless total mass flux of dissolved CO_2 increases by 30% when the sodium hydroxide concentration is stoichiometric with the solubility of CO_2 at the aqueous interface, compared to the results for the inert dissolution of CO_2 into brine with no reaction. The results for the two storage scenarios were converted to dimensional quantities and it was found that the difference in permeability between the two storage scenarios has a far greater effect on the timescales and rate of convective motion than the introduction of sodium hydroxide to the system. This type of analysis is therefore of great value during the initial screening of saline aquifer formations and the selection of suitable storage sites for large-scale CO_2 sequestration projects. Further work is required to obtain more accurate estimates for understanding the long-term fate of geologically stored CO_2 and to develop models that are able to incorporate more of the real world complexities that are present in storage formations but are currently ignored.

8.2 SUGGESTIONS FOR FUTURE WORK

The experimental work carried out in this study was able to provide important insights into the effect of a density increasing chemical reaction on the flow and transport of solute inside a two-layer immiscible system. However, further work is recommended to extend the range of parameters investigated and also improve the experimental apparatus.

A list of the common experimental problems experienced in the laboratory was given in chapter 4 along with their causes. Extra care has to continue to be taken when setting up the apparatus to minimise the possibility of the cells leaking or bubbles forming when the upper cell is lowered to start each experimental run. The bubbles were found to accumulate inside the cell due to the fact that the top of the upper cell is sealed and there are no vents for the bubbles to escape through. If vents are incorporated into the design then an alternative method of filling the upper cell is required, as the liquid would otherwise flow out of the upper cell when the rig is horizontally orientated during the filling stage.

Another improvement would be to change the way in which the upper cell is lowered to make contact with the lower cell in order to start each experimental run. This was done manually by sliding the upper cell downwards as steadily as possible, however it was often difficult to do so without imparting some vertical momentum perturbations to the interface and thus affecting the development of the early instabilities. This could be solved by installing a rotating screw jack to act as a controlled mechanism with which to lower the upper cell in a slow and uniform manner.

The borosilicate glass plates that were used to make up the lower and upper cell were all of slightly different dimensions. These differences come about from the machining process and make it very difficult to ensure that the plates and the cell gaps are perfectly aligned. The inevitable wear and tear also resulted in the surface of the glass being scratched. It is therefore necessary to order new plates, manufactured to a high degree of accuracy so that they have identical dimensions. Having more plates would also increase the number of experiments that can be completed during each session in the laboratory as this is currently limited by having to thoroughly clean and soak the plates after each run. However, if new glass plates are used in the future, the image colour to pH conversion would have to be recalibrated as the pixel intensity may be dependent on the thickness of the plates inside the cell.

The current visualisation technique, which uses a pH colour indicator, provides a non-intrusive way to study the complex of transport of multiple aqueous species in porous media, but requires further refinement. A deeper investigation into the optimum concentration and combination of different pH indicators would help improve the sensitivity of the colorimetric pH measurement. Some of the measurement errors and limitations in resolution were also due to the noise in the images. Although the lighting equipment was set up to provide as close to uniform illumination of the cell domain as possible, there was still some noise present in the images even after processing. To eliminate the remaining noise, future experiments should be conducted in a dark room so that any external light interference and possible reflections are avoided.

The contours of the fingers observed in the experiments are isocurves specific to the particular pH colour indicator chosen to visualise the system. Although care was taken to make sure that the mixture of indicators used during the experiments matched the pH transition zones of the chemical species, it is recommended to confirm that the full extent of the convective fingers is tracked by using an optical Schlieren technique. Such a visualisation technique is sensitive to changes in the refractive index generated by density gradients and can thus detect flow. If the observed convective patterns are the same for the two different visualisation techniques, it is then safe to rule out the possibility that the presence of the indicator in the solution affects the development of the hydrodynamics. Particle image velocimetry could also be used to fully capture velocity field and thus improve the understanding of the flow, however this creates additional challenges in the assembly and cleaning stages due to the presence of the fine tracer particles in the fluid.

Experiments could not be carried out over a wider range of values of Da/Ra^2 for this system due to the limitation in the time interval between images recorded by the digital camera. Using an ultra-fast camera that is able to shoot at a higher frame rate would address the issue of not being able to accurately capture the development of the fluid flow at early times. Additionally, a wider range of cell gap widths should also be investigated. A smaller gap width would lead to slower experiments and thus make it easier to use the current recording equipment to obtain a better insight into the early behaviour of the system and the formation of convective instabilities.

It would be of interest to perform more experiments where the initial dimensionless concentration of ammonia is in the range $C_{Bo}' = 10^{-1} - 1$ as this was the range over which the formation of product had the most pronounced effect. Experimental data points in this range would help build even more confidence in the agreement with the results of the numerical simulation.

The theoretical model in chapter 3 identified that along with the dimensionless parameters Da/Ra^2 and C_{Bo}', the flow in the system is also governed by the values for the solutal expansion coefficient of the reactant and product. Therefore, the study should be extended to determine the influence of these coefficients by exploring a different physicochemical system experimentally. The new physicochemical system would require for the chemical reaction between the solute and reactant species to also be instantaneous so that the current numerical model could still be used. Alternatively, investigating a chemical reaction with slower kinetics would make it possible to experimentally quantify the effect of Da/Ra^2, which could not be done using the current system. The physicochemical properties have been assumed to be constant because the solutions are dilute and the diffusivities of the different chemical species are similar (Weast, Astle and Beyer, 1979). If a different system is investigated, the effects of concentration on the viscosity and diffusivity need to be considered as it may be necessary to extend the study to account for any differential diffusion effects on the stability of the system.

The quantification of experimental observations was carried out using automated computational methods, when possible, in order to reduce human error in measurements. The depth of the convective fingers and their wavelength was calculated from the respective transverse and longitudinal averaged concentration profiles. However, the time for onset of convection was determined by eye. In the numerical simulations, the onset time was calculated by tracking the evolution of mass flux. Unfortunately, the experimental flux measurement is not currently sensitive enough to identify the transition from the diffusive flux regime to the convective one when convection dominates over diffusive mass transfer effects.

During numerical simulations, the convective fingers would reach the bottom boundary before the solute mass transfer rate could reach a steady state value. The depth of the numerical domain should therefore be increased so that the simulations can run for longer and therefore the sufficient amount of time can elapse for the system to enter the steady state flux regime. This could not be done during this study and would increase

the computational time for each simulation, however it would be a worthwhile future endeavour.

The chemical reaction between CO_2 and sodium hydroxide was introduced in chapter 7 to demonstrate how a very fast second-order reaction can enhance the dissolution and convection of CO_2 in geological formations. It was not possible to find an existing geochemical reaction between CO_2 and the naturally occurring reactive species that satisfies the reactive scenario investigated in this work. Further research into the geochemistry between CO_2 and the chemical species native to deep underground saline aquifers may lead to finding a suitable reaction, however if no such reactions can be identified then the numerical model and the experimental analogue system should be adapted to most closely match the destabilising scenario that can be observed in nature. It is also worth bearing mind that the real reaction is likely to be far more complex than the second-order scheme used in the present models.

Knowledge of reservoir properties such as porosity and permeability is required to quantify the potential storage capacity and rates of dissolution. These properties vary significantly between geological formations and within individual sites themselves, so further research into the confidence in the reported values may facilitate better estimates of the CO_2 trapping timescales. Sensitivity studies should be performed to factor in a given error in the known values of each property to show which is likely to have the biggest effect during the implementation of large-scale geological storage project.

The porous media in this work has been considered as a two-dimensional idealised system. However, this is a simplification of reality and these idealisations may lead to errors when the results are applied to a real geological storage scenario. All natural rock formations are heterogeneous at some scale and the the effect of heterogeneity on the flow and trapping mechanisms of CO_2 should therefore be accounted for by the models. The direct numerical simulations should also be extended to three-dimensions in order to obtain more realistic estimates of the long-term dissolution rate. Modelling in three dimensions would have to take into account additional degrees of freedom and may therefore increase the complexity of the hydrodynamic patterns.

Factoring in the quantitative effect of the considerations discussed above is beyond the scope of this work and they are unlikely to have a significant qualitative impact on the findings. However, it is worth calculating their relative effect on the development of the flow in order to improve the overall understanding of the influence of each of the

different parameters on the system and ensure the long-term safety of the sequestered CO_2.

Aside from the application to the storage of CO_2, the present work's experimental and numerical results also help the general understanding of the coupled effect of chemical reaction on convective fingering. The occurrence of these phenomena in miscible fluids is of interest to several other engineering applications and the existing apparatus and numerical model could therefore be adapted to study miscible systems where the upper and lower layers are both aqueous solutions.

APPENDIX

The numerical model used to simulate the MIBK – acetic acid – aqueous ammonia physiochemical system in chapter 6 is described in detail here. The model is based on the one used previously by Kim and Choi (2015), but this time uses the boundary conditions set out in chapter 3. The stability characteristics are identified theoretically and then using the theoretical results as a start point, the nonlinear buoyancy-driven motion is analysed by solving the nonlinear governing equations numerically.

A.1 LINEAR STABILITY EQUATIONS

Using the expressions for the total dimensionless concentration of the species derived from solute *A*, $C_{AT}' = C_A' + C_C'$, and the total dimensionless concentration of the species derived from reactant *B*, $C_{BT}' = C_B' + C_C'$, the conservation equations governing the system outlined in chapter 3 can be rewritten as

$$\frac{\partial C_{AT}'}{\partial t'} + \mathbf{v}' \cdot \nabla' C_{AT}' = \nabla'^2 C_{AT}' \tag{A.1}$$

$$\frac{\partial C_{BT}'}{\partial t'} + \mathbf{v}' \cdot \nabla' C_{BT}' = \nabla'^2 C_{BT}' \tag{A.2}$$

The reaction is instantaneous so solute *A* and reactant *B* cannot coexist. It is therefore assumed that there is a reaction front z_R', such that for $z' \leq z_R'$, $C_B' = 0$ and the velocity profile can be written as

$$\mathbf{v}' = -\nabla' p' + \{C_{AT}' + (\beta_C' - 1) C_{BT}'\}\mathbf{i}\,, \text{ for } z' \leq z_R' \tag{A.3}$$

Also, for $z' \geq z'_R$, where solute A is totally depleted and $C_A' = 0$

$$\mathbf{v}' = -\nabla' p' + \{\beta_B' C_{BT}' + (\beta_C' - \beta_B') C_{AT}'\}\mathbf{i}\,, \text{ for } z' \geq z_R' \tag{A.4}$$

The initial and boundary conditions for equations (A.1) – (A.4) are

$$C_{AT}' = 0,\ C_{BT}' = C_{Bo}' \text{ and } \mathbf{v}' = 0, \text{ at } t' = 0 \text{ and } z' > 0 \tag{A.5}$$

$$C_{AT}' = 1,\ C_{BT}' = C_{Bo}' \text{ and } \mathbf{v}' = 0, \text{ at } t' > 0 \text{ and } z' = 0 \tag{A.6}$$

$$C_{AT}' = 0,\ C_{BT}' = C_{Bo}' \text{ and } \mathbf{v}' = 0, \text{ at } t' > 0 \text{ and } z' \to \infty \tag{A.7}$$

All of the terms used in this appendix are nondimensional and the superscript (′) is left out from this point on to aid clarity.

The velocity and concentration are decomposed into the base state and perturbation components. Given the base state concentration solution $C_{BTb} = C_{Bo}$, it is possible to linearise the equations above to obtain the following linear stability equations:

$$\nabla^2 w_1 = \nabla_1^2\{C_{AT1} + (\beta_C - 1)C_{BT1}\}\,, \text{ for } z \leq z_R \tag{A.8}$$

$$\nabla^2 w_1 = \nabla_1^2\{\beta_B C_{BT1} + (\beta_C - \beta_B)C_{AT1}\}\,, \text{ for } z \geq z_R \tag{A.9}$$

$$\frac{\partial C_{AT1}}{\partial t} + w_1 \frac{\partial C_{ATb}}{\partial z} = \nabla^2 C_{AT1} \tag{A.10}$$

$$\frac{\partial C_{BT1}}{\partial t} = \nabla^2 C_{BT1} \tag{A.11}$$

$$C_{AT1} = C_{BT1} = w_1 = 0 \text{ at } z = 0 \tag{A.12}$$

$$C_{AT1} \to 0,\ C_{BT1} \to 0 \text{ and } w_1 \to 0 \text{ as } z \to \infty \tag{A.13}$$

where w_1 is the vertical velocity perturbation, $\nabla_1^2 \left(= \partial^2 / \partial x^2\right)$ is the horizontal Laplacian operator, C_{AT1} and C_{BT1} are the concentration perturbations of solute A and reactant B derived species respectively. Through the Fourier mode analysis, i.e., $\nabla_1^2 f(t,x,z) = -a^2 \bar{f}(t,z)$ where a is the horizontal wavenumber, the above equations are reduced to

$$\left(\frac{\partial^2}{\partial z^2} - a^2\right)\bar{w}_1 = -a^2\{\bar{C}_{AT1} + (\beta_C - 1)\bar{C}_{BT1}\}\,, \text{ for } z \leq z_R \tag{A.14}$$

$$\left(\frac{\partial^2}{\partial z^2} - a^2\right)\bar{w}_1 = -a^2\{\beta_B \bar{C}_{BT1} + (\beta_C - \beta_B)\bar{C}_{AT1}\}\,, \text{ for } z \geq z_R \tag{A.15}$$

$$\frac{\partial \bar{C}_{AT1}}{\partial t} + \bar{w}_1 \frac{\partial C_{ATb}}{\partial z} = \left(\frac{\partial^2}{\partial z^2} - a^2\right)\bar{C}_{AT1} \tag{A.16}$$

$$\frac{\partial \bar{C}_{BT1}}{\partial t} = \left(\frac{\partial^2}{\partial z^2} - a^2\right)\bar{C}_{BT1} \tag{A.17}$$

From now, for the purpose of simplicity, the bars (¯) will also be removed.

As discussed by the previous studies (Pramanik and Mishra, 2014; Pritchard, 2009; Riaz et al., 2005), the perturbations which are localised near the reaction front cannot be accurately captured in the (*t*,*z*)-domain, since the dominant operator, $\partial^2/\partial z^2$ does not have localised eigenfunctions that vanish at the infinite boundaries. Equations (A.12) – (A.17) can therefore be reformulated in the self-similar (*t*,*ζ*)-domain as

$$\left(\frac{\partial^2}{\partial\zeta^2} - a^2 t\right) w_1 = -a^2 t\{C_{AT1} + (\beta_C - 1)C_{BT1}\}, \text{ for } \zeta \le \zeta_R \tag{A.18}$$

$$\left(\frac{\partial^2}{\partial\zeta^2} - a^2 t\right) w_1 = -a^2 t\{\beta_B C_{BT1} + (\beta_C - \beta_B)C_{AT1}\}, \text{ for } \zeta \ge \zeta_R \tag{A.19}$$

$$t\frac{\partial C_{AT1}}{\partial t} = \left(\frac{\partial^2}{\partial\zeta^2} + \frac{\zeta}{2}\frac{\partial}{\partial\zeta} - a^2 t\right) C_{AT1} - \sqrt{t} w_1 \frac{1}{\sqrt{\pi}} \exp\left(-\frac{\zeta^2}{4}\right) \tag{A.20}$$

$$t\frac{\partial C_{BT1}}{\partial t} = \left(\frac{\partial^2}{\partial\zeta^2} + \frac{\zeta}{2}\frac{\partial}{\partial\zeta} - a^2 t\right) C_{BT1} \tag{A.21}$$

$$C_{AT1} = C_{BT1} = w_1 = 0 \text{ at } \zeta = 0 \tag{A.22}$$

$$C_{AT1} \to 0,\ C_{BT1} \to 0 \text{ and } w_1 \to 0 \text{ as } \zeta \to \infty \tag{A.23}$$

It should be kept in mind that equations (A.12) – (A.17) and equations (A.18) – (A.23) are mathematically equivalent except for the singular limit of $t = 0$.

A.2 ANALYTICAL SOLUTION

Following the analysis carried out by Kim and Choi (2015), the concentration perturbation fields can be expressed as

$$C_{AT1} = \sum_{n=1}^{\infty} A_n(t)\kappa_n \varphi_n(\zeta) \text{ and } C_{BT1} = \sum_{n=1}^{\infty} B_n(t)\kappa_n \varphi_n(\zeta) \tag{A.24}$$

$$\varphi_n(\zeta) = H_{2n-1}\left(\frac{\zeta}{2}\right)\exp\left(-\frac{\zeta^2}{4}\right) \text{ for n = 1, 2, 3, …} \tag{A.25}$$

$$\left(\frac{\partial^2}{\partial\zeta^2} + \frac{\zeta}{2}\frac{\partial}{\partial\zeta}\right)\varphi_n = -n\varphi_n \text{ for n = 1, 2, 3, …} \tag{A.26}$$

where $H_k(\xi)\left\{= (-1)^k \exp\left(\xi^2\right)\frac{d^k}{d\xi^k}\exp\left(-\xi^2\right)\right\}$ is the k-th Hermite polynomial. The scale factor $\kappa_n = \left\{2^{n-1/2}\pi^{1/4}\sqrt{\Gamma(2n)}\right\}^{-1}$ is inserted to guarantee the orthonormal relation. Here, φ_n and $-n$ are the eigenfunction and the eigenvalue of the Sturm-Liouville

equation (A.26), respectively. From equation (A.21) and equations (A.24) – (A.26) it is possible to obtain

$$\frac{\partial B_n}{\partial t} = -\left(\frac{n}{t} + a^2\right) B_n \tag{A.27}$$

which suggests that the perturbation C_{BT1} is always a decaying one and therefore, the most unstable perturbation is $C_{BT1} = 0$. Based on this, the stability equations (A.18) – (A.23) can be further simplified as

$$\left(\frac{\partial^2}{\partial \zeta^2} - a^2 t\right) w_1 = -a^2 t C_{AT1}\ ,\ \text{for } \zeta \leq \zeta_R \tag{A.28}$$

$$\left(\frac{\partial^2}{\partial \zeta^2} - a^2 t\right) w_1 = -a^2 t(\beta_C - \beta_B) C_{AT1}\ ,\ \text{for } \zeta \geq \zeta_R \tag{A.29}$$

$$t\frac{\partial C_{AT1}}{\partial t} = \left(\frac{\partial^2}{\partial \zeta^2} + \frac{\zeta}{2}\frac{\partial}{\partial \zeta} - a^2 t\right) C_{AT1} - \sqrt{t} w_1 \frac{1}{\sqrt{\pi}} \exp\left(-\frac{\zeta^2}{4}\right) \tag{A.30}$$

Letting

$$w_1{}^* = \sum_{n=1}^{\infty} A_n(t) \kappa_n \chi_n(a^2 t \zeta) \tag{A.31}$$

the following equations can be obtained

$$\left(\frac{\partial^2}{\partial \zeta^2} - a^2 t\right) \chi_n^- = -a^2 t \varphi_n\ ,\ \text{for } \zeta \leq \zeta_R \tag{A.32}$$

$$\left(\frac{\partial^2}{\partial \zeta^2} - a^2 t\right) \chi_n^+ = -a^2 t(\beta_C - \beta_B) \varphi_n\ ,\ \text{for } \zeta \geq \zeta_R \tag{A.33}$$

The superscripts (–) and (+) correspond to the solutions inside ($\zeta \leq \zeta_R$) and outside ($\zeta \geq \zeta_R$) the reaction front, respectively. Given that velocity and stress are continuous, $\chi_n^- = \chi_n^+$ and $(\chi_n^-/\partial\zeta) = (\chi_n^+/\partial\zeta)$ should be satisfied at $\zeta = \zeta_R$.

Using the variation of parameters, the solutions of equations (A.32) and (A.33) are obtained as

$$\begin{aligned}\chi_n^- = a^* \sinh(a^*\zeta) &\int_0^\infty \exp(-a^*\xi)\varphi_n d\xi \\ &+\frac{a^*}{2}\exp(-a^*\zeta)\int_0^\zeta \exp(a^*\xi)\varphi_n d\xi \\ &-\frac{a^*}{2}\exp(a^*\zeta)\int_0^\zeta \exp(-a^*\xi)\varphi_n d\xi \\ &+ a^*\sinh(a^*\zeta)\,(\beta_C-\beta_B-1)\int_{\zeta_R}^\infty \exp(-a^*\xi)\varphi_n d\xi\end{aligned} \tag{A.34}$$

and

$$\begin{aligned}\chi_n^+ = a^* \sinh(a^*\zeta) &\int_0^\infty \exp(-a^*\xi)\varphi_n d\xi \\ &+\frac{a^*}{2}\exp(-a^*\zeta)\int_0^\zeta \exp(a^*\xi)\varphi_n d\xi \\ &-\frac{a^*}{2}\exp(a^*\zeta)\int_0^\zeta \exp(-a^*\xi)\varphi_n d\xi \\ &+ a^*\sinh(a^*\zeta)\,(\beta_C-\beta_B-1)\int_{\zeta_R}^\zeta \exp(-a^*\xi)\varphi_n d\xi \\ &-\frac{a^*}{2}\exp(a^*\zeta)\,(\beta_C-\beta_B-1)\int_{\zeta_R}^\zeta \exp(-a^*\xi)\varphi_n d\xi\end{aligned} \tag{A.35}$$

Here, $a^* = a\sqrt{t}$. By performing the integration by parts, the following recursive relations can be reached

$$\begin{aligned}&\chi_n^- = \\ &4a^{*2}(\chi_{n-1}^- - 4\varphi_{n-1}) + \\ &a^*\sinh(a^*\zeta)\,(\beta_C-\beta_B-1)\begin{Bmatrix} 2\exp\left(-\frac{\zeta_R^2}{4}-a^*\zeta_R\right)H_{2n-2}\left(\frac{\zeta_R}{2}\right) \\ -4a^*\exp\left(-\frac{\zeta_R^2}{4}-a^*\zeta_R\right)H_{2n-3}\left(\frac{\zeta_R}{2}\right)\end{Bmatrix}\end{aligned} \tag{A.36}$$

and

$$\chi_n^+ = 4a^{*2}(\chi_{n-1}^+ - 4\varphi_{n-1}) - 4a^{*2}(\beta_C - \beta_B - 1)\varphi_{n-1} + a^*\exp(-a^*\zeta)(\beta_C - \beta_B - 1)\left\{2\exp\left(-\frac{\zeta_R^2}{4}\right)H_{2n-2}\left(\frac{\zeta_R}{2}\right)\sinh(a^*\zeta_R) + 4a^*\exp\left(-\frac{\zeta_R^2}{4}\right)H_{2n-3}\left(\frac{\zeta_R}{2}\right)\cosh(a^*\zeta_R)\right\} \quad \text{(A.37)}$$

with

$$\chi_1^- = a^{*2}\sqrt{\pi}\exp(a^{*2})\left[\exp(-a^*\zeta)\left\{\mathrm{erf}\left(\frac{\zeta}{2} - a^*\right)\right\} + \exp(a^*\zeta)\left\{\mathrm{erf}\left(\frac{\zeta}{2} + a^*\right)\right\} - 2\sinh(a^*\zeta)\right] + a^*\sinh(a^*\zeta)\,(\beta_C - \beta_B - 1)\left[2\exp\left(-\frac{\zeta_R^2}{4} - a^*\zeta_R\right) - 2\,a^*\sqrt{\pi}\exp(a^{*2})\left\{1 - \mathrm{erf}\left(\frac{\zeta_R}{2} + a^*\right)\right\}\right] \quad \text{(A.38)}$$

and

$$\chi_1^+ = a^{*2}\sqrt{\pi}\exp(a^{*2})\left[\exp(-a^*\zeta)\left\{\mathrm{erf}\left(\frac{\zeta}{2} - a^*\right)\right\} + \exp(a^*\zeta)\left\{\mathrm{erf}\left(\frac{\zeta}{2} + a^*\right)\right\} - 2\sinh(a^*\zeta) - 2\sinh(a^*\zeta)\,(\beta_C - \beta_B - 1)\left\{1 - \mathrm{erf}\left(\frac{\zeta_R}{2} + a^*\right)\right\} + (\beta_C - \beta_B - 1)\exp(a^*\zeta)\left\{\mathrm{erf}\left(\frac{\zeta}{2} + a^*\right) - \mathrm{erf}\left(\frac{\zeta_R}{2} + a^*\right)\right\} + (\beta_C - \beta_B - 1)\exp(-a^*\zeta)\left\{\mathrm{erf}\left(\frac{\zeta}{2} - a^*\right) - \mathrm{erf}\left(\frac{\zeta_R}{2} - a^*\right)\right\}\right] + 2a^*\sinh(a^*\zeta)\,(\beta_C - \beta_B - 1)\exp\left(-\frac{\zeta_R^2}{4} - a^*\zeta_R\right) + a^*(\beta_C - \beta_B - 1)\left\{\exp(-a^*\zeta)\exp\left(-\frac{\zeta_R^2}{4} + a^*\zeta_R\right) - \exp(a^*\zeta)\exp\left(-\frac{\zeta_R^2}{4} - a^*\zeta_R\right)\right\} \quad \text{(A.39)}$$

Substituting C_{AT1} and w_1 into equation (A.30) and performing the weighted integration for the whole domain, the following relation is obtained

$$t\sum_{m=1}^{\infty}\frac{dA_m}{dt}\int_0^{\infty}\kappa_m\,\varphi_m\kappa_n\varphi_n\exp\left(\frac{\zeta^2}{4}\right)d\zeta$$

$$=\sum_{m=1}^{\infty}A_m(-m-a^2t)\int_0^{\infty}\kappa_m\,\varphi_m\kappa_n\varphi_n\exp\left(\frac{\zeta^2}{4}\right)d\zeta \qquad \text{(A.40)}$$

$$-\frac{1}{\sqrt{\pi}}\sqrt{t}\exp\left(\frac{\zeta^2}{4}\right)\sum_{m=1}^{\infty}A_m\int_0^{\infty}\kappa_m\,\chi_m\kappa_n\varphi_n\exp\left(\frac{\zeta^2}{4}\right)d\zeta$$

Here $\exp(\zeta^2/4)$ is the weighting function of the operator $\left\{\partial^2/\partial\zeta^2+(\zeta/2)\partial/\partial\zeta\right\}$. Using the orthonormal relation $\int_0^{\infty}\kappa_m\,\varphi_m\kappa_n\varphi_n\exp\left(\frac{\zeta^2}{4}\right)d\zeta=\delta_{m,n}$, the stability equations are reduced to the following matrix form

$$t\frac{d\mathbf{a}}{dt}=\mathbf{E}\mathbf{a} \qquad \text{(A.41)}$$

where

$$E_{mn}=(-m+a^2t)\delta_{m,n}+\frac{1}{\sqrt{\pi}}\sqrt{t}\kappa_m\kappa_n\int_0^{\infty}\varphi_m(\zeta)\chi_n(\zeta)d\zeta \qquad \text{(A.42)}$$

$$\mathbf{a}=[A_1,A_2,A_3,\ldots]^T \qquad \text{(A.43)}$$

for m, n = 1, 2, 3. It is stressed that the partial differential equations (A.28) – (A.30) are reduced into the simultaneous ordinary differential equations (A.41) – (A.43), without spatial discretisation. Furthermore, the characteristic matrix **E** is real and symmetric, i.e., $\mathbf{E}=\mathbf{E}^T$, since $\int_0^{\infty}\varphi_m(\zeta)\chi_n(\zeta)d\zeta=\int_0^{\infty}\varphi_n(\zeta)\chi_m(\zeta)d\zeta$ and therefore the following normal mode expression is possible

$$\sigma t\mathbf{a}=\mathbf{E}\mathbf{a} \qquad \text{(A.44)}$$

The above equation means that the growth factor of perturbation, σt, and the corresponding perturbation are determined by the maximum eigenvalue of the characteristic matrix **E** and its eigenvector. Furthermore, overstability is not a concern since all the eigenvalues of the symmetric matrix are real.

For the case where $t \ll 1$, the following 1-term approximation, which has been previously called the dominant mode analysis (DMA) (Riaz et al., 2005), is valid

$$\sigma t = -(1 + a^2 t) + \frac{1}{\sqrt{\pi}} \sqrt{t} \kappa_1^2 \int_0^\infty \varphi_1(\zeta) \chi_1(\zeta) d\zeta \tag{A.45}$$

Also, for the extreme case where $t \to 0$, the maximum growth rate and the least stable perturbation are determined as

$$\sigma t \to -1 \text{ and } C_{AT1}(t, \zeta) = A_1(t) \kappa_1 \chi_1(\zeta) \text{as } t \to 0 \tag{A.46}$$

This means that the present system is initially stable, since the least stable perturbation has a large negative growth rate.

A.3 NUMERICAL SHOOTING SOLUTION

Under the Quasi-Steady State Approximation (QSSA), equations (A.18) – (A.21) can be reduced as

$$(D^2 - a^2 t) w_1 = -a^2 t \{C_{AT1} + (\beta_C - 1) C_{BT1}\}, \text{ for } \zeta \leq \zeta_R \tag{A.47}$$

$$(D^2 - a^2 t) w_1 = -a^2 t \{\beta_B C_{BT1} + (\beta_C - \beta_B) C_{AT1}\}, \text{ for } \zeta \geq \zeta_R \tag{A.48}$$

$$\sigma t C_{AT1} = \left(D^2 + \frac{\zeta}{2} D - a^2 t\right) C_{AT1} - \sqrt{t} w_1 \frac{1}{\sqrt{\pi}} \exp\left(-\frac{\zeta^2}{4}\right) \tag{A.49}$$

$$\sigma t C_{BT1} = \left(D^2 + \frac{\zeta}{2} D - a^2 t\right) C_{BT1} \tag{A.50}$$

Where $D = d/d\zeta$. The boundary conditions for these equations are the same as those given in equations (A.22) – (A.23). The stability equations (A.47) – (A.50) were solved by employing the outward shooting scheme (Straughan, 2004). In order to integrate these stability equations the appropriate values of Dw_1, DC_{AT1} and DC_{BT1} at $\zeta = 0$ should be assigned for a given t and a. Since the stability equations and their boundary conditions are all homogeneous, the values of $Dw_1(0)$ can be given arbitrarily and the values of $\sqrt{t}$ are assumed under the neutral stability condition, $\sigma = 0$. After the initialization this eigenvalue problem can be solved numerically by following the method previously outlined by Kim and Choi (2012).

As shown in Figure A.1, for the MIBK – acetic acid – aqueous ammonia system where the initial dimensionless concentration of ammonia in the lower layer $C_{Bo} = 10^{-1}$, the neutral stability curves obtained by setting $\sigma = 0$ support each other even though it is not assumed that $C_{BT1} = 0$ in the present QSSA. This means that C_{BT1} cannot grow as there is no convective term in equation (A.21). The theoretical critical time and corresponding

critical wavenumber can be determined by the minimum of such neutral stability curves and is discussed for the reactive cases in chapter 6.

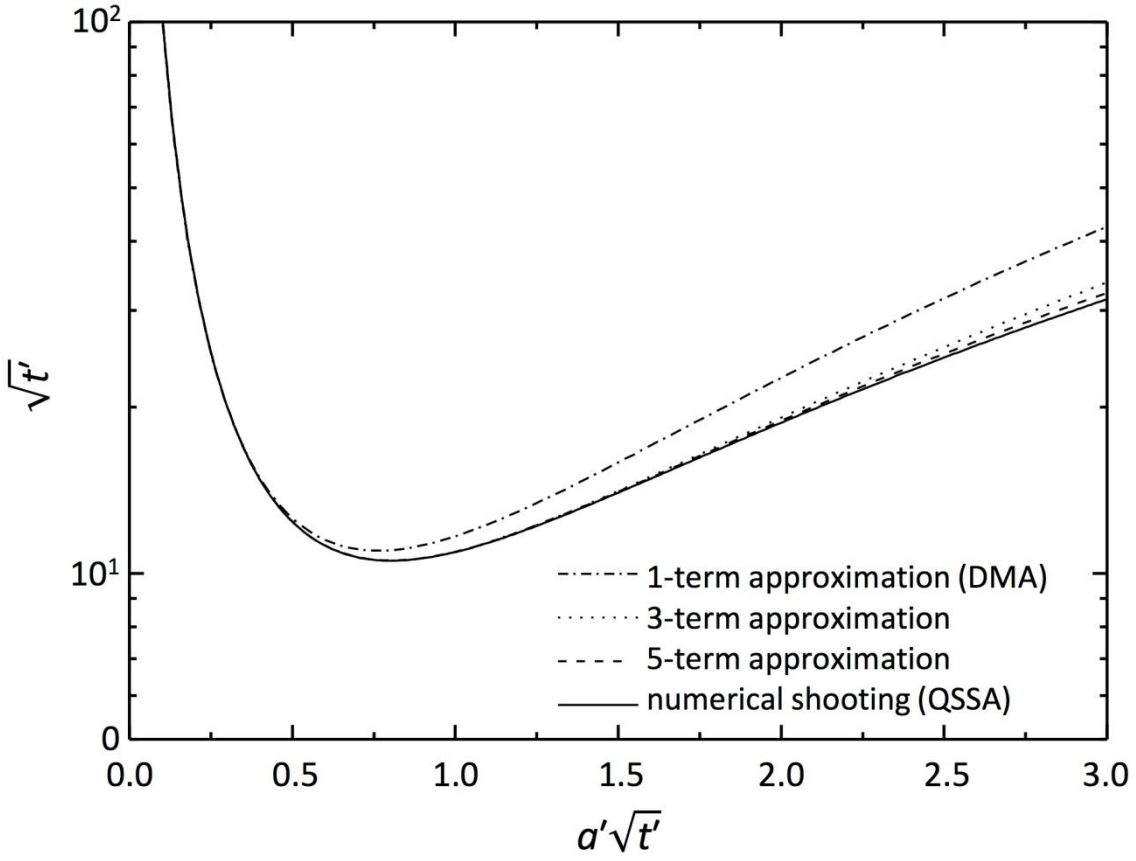

Figure A.1 Comparison of neutral stability curves obtained with and without the QSSA for the case where the MIBK – acetic acid – aqueous ammonia system where the initial dimensionless concentration of ammonia in the lower layer $C_{Bo} = 10^{-1}$.

A.4 NONLINEAR NUMERICAL SIMULATIONS

The linear stability analysis above is only applicable when the perturbations are small in amplitude. In order to compare theoretical predictions with corresponding experiments, a solution of the full nonlinear set of governing equations is required. By expressing the velocity and concentration fields as $\mathbf{v} = (-\frac{\partial \psi}{\partial z}, 0, \frac{\partial \psi}{\partial x},)$ and $C_{AT}(t, x, z) = C_{ATb}(t, x, z) + C_{AT1}(t, x, z)$, where ψ is a stream function, and $C_{ATb} = \text{erfc}(z/2\sqrt{t})$, the field equations for the concentration and the stream function reduce to

$$\nabla^2\psi = -\omega \tag{A.51}$$

$$\frac{\partial C_{AT1}}{\partial t} = \nabla^2 C_{AT1} - J_A \tag{A.52}$$

$$\frac{\partial C_{BT1}}{\partial t} = \nabla^2 C_{BT1} - J_B \tag{A.53}$$

$$\omega = \left\{\frac{\partial C_{AT1}}{\partial z} + (\beta_C - 1)\frac{\partial C_{BT1}}{\partial z}\right\} \text{ for } C_{AT1} - C_{BT1} \geq C_{Bo} - \text{erfc}\left(\frac{z}{2\sqrt{t}}\right) \tag{A.54}$$

$$\omega = \left\{(\beta_C - \beta_B)\frac{\partial C_{AT1}}{\partial z} + \beta_B \frac{\partial C_{BT1}}{\partial z}\right\} \text{ for } C_{AT1} - C_{BT1} \leq C_{Bo} - \text{erfc}\left(\frac{z}{2\sqrt{t}}\right) \tag{A.55}$$

$$J_A = \frac{\partial \psi}{\partial x}\frac{\partial C_{ATb}}{\partial z} + \left(\frac{\partial \psi}{\partial x}\frac{\partial C_{AT1}}{\partial z} - \frac{\partial \psi}{\partial z}\frac{\partial C_{AT1}}{\partial x}\right) \tag{A.56}$$

$$J_B = \left(\frac{\partial \psi}{\partial x}\frac{\partial C_{BT1}}{\partial z} - \frac{\partial \psi}{\partial z}\frac{\partial C_{BT1}}{\partial x}\right) \tag{A.57}$$

where $\omega = \partial u/\partial z - \partial w/\partial x$. The proper boundary conditions are

$$\psi = C_{AT1} = C_{BT1} = 0 \text{ at } z = 0 \text{ and } z \to \infty \tag{A.58}$$

Using the discrete Fourier transform (DFT), in the *x*- and *z*-directions, equations (A.51) – (A.53) are transformed into the following ordinary differential equations

$$(k_m^2 + k_n^2)\Psi_{mn} = \Omega_{mn} \tag{A.59}$$

$$\frac{\partial c_{ATmn}}{\partial t} = -(k_m^2 + k_n^2)c_{ATmn} - j_{Amn} \tag{A.60}$$

$$\frac{\partial c_{BTmn}}{\partial t} = -(k_m^2 + k_n^2)c_{BTmn} - j_{Bmn} \tag{A.61}$$

where Ψ_{mn} = F($\widehat{\psi}$), Ω_{mn} = F($\widehat{\omega}$), c_{ATmn} = F($\hat{C}_{AT1}$), c_{BTmn} = F($\hat{C}_{BT1}$), j_{Amn} = F ($\hat{J}_A$) and j_{Bmn} = F ($\hat{J}_B$). Here, F($\hat{f}$) is the DFT of $\hat{f}(t, x, z)$ and $\hat{f}(t, x, z)$ is the odd expansion of $f(t, x, z)$. The system of ordinary differential equations can be solved as

$$c_{ATmn}(t) = \exp\{(k_m^2 + k_n^2)t\}\left[\int_{t_e}^{t} \exp\{-(k_m^2 + k_n^2)\tau\} j_{Amn} d\tau\right] + c_{ATmn}(t_e) \tag{A.62}$$

$$c_{BTmn}(t) = \exp\{(k_m^2 + k_n^2)t\}\left[\int_{t_e}^{t} \exp\{-(k_m^2 + k_n^2)\tau\} j_{Bmn} d\tau\right] + c_{BTmn}(t_e) \tag{A.63}$$

The Adams-Bashforth predictor-corrector method is used to calculate the integral in equations (A.62) and (A.63). The equations above were solved to obtain the Fourier components Ψ_{mn}, c_{ATmn} and c_{BTmn}, after which the physical components $\psi(t, x, z)$, $C_{AT}(t, x, z)$ and $C_{BT}(t, x, z)$ were obtained by taking the inverse transform of the Fourier components.

In the present analysis, the calculation domain the numerical domain $[0, L_x] \times [0, L_z]$ is set to $[0, 2 \times 10^3] \times [-10^3, 10^3]$, and 2,048 × 2,048 collocation points are used. Unlike the linear theory, the initial magnitude of perturbations is important in the nonlinear analysis. As shown in equation (A.27), since the initial growth rate analysis cannot suggest a wavenumber, in the present simulation the following initial condition is employed

$$\hat{C}_{AT1} = \varepsilon \frac{1}{\sqrt{2\sqrt{\pi}}} \left(\frac{z}{\sqrt{t_i}}\right) \exp\left(-\frac{z^2}{4t_i}\right) \mathrm{rand}(x) \text{ at } t = t_i \tag{A.64}$$

$$\hat{C}_{BT1} = 0 \text{ at } t = t_i \tag{A.65}$$

where ε corresponds to the initial perturbation level and $\mathrm{rand}(x)$ is the pseudo-random number uniformly distributed between –1 and 1. This condition prevents unphysical conditions of $C_{AT} > 1$or $C_{AT} < 0$, if ε is small enough. In the present analysis, we set $\varepsilon = 10^{-2}$ and $t_i = 10^{-1}$. Due to the nature of the Fourier spectral method, the lateral periodic boundary condition is naturally imposed. However, unlike the linear analysis of the previous section, the wavenumber is not fixed.

The convective motion is characterised by the rate of mass transfer. The dimensionless total mass flux of solute at the interface $z = 0$, J_A, can be obtained as

$$J_A = \frac{1}{L_x} \int_0^{L_x} -\frac{\partial C_{ATb}}{\partial z}\bigg|_{z=0} dx + \frac{1}{L_x} \int_0^{L_x} -\frac{\partial C_{AT1}}{\partial z}\bigg|_{z=0} dx \tag{A.66}$$

The diffusional flux can be computed explicitly from the base concentration profile as

$$J_{Ab} = -\frac{\partial C_{ATb}}{\partial z}\bigg|_{z=0} = \frac{1}{\sqrt{\pi t}} \tag{A.67}$$

and the above convective flux can be expressed as

$$J_{A1} = \frac{1}{L_x} \int_0^{L_x} -\frac{\partial C_{AT1}}{\partial z}\bigg|_{z=0} dx = \frac{1}{L_x L_z} \int_0^{L_x} (C_{AT1} w) dz dx \tag{A.68}$$

REFERENCES

Almarcha, C., Trevelyan, P.M.J., Grosfils, P. and De Wit, A., 2013. Thermal effects on the diffusive layer convection instability of an exothermic acid-base reaction front. *Physical Review E - Statistical, Nonlinear, and Soft Matter Physics*, 88(3), pp.1–11.

Almarcha, C., Trevelyan, P.M.J., Riolfo, L. A., Zalts, A., El Hasi, C., D'Onofrio, A. and De Wit, A., 2010. Active Role of a Color Indicator in Buoyancy-Driven Instabilities of Chemical Fronts. *The Journal of Physical Chemistry Letters*, 1(4), pp.752–757.

Andres, J.T.H. and Cardoso, S.S.S., 2011. Onset of convection in a porous medium in the presence of chemical reaction. *Physical Review E*, 83(4), pp.6–11.

Andres, J.T.H. and Cardoso, S.S.S., 2012. Convection and reaction in a diffusive boundary layer in a porous medium: Nonlinear dynamics. *Chaos*, 22(3), p.037113.

Audigane, P., Gaus, I., Czernichowski-Lauriol, I., Pruess, K. and Xu, T., 2007. Two-dimensional reactive transport modeling of CO_2 injection in a saline aquifer at the Sleipner site, North Sea. *American Journal of Science*, 307(7), pp.974–1008.

Bachu, S., Gunter, W.D. and Perkins, E.H., 1994. Aquifer disposal of CO_2: Hydrodynamic and mineral trapping. *Energy Conversion and Management*, 35(4), pp.269–279.

Bachu, S., 2003. Screening and ranking of sedimentary basins for sequestration of CO_2 in geological media in response to climate change. *Environmental Geology*, 44(3), pp.277–289.

Bachu, S., 2008. CO_2 storage in geological media: Role, means, status and barriers to deployment. *Progress in Energy and Combustion Science*, 34(2), pp.254–273.

Bachu, S., 2015. Review of CO_2 storage efficiency in deep saline aquifers. *International Journal of Greenhouse Gas Control*, 40, pp.188–202.

Backhaus, S., Turitsyn, K. and Ecke, R.E., 2011. Convective Instability and Mass Transport of Diffusion Layers in a Hele-Shaw Geometry. *Physical Review Letters*, 106(10), p.104501.

Balashov, V.N., Guthrie, G.D., Hakala, J.A., Lopano, C.L., Rimstidt, J.D. and Brantley, S.L., 2013. Predictive modeling of CO_2 sequestration in deep saline sandstone reservoirs: Impacts of geochemical kinetics. *Applied Geochemistry*, 30, pp.41–56.

Bickle, M., Chadwick, A., Huppert, H.E., Hallworth, M. and Lyle, S., 2007. Modelling carbon dioxide accumulation at Sleipner: Implications for underground carbon storage. *Earth and Planetary Science Letters*, 255(1-2), pp.164–176.

BP, 2016. BP Statistical Review of World Energy 2016. London.

Bratsun, D.A. and De Wit, A., 2011. Buoyancy-driven pattern formation in reactive immiscible two-layer systems. *Chemical Engineering Science*, 66(22), pp.5723–5734.

Budroni, M.A., Riolfo, L.A., Lemaigre, L., Rossi, F., Rustici, M. and De Wit, A., 2014. Chemical Control of Hydrodynamic Instabilities in Partially Miscible Two-Layer Systems. *The Journal of Physical Chemistry Letters*, (5), pp.875–881.

Bulicka, J. and Prochazka, J., 1976, Diffusion Coefficients in Some Ternary Systems. *Journal of Chemical and Engineering Data*, (21), pp452-456.

Carballido-Landeira, J., Trevelyan, P.M.J., Almarcha, C. and De Wit, A., 2013. Mixed-mode instability of a miscible interface due to coupling between Rayleigh-Taylor and double-diffusive convective modes. *Physics of Fluids*, 25(2), p.024107.

Cardoso, S.S.S. and Andres, J.T.H., 2014. Geochemistry of silicate-rich rocks can curtail spreading of carbon dioxide in subsurface aquifers. *Nature Communications*, 5, p.5743.

Carslaw, H. S. and Jaeger, J. C., 1959, *Conduction of Heat in Solids*, Oxford University Press, Oxford.

Chadwick, A., Arts, R., Bernstone, C., May, F., Thibeau, S. and Zweigel, P., 2008. Best practice for the storage of CO_2 in saline aquifers - observations and guidelines from the SACS and CO2STORE projects. North Star, Nottingham: British Geological Survey.

Chadwick, R.A., Williams, G.A., Williams, J.D.O. and Noy, D.J., 2012. Measuring pressure performance of a large saline aquifer during industrial-scale CO_2 injection: The Utsira Sand, Norwegian North Sea. *International Journal of Greenhouse Gas Control*, 10, pp.374–388.

Cheng, P., Bestehorn, M. and Firoozabadi, A., 2012. Effect of permeability anisotropy on buoyancy-driven flow for CO_2 sequestration in saline aquifers. *Water Resources Research*, 48(9), pp.1–16.

Chevalier, S., Faisal, T.F., Bernabe, Y., Juanes, R. and Sassi, M., 2015. Numerical sensitivity analysis of density driven CO_2 convection with respect to different modeling and boundary conditions. *Heat and Mass Transfer*, 51(7), pp.941–952.

D'Hernoncourt, J., Zebib, A. and De Wit, A, 2007. On the classification of buoyancy-driven chemo-hydrodynamic instabilities of chemical fronts. *Chaos (Woodbury, N.Y.)*, 17(1), p.013109.

Duan, Z. and Sun, R., 2003. An improved model calculating CO_2 solubility in pure water and aqueous NaCl solutions from 273 to 533 K and from 0 to 2000 bar. *Chemical Geology*, 193(3-4), pp.257–271.

Eckert, K., Acker, M. and Shi, Y., 2004. Chemical pattern formation driven by a neutralization reaction. I. Mechanism and basic features. *Physics of Fluids*, 16(2), p.385.

Eckert, K. and Grahn, A., 1999. Plume and Finger Regimes Driven by an Exothermic Interfacial Reaction. *Physical Review Letters*, 82(22), pp.4436–4439.

Elenius, M.T. and Johannsen, K., 2012. On the time scales of nonlinear instability in miscible displacement porous media flow. *Computational Geosciences*, 16(4), pp.901–911.

Ennis-King, J. and Paterson, L., 2005. Role of Convective Mixing in the Long-Term Storage of Carbon Dioxide in Deep Saline Formations.pdf. *SPE Journal*, 10(3), pp.349–356.

Ennis-King, J. and Paterson, L., 2007. Coupling of geochemical reactions and convective mixing in the long-term geological storage of carbon dioxide. *International Journal of Greenhouse Gas Control*, 1(1), pp.86–93.

Ennis-King, J., Preston, I. and Paterson, L., 2005. Onset of convection in anisotropic porous media subject to a rapid change in boundary conditions. *Physics of Fluids*, 17(8), p.084107.

Etheridge, D.M., Steele, L.P., Langenfelds, R.L., Francey, R.J., Barnola, J.-M. and Morgan, V.I., 1996. Natural and anthropogenic changes in atmospheric CO_2 over the last 1000 years from air in Antarctic ice and firn. *Journal of Geophysical Research: Atmospheres*, 101(D2), pp.4115–4128.

Faisal, T.F., Chevalier, S., Bernabe, Y., Juanes, R. and Sassi, M., 2015. Quantitative and qualitative study of density driven CO_2 mass transfer in a vertical Hele-Shaw cell. *International Journal of Heat and Mass Transfer*, 81, pp.901–914.

Farajzadeh, R., Meulenbroek, B., Daniel, D., Riaz, A. and Bruining, J., 2013. An empirical theory for gravitationally unstable flow in porous media. *Computational Geosciences*, 17(3), pp.515–527.

Farajzadeh, R., Salimi, H., Zitha, P.L.J. and Bruining, H., 2007. Numerical simulation of density-driven natural convection in porous media with application for CO_2 injection projects. *International Journal of Heat and Mass Transfer*, 50(25-26), pp.5054–5064.

Florea, L., Fay, C., Lahiff, E., Phelan, T., O'Connor, N.E., Corcoran, B., Diamond, D. and Benito-Lopez, F., 2013. Dynamic pH mapping in microfluidic devices by

integrating adaptive coatings based on polyaniline with colorimetric imaging techniques. *Lab on a chip*, 13(6), pp.1079–85.

Garcia, J., 2001. Density of aqueous solutions of CO_2. *LBNL Report 49023*, Lawrence Berkeley National Laboratory, Berkeley, CA.

Ghesmat, K., Hassanzadeh, H. and Abedi, J., 2011. The effect of anisotropic dispersion on the convective mixing in long-term CO_2 storage in saline aquifers. *AIChE Journal*, 57(3), pp.561–570.

GISTEMP, 2016. *GISS Surface Temperature Analysis (GISTEMP)*. Goddard Institute for Space Studies. Available at: https://data.giss.nasa.gov/gistemp [Accessed 21 Jun. 2016].

Global CCS Institute, 2014. *The Global Status of CCS: 2014*., Melbourne, Australia

Gondal, S., Asif, N., Svendsen, H.F. and Knuutila, H., 2015. Kinetics of the absorption of carbon dioxide into aqueous hydroxides of lithium, sodium and potassium and blends of hydroxides and carbonates. *Chemical Engineering Science*, 123, pp.487–499.

Gunter, W.D., Wiwchar, B. and Perkins, E.H., 1997. Aquifer disposal of CO_2-rich Greenhouse Gases: Extension of the time scale of experiment for CO_2-sequestering reactions by geochemical modelling. *Mineralogy and Petrology*, 59(1), pp.121–140.

Hassanzadeh, H., Pooladi-Darvish, M. and Keith, D., 2007. Scaling behavior of convective mixing, with application to geological storage of CO_2. *AIChE journal*, 53(5), pp.1121–1131.

Hassanzadeh, H., Pooladi-Darvish, M. and Keith, D.W., 2005. Modelling of convective mixing in CO_2 storage. *Journal of Canadian Petroleum Technology*, 44(10), pp.43–50.

Hassanzadeh, H., Pooladi-Darvish, M. and Keith, D.W., 2006. Stability of a fluid in a horizontal saturated porous layer: effect of non-linear concentration profile, initial, and boundary conditions. *Transport in Porous Media*, 65(2), pp.193–211.

Herzog, H. and Golomb, D. a N., 2004. Carbon Capture and Storage from Fossil Fuel Use. *Encyclopedia of Energy*, 1, pp.1–11.

Hesse, M. a., Orr, F.M. and Tchelepi, H. a., 2009. Gravity currents with residual trapping. *Energy Procedia*, 1(1), pp.3275–3281.

Hidalgo, J.J. and Carrera, J., 2009. Effect of dispersion on the onset of convection during CO_2 sequestration. *Journal of Fluid Mechanics*, 640(2009), p.441.

Hikita, H., Asai, S. and Takatsuka, T., 1976. Absorption of carbon dioxide into aqueous sodium hydroxide and sodium carbonate-bicarbonate solutions. *The Chemical Engineering Journal*, 11(2), pp.131–141.

Huppert, H.E. and Neufeld, J.A., 2014. The Fluid Mechanics of Carbon Dioxide Sequestration. *Annual Review of Fluid Mechanics*, 46(1), pp.255–272.

IPCC, 2000. Special Report on Emissions Scenarios: A Special Report of Working Group III of the Intergovernmental Panel on Climate Change. Cambridge: Cambridge University Press, Cambridge, United Kingdom.

IPCC, 2007. Climate Change 2007: Synthesis Report. Contribution of Working Groups I, II and III to the Fourth Assessment Report of the Intergovernmental Panel on Climate Change. Geneva, Switzerland: IPCC.

IPCC, 2012. Special Report on Carbon Dioxide Capture and Storage. Cambridge University Press.

Javaheri, M., Abedi, J. and Hassanzadeh, H., 2009. Linear Stability Analysis of Double-Diffusive Convection in Porous Media, with Application to Geological Storage of CO_2. *Transport in Porous Media*, 84(2), pp.441–456.

Juanes, R., MacMinn, C.W. and Szulczewski, M.L., 2010. The footprint of the CO_2 plume during carbon dioxide storage in saline aquifers: Storage efficiency for capillary trapping at the basin scale. *Transport in Porous Media*, 82(1), pp.19–30.

Kim, M.C. and Choi, C.K., 2012. Linear stability analysis on the onset of buoyancy-driven convection in liquid-saturated porous medium. *Physics of Fluids*, 24(4), p.044102.

Kim, M.C. and Choi, C.K., 2014. Effect of first-order chemical reaction on gravitational instability in a porous medium. *Physical Review E - Statistical, Nonlinear, and Soft Matter Physics*, 90(5), p.53016.

Kim, M.C. and Choi, C.K., 2015. Some theoretical aspects on the onset of buoyancy-driven convection in a fluid-saturated porous medium heated impulsively from below. *Korean J. Chem. Eng.*, 32(12), pp.2400–2405.

Kim, S. and Santamarina, J.C., 2014. CO_2 geological storage: Hydro-chemo-mechanical analyses and implications. *Greenhouse Gases: Science and Technology*, 4(4), pp.528–543.

Kneafsey, T.J. and Pruess, K., 2010. Laboratory flow experiments for visualizing carbon dioxide-induced, density-driven brine convection. *Transport in Porous Media*, 82(1), pp.123–139.

Kneafsey, T.J. and Pruess, K., 2011. Laboratory experiments and numerical simulation studies of convectively enhanced carbon dioxide dissolution. *Energy Procedia*, 4, pp.5114–5121.

Kuster, S., Riolfo, L.A, Zalts, A., El Hasi, C., Almarcha, C., Trevelyan, P.M.J., De Wit, A. and D'Onofrio, A., 2011. Differential diffusion effects on buoyancy-driven instabilities of acid-base fronts: the case of a color indicator. *Physical Chemistry Chemical Physics : PCCP*, 13(38), pp.17295–303.

Lamb, H., 1932. *Hydrodynamics*. Cambridge: Cambridge University Press.

Lemaigre, L., Budroni, M. a., Riolfo, L. a., Grosfils, P. and De Wit, a., 2013. Asymmetric Rayleigh-Taylor and double-diffusive fingers in reactive systems. *Physics of Fluids*, 25(1), p.014103.

Lindeberg, E. and Wessel-Berg, D., 2011. Upscaling studies of diffusion induced convection in homogeneous and heterogeneous aquifers. *Energy Procedia*, pp.3927–3934.

Loodts, V., Rongy, L. and De Wit, A., 2015. Chemical control of dissolution-driven convection in partially miscible systems: theoretical classification. *Physical Chemistry Chemical Physics : PCCP*, 17(44), pp.29814–23.

Loodts, V., Thomas, C., Rongy, L. and De Wit, A., 2014. Control of convective dissolution by chemical reactions: General classification and application to CO_2 dissolution in reactive aqueous solutions. *Physical Review Letters*, 113(11), p.114501.

Lopez, O., Idowu, N., Mock, A., Rueslatten, H., Boassen, T., Leary, S. and Ringrose, P., 2011. Pore-scale modelling of CO_2-brine flow properties at In Salah, Algeria. *Energy Procedia*, pp.3762–3769.

Macminn, C.W., Szulczewski, M.L. and Juanes, R., 2010. CO_2 migration in saline aquifers. Part 1. Capillary trapping under slope and groundwater flow. *Journal of Fluid Mechanics*, 662, pp.329–351.

MacMinn, C.W., Szulczewski, M.L. and Juanes, R., 2011. CO_2 migration in saline aquifers: Regimes in migration with dissolution. *Energy Procedia*. pp.3904–3910.

Marini, L., 2007. Geological sequestration of carbon dioxide: thermodynamics, kinetics, and reaction path modeling. Amsterdam: Elsevier.

Martens, S., Liebscher, A., Möller, F., Henninges, J., Kempka, T., Lüth, S., Norden, B., Prevedel, B., Szizybalski, A., Zimmer, M., Kühn, M. and Group, K., 2013. CO_2 Storage at the Ketzin Pilot Site, Germany: Fourth Year of Injection, Monitoring, Modelling and Verification. *Energy Procedia*, 37(0), pp.6434–6443.

Mohammed, O.F., Pines, D., Pines, E. and Nibbering, E.T.J., 2007. Aqueous bimolecular proton transfer in acid-base neutralization. *Chemical Physics*, 341(1-3), pp.240–257.

Mojtaba, S., Behzad, R., Rasoul, N.M. and Mohammad, R., 2014. Experimental study of density-driven convection effects on CO_2 dissolution rate in formation water for geological storage. *Journal of Natural Gas Science and Engineering*, 21, pp.600–607.

Nagatsu, Y. and De Wit, A., 2011, Viscous fingering of a miscible reactive $A + B \rightarrow C$ interface for an infinitely fast reaction: Nonlinear simulations. *Physics of Fluids*, 23(4), p.043103.

Neufeld, J.A. and Huppert, H.E., 2009. Modelling carbon dioxide sequestration in layered strata. *Journal of Fluid Mechanics*, 625, pp.353–370.

Neufeld, J.A., Hesse, M.A., Riaz, A., Hallworth, M.A., Tchelepi, H.A. and Huppert, H.E., 2010. Convective dissolution of carbon dioxide in saline aquifers. *Geophysical Research Letters*, 37(22), pp.2–6.

Nijsing, R.A.T.O., Hendriksz, R.H. and Kramers, H., 1959. Absorption of CO_2 in jets and falling films of electrolyte solutions, with and without chemical reaction. *Chemical Engineering Science*, 10(1-2), pp.88–104.

Nomeli, M.A., Tilton, N. and Riaz, A., 2014. A new model for the density of saturated solutions of CO_2-H_2O-NaCl in saline aquifers. *International Journal of Greenhouse Gas Control*, 31, pp.192–204.

Nordbotten, J.M., Celia, M.A. and Bachu, S., 2005. Injection and storage of CO_2 in deep saline aquifers: Analytical solution for CO_2 plume evolution during injection. *Transport in Porous Media*, 58(3), pp.339–360.

Novotny, P. and Sohnel, O., 1988. Densities of binary aqueous solutions of 306 inorganic substances. *Journal of Chemical and Engineering Data*, pp.49–55.

Oltean, C., Golfier, F. and Buès, M.A., 2008. Experimental and numerical study of the validity of Hele-Shaw cell as analogue model for variable-density flow in homogeneous porous media. *Advances in Water Resources*, 31(1), pp.82–95.

Orr, F.M., 2009. Onshore Geologic Storage of CO_2. *Science*, 325(5948), pp.1656–1658.

Outeda, R., El Hasi, C., D'Onofrio, A. and Zalts, A., 2014. Experimental study of linear and nonlinear regimes of density-driven instabilities induced by CO_2 dissolution in water. *Chaos (Woodbury, N.Y.)*, 24(1), p.013135.

Parker, L., Yarwood, R. and Selker, J., 2006. Observations of gas flow in porous media using a light transmission technique. *Water Resources Research*, 42(5), pp.1–5.

Parry, M.L., Canziani, O.F., Palutikof, J.P., van der Linden, P.J. and Hanson, C.E., 2007. Climate Change 2007: Impacts, Adaptation and Vulnerability. Contribution of Working Group II to the Fourth Assessment Report of the Intergovernmental Panel on Climate Change.

Pau, G.S.H., Bell, J.B., Pruess, K., Almgren, A.S., Lijewski, M.J. and Zhang, K., 2010. High-resolution simulation and characterization of density-driven flow in CO_2 storage in saline aquifers. *Advances in Water Resources*, 33(4), pp.443–455.

Portier, S. and Rochelle, C., 2005. Modelling CO_2 solubility in pure water and NaCl-type waters from 0 to 300^{o}C and from 1 to 300 bar. Application to the Utsira Formation at Sleipner. *Chemical Geology*, 217, pp.187–199.

Pramanik, S. and Mishra, M., 2014. Comparison of Korteweg stresses effect on the fi ngering instability of higher or less viscous miscible slices : Linear stability analysis. *Chemical Engineering Science*, 110, pp.144–152.

Pritchard, D. and Richardson, C.N., 2007. The effect of temperature-dependent solubility on the onset of thermosolutal convection in a horizontal porous layer. Journal of Fluid Mechanics,

Pritchard, D., Woods, A.W. and Hogg, A.J., 2001. On the slow draining of a gravity current moving through a layered permeable medium. *J. Fluid Mech.*, 444, pp.23–47.

Pritchard, D., 2009. The linear stability of double-diffusive miscible rectilinear displacements in a Hele-Shaw cell. *European Journal of Mechanics B/Fluids*, 28(4), pp.564–577.

Pruess, K. and Nordbotten, J., 2011. Numerical Simulation Studies of the Long-term Evolution of a CO_2 Plume in a Saline Aquifer with a Sloping Caprock. *Transport in Porous Media*, 90(1), pp.135–151.

Rees, D.A.S., Selim, A. and Ennis-King, J.P., 2008. The Instability of Unsteady Boundary Layers in Porous Media. *Emerging Topics in Heat and Mass Transfer in Porous Media*, 22, pp.85-110.

Riaz, A. and Cinar, Y., 2014. Carbon dioxide sequestration in saline formations: Part I-Review of the modeling of solubility trapping. *Journal of Petroleum Science and Engineering*, 124, pp.367–380.

Riaz, A., Hesse, M., Tchelepi, H.A. and Orr, F.M., 2005. Onset of convection in a gravitationally unstable diffusive boundary layer in porous media. *Journal of Fluid Mechanics*, 548(1), pp.87–111.

Ritchie, L.T. and Pritchard, D., 2011. Natural convection and the evolution of a reactive porous medium. *J. Fluid Mech.*, 673, pp.286–317.

Rongy, L., Trevelyan, P. and De Wit, a., 2008. Dynamics of A+B→C Reaction Fronts in the Presence of Buoyancy-Driven Convection. *Physical Review Letters*, 101(8), p.084503.

Rongy, L., Trevelyan, P.M.J. and De Wit, A., 2010. Influence of buoyancy-driven convection on the dynamics of A+B→C reaction fronts in horizontal solution layers. *Chemical Engineering Science*, 65(7), pp.2382–2391.

Rosenbauer, R.J., Koksalan, T. and Palandri, J.L., 2005. Experimental investigation of CO_2-brine-rock interactions at elevated temperature and pressure: Implications for CO_2 sequestration in deep-saline aquifers. *Fuel Processing Technology*, 86(14-15), pp.1581–1597.

Selim, A. and Rees, D. A. S., 2007, The Stability of a Developing Thermal Front in a Porous Medium. II Nonlinear Evolution. *Journal of Porous Media*, 10 (1), pp. 1-16.

Sherwood, T.K. and Pigford, R. L., 1956, *Absorption and Extraction*, McGraw-Hill, New York, USA

Sherwood, T.K., Evans, J.E. and Longcor, J.V. A, 1939. Extraction in spray and packed columns. *Industrial and Engineering Chemistry*, 31(9), pp.1144–1150.

Shi, Y. and Eckert, K., 2006. Acceleration of reaction fronts by hydrodynamic instabilities in immiscible systems. *Chemical Engineering Science*, 61(17), pp.5523–5533.

Slim, A.C., Bandi, M.M., Miller, J.C. and Mahadevan, L., 2013. Dissolution-driven convection in a Hele–Shaw cell. *Physics of Fluids*, 25(2), p.024101.

Slim, A.C. and Ramakrishnan, T.S., 2010. Onset and cessation of time-dependent, dissolution-driven convection in porous media. *Physics of Fluids*, 22(12), p.124103.

Slim, A.C., 2014. Solutal-convection regimes in a two-dimensional porous medium. *Journal of Fluid Mechanics*, 741, pp.461–491.

Smith, A.R., 1978. Color gamut transform pairs. *ACM SIGGRAPH Computer Graphics*, 12(3), pp.12–19.

Sohnel, O., Novotny, P. and Solc, Z., 1984. Densities of aqueous solutions of 18 inorganic substances. *Journal of Chemical and Engineering Data*, 29(4), pp.379–382.

Someya, S., Yoshida, S., Tabata, T. and Okamoto, K., 2009. The effect of chemical reaction on the mixing flow between aqueous solutions of acetic acid and ammonia. *International Journal of Heat and Mass Transfer*, 52(19-20), pp.4236–4243.

Spycher, N., Pruess, K. and Ennis-King, J., 2003. CO_2-H_2O mixtures in the geological sequestration of CO_2. I. Assessment and calculation of mutual solubilities from 12 to 100°C and up to 600 bar. *Geochimica et Cosmochimica Acta*, 67(16), pp.3015–3031.

Straughan, B., 2004. *The Energy Method, Stability, and Nonlinear Convection*. 2nd ed. New York: Springer-Verlag New York.

Tans, P. and Keeling, R., 2016. *Trends in Atmospheric Carbon Dioxide*. NOAA/ESRL. Available at: www.esrl.noaa.gov/gmd/ccgg/trends [Accessed 21 Jun. 2016].

Teng, H., 1998. Solubility of Liquid CO_2 in Synthetic Sea Water at Temperatures from 278 K to 293 K and Pressures from 6 .44 MPa to 29 .49 MPa, and. *Journal of Chemical and Engineering Data*, 9568(97), pp.2–5.

Thomas, C., Lemaigre, L., Zalts,A., D'Onofrio, A. and De Wit, A., 2015. Experimental study of CO_2 convective dissolution: The effect of color indicators. *International Journal of Greenhouse Gas Control*, 42, pp.525–533.

Titus, J.G., Barth, M.C., Gibbs, M.J., Hoffman, J.S. and Kenney, M., 1985. Greenhouse Effect and Sea Level Rise: A Challenge For This Generation. *Quarterly Journal of the Royal Meteorological Society*, 111(470), p.1139.

Torp, T.A. and Gale, J., 2004. Demonstrating storage of CO_2 in geological reservoirs: The Sleipner and SACS projects. *Energy*, 29(9-10), pp.1361–1369.

Tritton, D.J., 1977, *Physical Fluid Dynamics*. Van Nostranf Reinhold, New York, USA.

Trevelyan, P., Strier, D. and De Wit, A., 2008. Analytical asymptotic solutions of nA+mB→C reaction-diffusion equations in two-layer systems: A general study. *Physical Review E*, 78(2), pp.1–13.

Trevelyan, P.M.J., Almarcha, C. and De Wit, A., 2011. Buoyancy-driven instabilities of miscible two-layer stratifications in porous media and Hele-Shaw cells. *Journal of Fluid Mechanics*, 670(2011), pp.38–65.

Trevelyan, P.M.J., Almarcha, C. and De Wit, A., 2015. Buoyancy-driven instabilities around miscible A+B→C reaction fronts: A general classification. *Physical Review E - Statistical, Nonlinear, and Soft Matter Physics*, 91(2), pp.1–8.

Tsai, P.A., Riesing, K. and Stone, H.A., 2013. Density-driven convection enhanced by an inclined boundary: Implications for geological CO_2 storage. *Physical Review E - Statistical, Nonlinear, and Soft Matter Physics*, 87(1), p.011003.

Verdon, J. and Woods, A.W., 2007. Gravity-driven reacting flows in a confined porous aquifer. *Journal of Fluid Mechanics*, 588(2007), pp.29–41.

Vosper, H., Kirk, K., Rochelle, C., Noy, D. and Chadwick, A., 2014. Does numerical modelling of the onset of dissolution-convection reliably reproduce this key stabilization process in CO2 Storage? *Energy Procedia*. Elsevier B.V., pp.5341–5348.

Ward, T.J., Cliffe, K.A., Jensen, O.E. and Power, H., 2014a. Dissolution-driven porous-medium convection in the presence of chemical reaction. *Journal of Fluid Mechanics*, 747, pp.316–349.

Ward, T.J., Jensen, O.E., Power, H. and Riley, D.S., 2014b. High-Rayleigh-number convection of a reactive solute in a porous medium. *Journal of Fluid Mechanics*, 760, pp.95–126.

Ward, T.J., Jensen, O.E., Power, H. and Riley, D.S., 2015. Substrate degradation in high-Rayleigh-number reactive convection. *Physics of Fluids*, 27(11), p.116601.

Weast, R.C., Astle, M.J. and Beyer, W.H., 1979. *CRC Handbook of Chemistry and Physics*. 59th ed. Boca Raton, FL.

White, C.M., Strazisar, B.R., Granite, E.J., Hoffman, J.S. and Pennline, H.W., 2003. Separation and Capture of CO_2 from Large Stationary Sources and Sequestration in Geological Formations. EM: Air and Waste Management Association's Magazine for Environmental Managers, 53, pp.29–34.

De Wit, A., 2001. Fingering of Chemical Fronts in Porous Media. *Physical Review Letters*, 87(5), pp.1–4.

De Wit, A., 2004. Miscible density fingering of chemical fronts in porous media: Nonlinear simulations. *Physics of Fluids*, 16(1), p.163.

Wolf, A. V., 1966. Aqueous Solutions of Body Fluids - Their Concentrative Properties and Conversion Tables. New York and London: Harper & Row Publishers.

Woods, A.W. and Farcas, A., 2009. Capillary entry pressure and the leakage of gravity currents through a sloping layered permeable rock. *Journal of Fluid Mechanics*, 618(2009), p.361.

Wylock, C., Rednikov, A., Haut, B. and Colinet, P., 2014. Nonmonotonic rayleigh-taylor instabilities driven by gas-liquid CO_2 chemisorption. *Journal of Physical Chemistry B*, 118(38), pp.11323–11329.

Xu, T., Apps, J.A. and Pruess, K., 2004. Numerical simulation of CO_2 disposal by mineral trapping in deep aquifers. *Applied Geochemistry*, 19(6), pp.917–936.

Xu, X., Chen, S. and Zhang, D., 2006. Convective stability analysis of the long-term storage of carbon dioxide in deep saline aquifers. *Advances in Water Resources*, 29(3), pp.397–407.

Yang, C. and Gu, Y., 2006. Accelerated mass transfer of CO_2 in reservoir brine due to density-driven natural convection at high pressures and elevated temperatures. *Industrial and Engineering Chemistry Research*. pp.2430–2436.

Yasunishi, a and Yoshida, F., 1979. Solubility of carbon dioxide in aqueous electrolyte solutions. *Journal of Chemical and Engineering*, 24(7), pp.13–16.

Zalts, A., El Hasi, C., Rubio, D., Ureña, A. and D'Onofrio, A., 2008. Pattern formation driven by an acid-base neutralization reaction in aqueous media in a gravitational field. *Physical Review E*, 77(1), p.015304.

Zimmerman, W.B. and Homsy, G.M., 1991. Nonlinear viscous fingering in miscible displacement with anisotropic dispersion. *Physics of Fluids A: Fluid Dynamics*, 3(8), p.1859.